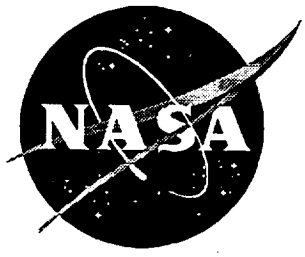

NASA Contractor Report 4686

Failure Models for Textile Composites

Brian Cox
Rockwell International Science Center • Thousand Oaks, California

National Aeronautics and Space Administration
Langley Research Center • Hampton, Virginia 23681-0001

Prepared for Langley Research Center
under Contract NAS1-19243

August 1995

Printed copies available from the following:

NASA Center for AeroSpace Information
800 Elkridge Landing Road
Linthicum Heights, MD 21090-2934
(301) 621-0390

National Technical Information Service (NTIS)
5285 Port Royal Road
Springfield, VA 22161-2171
(703) 487-4650

Table of Contents

List of Figures

List of Tables

Personnel

Brian Cox (program manager)

Mahyar Dadkhah

Fred Morris

Acknowledgments

The authors are indebted to Mr. Jonathan Flintoff for assistance with experiments; and to Messrs. Junde Xu and Mike McGlockton (UC Santa Barbara) for developing a generic solver for the Binary Model.

Inspiration was drawn throughout this research from the activities of the textiles working group in the Advanced Composites Technology Program at NASA Langley. The authors are especially pleased to recognize the guiding influence of Drs. C.E. Harris and C.C. Poe in that program.

Summary

The goals of this research program were to

(i) determine how microstructural factors, especially the architecture of reinforcing fibers, control stiffness, strength, strain to failure, work of fracture, notch sensitivity, and fatigue life in 3D woven composites;

(ii) identify mechanisms of failure;

(iii) model composite stiffness;

(iv) model strength; and

(v) model fatigue life.

A total of eleven different angle and orthogonal interlock woven composites were examined. These 3D woven composites possess an extraordinary combination of strength, damage tolerance, and notch insensitivity. In many important regards, they far outstrip conventional 2D laminates or stitched laminates.

We have determined the essential mechanisms of failure in monotonic and fatigue loading and how they are related to the reinforcement geometry. Composite properties depend on the weave architecture, the tow size, and the distributions in space and strength of geometrical flaws. Important concepts follow for reliability, design, and manufacture.

We have developed the simplest possible models for predicting elastic properties, strength, and fatigue life. These models can be implemented with minimal numerical computation. Other properties, especially relating to damage tolerance, ultimate failure, and the detailed effects of weave architecture, require computationally intensive stochastic modeling. We have developed a new model, the "Binary Model," to carry out such tasks in the most efficient manner.

This is the final report for task 9 in Space Systems Division contract NAS1-19243. It covers all work from January, 1993 up to the conclusion of the program in November, 1994.

1. Introduction

Textile composites with three-dimensional (3D) reinforcement possess some remarkable mechanical properties. In skin applications, 3D woven or braided composites and stitched laminates are invulnerable to failure by delamination and buckling, provided the through-thickness reinforcement is not distorted during fabrication [1–13]. The through-thickness reinforcement limits delamination and damage extension after impact, allowing compressive strength often to remain comparable to that of pristine material. Like 3D carbon-carbon composites of earlier years [3], 3D woven polymer composites possess exceptionally high strain to failure in either compression or tension [12,13]. In work of fracture and notch insensitivity in tension, they far surpass metal alloys and conventional polymer laminates [13].

Detailed experimental observations on 3D woven composites have revealed that the reinforcement geometry has a dominant role in determining mechanisms of failure [12–14]. Both the ideal composite geometry, in which in-plane tows are straight, and deviations from the ideal are important. In fact, high stress to failure, notch insensitivity, and damage tolerance can all be attributed to the presence of geometrical flaws in the reinforcement [12–13]. Some geometrical flaws consist of certain local configurations of tows, such as sites where through-thickness yarns wrap around nominally straight in-plane yarns. Other geometrical flaws are segments of in-plane tows that are misaligned to an unusually high degree.

This report deals with predicting the properties of 3D woven composites, emphasizing the roles of geometrical flaws and the weave architecture. For predicting composite elastic constants and tensile strength, geometrical flaws have a relatively minor role. For predicting compressive strength, fatigue life, damage tolerance, and work of fracture, geometrical flaws are all important. The reasons for this will be elucidated.

Many of the theoretical models described in the report have been encoded in computer programs. These are detailed in Appendices. Source codes are available in electronic form.

2. Materials

Analyses will be presented for the eleven woven interlock composites listed in Table 1. Figure 1 shows the three types of weave in this group: layer-to-layer and through-the-thickness angle interlock; and orthogonal interlock weaves. "Stuffer" and "filler" tows form an orthogonal array suggestive of a course 0°/90° laminate, while "warp weaver" tows provide through-thickness reinforcement. Complete specifications of weave patterns are given in Appendix A. In the jargon of crystallographers, all the weaves are orthorhombic in the absence of any tow distortions. The orthogonal interlock weaves are also invariant under certain inversions; but not the angle interlock weaves, as contemplation of the detailed drawings in Appendix A will reveal.

The subject composites can also be classified by the total fiber volume fraction, V, achieved in processing: "lightly compacted" composites, with relatively low V, and "heavily compacted" composites, with relatively high V. Table 1 reintroduces labels from [12] for the 11 composites studied, with the italic letter designating the degree of compaction (*"l"* for light and *"h"* for heavy).

The layers in Fig. 1 are much thicker than plies in a conventional 2D laminate, because the individual tows are ~ 1 mm^2 in cross section. Such coarseness lowers manufacturing cost, which rises with the number of yarns to be set up on the loom. Fortunately, it also favors damage tolerance and notch insensitivity [12].

Nearly all the composites of Table 1 consist of AS4 carbon fibers† in epoxy resin. The exceptions are composites *l*-L-2 and *l*-T-2, in which the warp weavers were S-glass fibers. All lightly consolidated composites were made with Tactix 138 resin cured with H41 hardener*; all heavily compacted composites were made with Shell RSL-1895 resin with EPON CURING AGENT® W.** Further processing details appear in [12-14].

Table 1 also lists for each composite the weaver's specifications of the linear density of yarns in the loom (ends per unit length, e, and picks per unit length, p) and the yields (length per unit mass) y_α, α = s, f, or w for stuffers, fillers, or warp weavers. (The symbol α will be used throughout this report to identify tow type in the weave.)

† Hercules Inc., Salt Lake City, Utah.
* Dow Chemical Co., Freeport, Texas.
** Shell Oil Co., Anaheim, California.

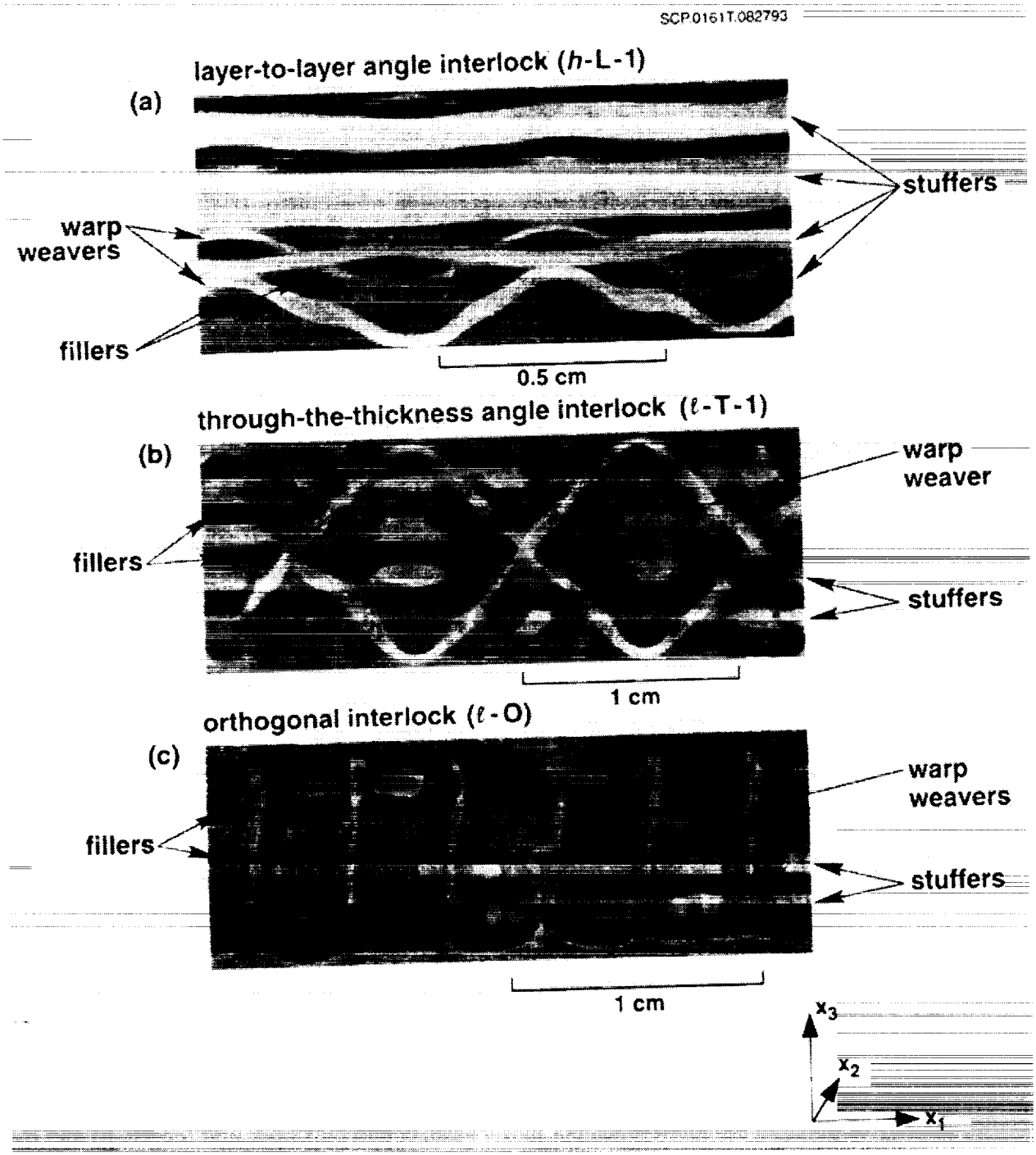

Figure 1. Sections normal to the filler direction of specimens with three different weave types. Stuffers and warp weavers appear as light ribbons. Sections of fillers appear as dark patches.

2.1 Fiber Distributions

Reliable predictions of engineering properties require accurate knowledge of the volume fractions of stuffer, filler, and warp weaver fibers. In principle, these volume fractions could be deduced from the weaver's specifications just listed, together with the measured thickness of the composite. However, this would assume that the mean separation of yarns did not change during manufacture of the composite, which may be optimistic.† In this work, the weaver's specifications were used only to deduce the fractions by volume f_α (α = s, f, or w) of all fibers that lie in stuffers, fillers, and warp weavers.*** All macroscopic elastic properties will be deduced from these fractions, the measured total fiber volume fraction, V, and the measured composite thickness, t.

In a composite with n_s layers of stuffers alternating with n_s+1 layers of fillers through the thickness, n_w warp weavers between successive columns of stuffers (see Appendix A), and in which all yarns are made of the same fibers

$$f_s = \frac{n_s e c_s}{L y_s} \; ; \; f_f = \frac{(n_s + 1) p c_f}{L y_f} \; ; \; f_w = \frac{n_w e c_w}{L y_w} \tag{1}$$

where c_s, c_f, and c_w are crimp factors; L is chosen to satisfy $f_s + f_f + f_w = 1$; and y_w is an appropriately weighted average for composites with warp weavers and surface warp weavers of unequal yields (composites *h*-L-1 and *h*-L-2). The crimp factors are customarily determined by measuring the lengths of yarns extracted from a representative length of woven preform. Both c_s and c_f are very close to unity. Values of c_w supplied by the weaver are given in Table 1. (For the lightly compacted composites, which were the first manufactured [13], crimp factors could not be found in old records. Estimates have been substituted. Since the warp weavers constitute a relatively small fraction of all reinforcement, the effect on f_s and f_f and therefore on almost all predicted properties of any error in c_w is negligible compared to other factors, especially softening due to waviness. The single exception is the through-thickness modulus - see Section 3.) The only additional measurement required to fix the density of reinforcement in a composite containing a single type of fiber is the total fiber volume fraction, V.

† Total fiber volume fractions estimated for the heavily compacted composites from the weaver's specifications and the measured composite thickness were found to be consistently higher than measured values by up to 5%.

*** It will be assumed here that stuffers and fillers spread equally during consolidation. This assumption is reasonable in manufacturing flat panels. When preforms are deformed to make curved parts, especially those involving nondevelopable transformations, tows are likely to thin or consolidate anisotropically. The analysis of such cases would be a useful research topic.

Table 1. Composite and Fiber Data

Composite Label	Architecture	Tow Yield			Linear Tow Density		Crimp Factor (Warp Weavers)
		Stuffers y_s (mm/g)	Fillers y_f (mm/g)	Weavers y_w (mm/g)	Stuffers e (mm^{-1})[a]	Fillers p (mm^{-1})[b]	c_w
(a) Lightly Compacted							
l-L-1	Layer-to-Layer	652	652	1525	0.51	0.44	1.2[c]
l-L-2	Angle Interlock	652	652	1510	0.51	0.59	1.2[c]
l-T-1	Through-the-Thickness	652	652	1525	0.47	0.50	1.4[c]
l-T-2	Angle Interlock	652	652	1510	0.51	0.50	1.4[c]
l-O	Orthogonal Interlock	652	652	1525	0.47	0.51	3.25[c]
(b) Heavily Compacted							
h-L-1	Layer-to-Layer	570	1140	(2280, 13600)[d]	0.55	0.51	1.2
h-L-2	Angle Interlock	1140	2280	(4570, 13600)[d]	0.71	0.79	1.03
h-T-1	Through-the-Thickness	570	1140	2280	0.55	0.51	1.375
h-T-2	Angle Interlock	1140	2280	4570	0.71	0.79	1.25
h-O-1	Orthogonal Interlock	570	1140	2280	0.55	0.51	4
h-O-2	Orthogonal Interlock	1140	2280	4570	0.71	0.79	4.5

[a] "ends per cm" ≡ number of columns of stuffers per cm in the weft direction
[b] "picks per cm" ≡ number of columns of fillers per cm in the warp direction
[c] Estimated, not measured
[d] The first figure refers to warp weavers, the second to surface warp weavers (see Appendix A)

In a composite in which the warp weavers contain different fibers from those in the stuffers and fillers (composites *l*-L-2 and *l*-T-2), f_w is determined by a separate experimental measurement of the volume fraction, V', of weaver fibers (S2 glass here): $f_w = V'/(V + V')$. In this case only f_s and f_f are defined by Eq. (1), with L chosen to satisfy $f_s + f_f = V/(V + V')$.

Table 2 shows values of f_s, f_f, and f_w computed by these rules, along with measured values of V and, where appropriate, V'.

In estimating flexural rigidity, information is also required of the distribution of stuffers and fillers through the thickness of the composites. Let t_f and t_s denote the thicknesses of filler and stuffer layers, with all filler layers assumed equal and all stuffer layers assumed equal (Fig. 2). (Generalization to unequal layers of stuffers or fillers,

which might be preferred to maximize flexural rigidity in one direction, follows obviously.) Assuming equal degrees of compaction of stuffers and fillers,

$$\frac{t_s}{t_f} = \frac{y_f e}{y_s p} \tag{2a}$$

while

$$(n_S + 1)\, t_f + n_S t_S = t\,, \tag{2b}$$

where t denotes the measured composite thickness (Table 2). Hence

$$t_f = \frac{y_s p t}{(n_s+1) y_s p + n_s y_f e} \tag{3a}$$

$$t_s = \frac{y_f e t}{(n_s+1) y_s p + n_s y_f e}\,. \tag{3b}$$

In the coordinate system of Fig. 2, the layers of the upper half of the stack have the boundaries $u_o = 0$ and

$$u_i = \begin{cases} \frac{i}{2} t_f + \frac{i-1}{2} t_s & (n_s i \text{ odd}) \\ \frac{i-1}{2} t_f + \frac{i}{2} t_s & (n_s i \text{ even}) \end{cases} \qquad (i=1,\ldots,n_s+1). \tag{4}$$

2.2 Tow Waviness

In contradiction of the ideal geometry prescribed by the weaver and widely assumed in prior modeling of textile composites, stuffers and fillers are in reality not straight. Indication of this for stuffers is visible in Fig. 1: the stuffers exhibit appreciable deflections in the out-of-plane or through-thickness direction (i.e., in x_1-x_3 planes in Fig. 1). Figure 3 shows that such irregularity or waviness can be quite dramatic for fillers. It is generally larger for fillers than stuffers because the stuffers, being warp yarns, are held in tension during weaving, whereas the fillers are non-tensioned weft. In the heavily compacted composites, filler distortion is probably further exacerbated by the fact that fillers are only half as thick as stuffers. Waviness in stuffers and fillers tends to be greater in the lightly compacted composites than in the heavily compacted composites; and greater for angle interlock than for orthogonal interlock weaves.

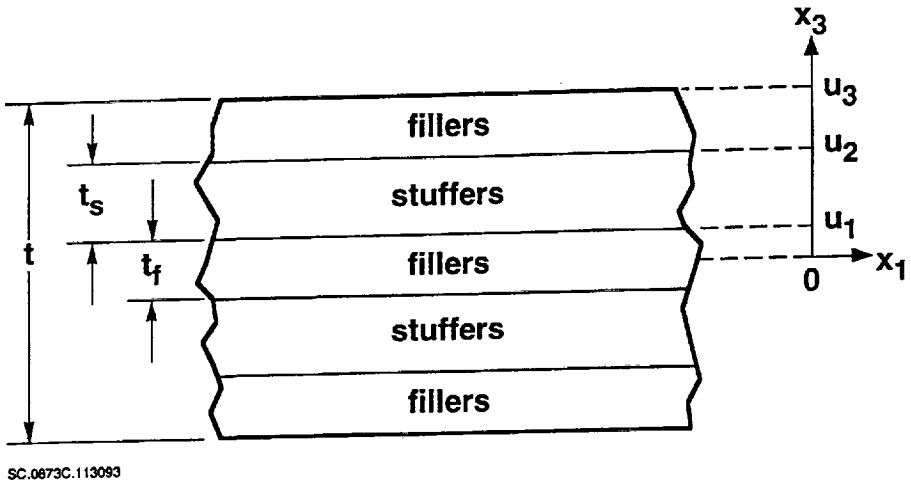

Figure 2. Representative layer sequence of fillers and stuffers through the thickness, with the layer thicknesses t_f and t_s defined. For the case shown, n_s=2.

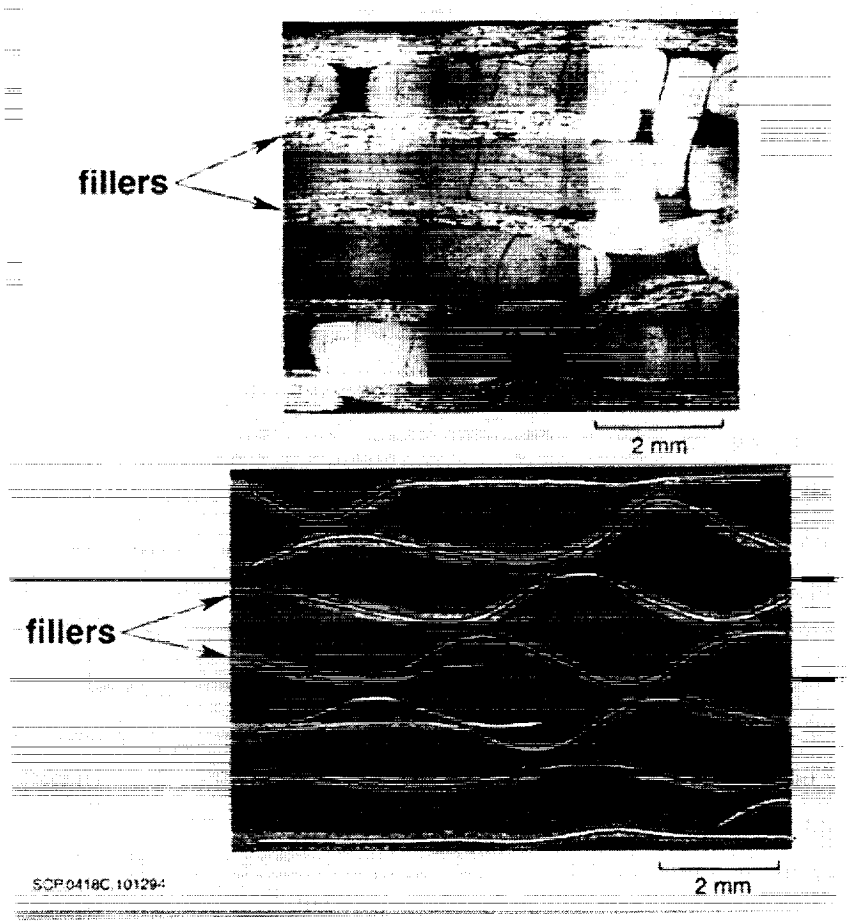

Figure 3. Sections of two specimens normal to the stuffer direction showing typical irregularity or waviness of fillers (above: *h*-L-1; below: *h*-L-2).

Table 2. Composite Volume Fractions and Dimensions

Composite Label	Fraction by Volume of All Fibers that Lie in: Stuffers f_s	Fillers f_f	Weavers f_w	Measured Fiber Volume Fraction[a] V (V')	Composite Thickness t (mm)
(a) Lightly Compacted					
l-L-1	0.385	0.418	0.197	0.35±0.03	12.6
l-L-2	0.347	0.502	0.151	0.370±0.005[b] (0.066±0.004[c])	12.4
l-T-1	0.381	0.504	0.115	0.466±0.003	10.2
l-T-2	0.406	0.497	0.097	0.408±0.020[b] (0.044±0.004[c])	9.7
l-O	0.387	0.524	0.090	0.483±0.010	8.8
(b) Heavily Compacted					
h-L-1	0.587	0.340	0.073	0.620±0.008	5.61
h-L-2	0.580	0.375	0.045	0.557±0.015	6.25
h-T-1	0.571	0.331	0.098	0.613±0.003	5.73
h-T-2	0.571	0.369	0.059	0.592±0.014	5.77
h-O-1	0.586	0.340	0.073	0.619±0.008	5.79
h-O-2	0.545	0.353	0.102	0.593±0.014	5.87

[a] measured by acid digestion following ASTM Standard D3171
[b] graphite fibers
[c] glass fibers

Warp weavers also exhibit waviness; in some cases, they are the most severely distorted of all the tows. Warp weaver irregularity is generally more pronounced in angle interlock than in orthogonal interlock composites. It is also closely correlated with the reduction in thickness of the woven preform during consolidation of the composite [12], as should be expected. Some examples of warp weaver crimp appear in Fig. 4. See also Fig. 4 of [12].

There is also some in-plane misalignment of stuffers and fillers, i.e., in the x_1–x_2 plane. However, these fluctuations are considerably smaller than out-of-plane misalignments and are neglected in all the following analyses.

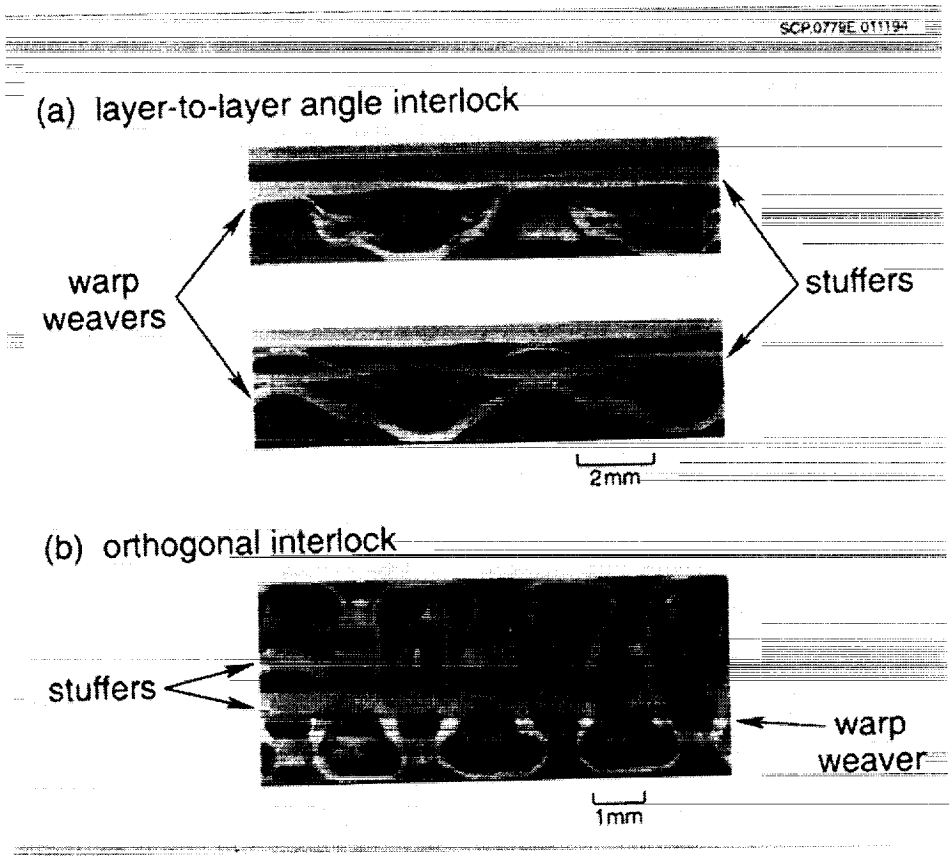

Figure 4. Sections normal to the filler direction showing warp weaver crimp in two heavily compacted composites.

Out-of-Plane Waviness of Stuffers and Fillers

Out-of-plane waviness was quantified by statistical analysis of digitized images of cross sections.† Digital image analysis was used to reduce images of stuffers and fillers such as those in Figs. 1 and 3 to one dimensional curves or "tow loci" representative of their centers. Typical tow loci are shown superimposed on the fillers of Fig. 3. The analysis of elastic properties requires data on the distribution of out-of-plane misalignment angles along the entire length of tows. The analysis of strength and fatigue life requires distributions of extreme values.

Considerable effort was expended in finding the best method of generating and smoothing tow loci. Details of the procedure finally selected are as follows. Cross sectional images were first digitized on 256 × 256 arrays. The size of the area on the specimen represented by a single pixel depended on the image magnification. A gray

† Similar analysis of waviness in triaxial braids can be found in [15] and [16].

level threshold was then used to delineate individual tows. The representation of each tow identified in this manner was then skeletonized by alternately eliminating pixels from the upper and lower boundaries. The coordinates of the centers of mass of the surviving pixels in the skeletons were stored for subsequent analysis as the raw tow loci data. Subjectivity entered in the procedure to this point only in a small amount of touching up to aid in contrast thresholding and the elimination of some spurious features associated with fragments of tows caught on the specimen section.

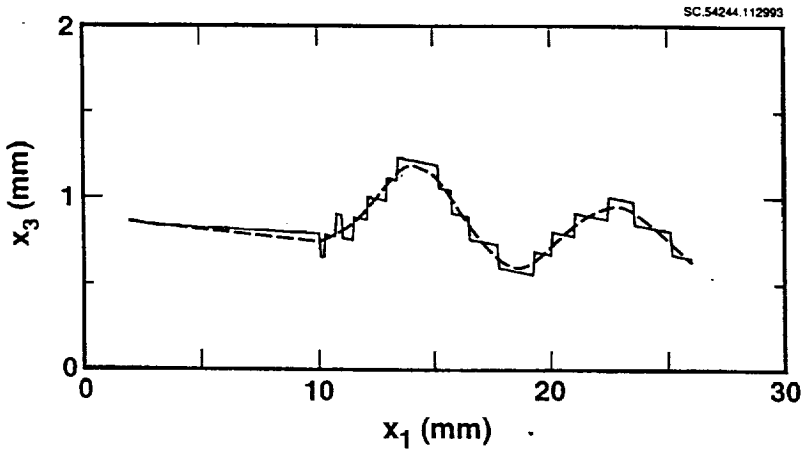

Figure 5. Steps on a digitized tow locus reflecting the size of pixels in the digitized image (solid curve); and a smoothing spline function (dashed curve).

The first step in deducing misalignment data from the raw tow loci data was to eliminate noise arising from the digital image processing. The noise consisted of steps corresponding to the pixel size (Fig. 5). In such stepped data, the most accurately known values are the midpoints of the vertical segments. Smoothing was therefore effected by fitting cubic splines to the set of all step midpoints on each locus. The fitting routine used* finds splines of minimum curvature such that the root mean square difference between the fitted splines and the data points does not exceed some specified amount δ. Forcing the splines to pass exactly through the data ($\delta = 0$) results in large oscillations or ringing as the splines accommodate noise. Specifying a very large value of δ results in lost information, with the fitted spline tending to a straight line. The optimal choice of δ should correspond to the expected error in each datum. The error should be a small fraction of the step height, but is difficult to specify a priori. Therefore, the optimal value of δ was determined by comparing fitted splines with the original micrographs by eye. Acceptable fits were found when $\delta = 0.02 \pm 0.01$ mm, or about one fifth of the step height

* IMSL (International Mathematical Software Library) routine ICSCSU.

(Figs. 3 and 5). The fitted curves were considerably superior to smoothed curves obtained by filtering Fourier transforms.

To check the adequacy of the pixel density, some cross sections were analyzed again starting with images of higher magnification. The step size was accordingly smaller. With δ again set to one fifth the average step size, smoothed curves close to those obtained from the lower magnification images were generated.

At least five sections were analyzed for each material. A cumulative probability distribution (cpd) was then formed for the out-of-plane misalignment angle, ξ, of small, equal intervals on all smoothed tow loci. Typical cpds are shown in Fig. 6. Although there are no obvious physical grounds to expect it, experience shows that each such cpd can be fitted quite well by a symmetric normal distribution

$$F_\xi(\xi) = \int_{-\infty}^{\xi} f_\xi(\xi')\, d\xi', \tag{5a}$$

with the density function $f_\xi(\xi)$ given by

$$f_\xi(\xi) = \frac{1}{\sigma_\xi \sqrt{2\pi}} e^{-\xi^2/2\sigma_\xi^2}. \tag{5b}$$

Typical fitted functions $F_\xi(\xi)$ are also shown in Fig. 6. The width, σ_ξ, of the distributions determines the degree of softening of Young's modulus in the tow direction due to out-of-plane tow waviness (see below). Values of σ_ξ determined by maximum likelihood estimators are listed in Table 3.

The influence of uncertainty in the smoothing parameter δ was assessed by reevaluating σ_ξ using the lowest and highest credible values assigned to δ. The resulting uncertainty in σ_ξ is also indicated in Table 3. For stuffers, it is typically ~ 30%; for fillers, ~ 10%. Higher (lower) values of δ lead to narrower (broader) distributions of ξ. However, as long as δ is varied consistently for all cases, the net effect is broadening or narrowing of all distributions by the same factor. The *relative* uncertainty in σ_ξ for different composites may therefore be much less than the uncertainty shown in Table 3. From statistical arguments, it should fall as the square root of the number of data points sampled (e.g. [17]). When the data available for the stuffers in each composite were analyzed in two halves, the two values of σ_ξ obtained differed typically by 10%. This is a better estimate of the *relative* uncertainty in out-of-plane misalignment angles for stuffers.

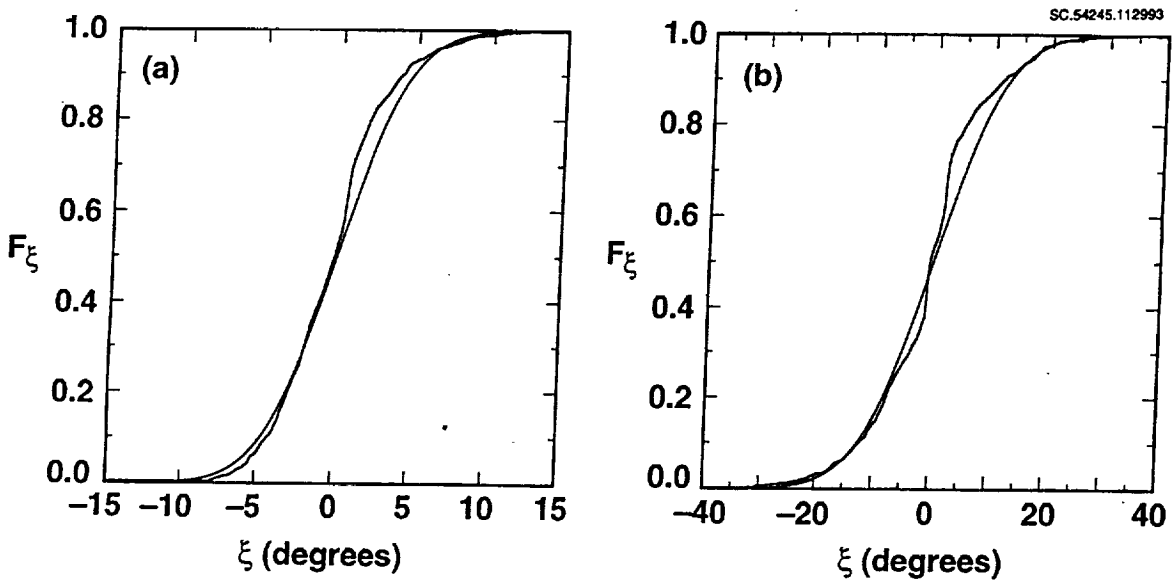

Figure 6. Distributions of the out-of-plane misalignment angle ξ for (a) stuffers in the composite *l*-T-2 and (b) fillers in the composite *l*-L-2. The irregular curves are the data; the overlaid smooth curves show symmetric normal distributions fitted by maximum likelihood estimators.

Crimp of Warp Weavers

The distortion of warp weavers is much more difficult to quantify. Warp weavers follow complicated paths and are often much more severely crimped than stuffers or fillers (e.g. Fig. 4). Warp weavers, being of lighter denier, also exhibit greater departures proportional to their widths from the planes in which they nominally lie. Therefore specimen sections rarely display cleanly defined outlines of warp weavers. Warp weavers fade in and out of exposed sections and have often been fragmented by the cutting action.

It was not possible to obtain realistic statistics for warp weaver misalignment angles; however these might be defined. Instead, a qualitative assessment of the degree of crimp was made by inspecting images of cross sections such as Fig. 4. The degree of crimp is manifestly correlated with the extent to which the dry fiber preform was squashed in consolidating the composite (Table 3): compare the heavily compacted composite of Fig. 4a with the lightly compacted composite of Fig. 1b.

Table 3. Tow Waviness Parameters

Composite Label	σ_ξ (degrees) Stuffers	σ_ξ (degrees) Fillers	Stiffness Knockdown Factor $\eta(\alpha)$ Stuffers	Stiffness Knockdown Factor $\eta(\alpha)$ Fillers	Degree of Warp Weaver Crimp	Composite Thickness/ Preform Thickness
l-L-1	_[a]	_[a]	-	-	severe	_[b]
l-L-2	4.0±1.0	9.9±0.8	0.82±0.07	0.45±0.04	severe	-
l-T-1	3.4±0.8	6.0±0.6	0.86±0.06	0.66±0.04	intermediate	-
l-T-2	3.7±0.7	6.4±0.8	0.84±0.05	0.64±0.05	intermediate	-
l-O	3.4±0.8	1.2±1.0	0.86±0.06	0.98±0.05	severe	-
h-L-1	1.7±0.5	4.8±0.7	0.97±0.02	0.69±0.06	severe	0.79
h-L-2	2.0±0.6	14.8±0.8	0.95±0.02	0.32±0.02	severe	0.75
h-T-1	1.3±0.5	2.9±0.7	0.98±0.02	0.91±0.04	intermediate	0.83
h-T-2	1.7±0.3	4.2±1.0	0.97±0.02	0.83±0.06	slight	0.93
h-O-1	0.3±0.1	3.4±0.7	0.99±0.01	0.89±0.05	intermediate	0.87
h-O-2	1.2±0.6	1.8±1.0	0.98±0.02	0.97±0.06	slight	0.91

[a] This preform was so inhomogeneously distorted that meaningful measurements of F_ξ could not be made.

[b] Not known for lightly compacted composites.

Out-of-Plane Misalignment Extrema

Out-of-plane misalignment extrema were defined as the angles of maximum magnitude between successive zeros of ξ. Successive zeros of ξ tend to be separated by a length commensurate with the tow spacing - misalignment is a product of the reinforcement architecture. The misalignment extrema are identified with the tow segment misalignment angle ζ.

Figure 7 shows cumulative probability distributions (cpd's) F_ζ of ζ. The cpd's fall clearly into two groups, corresponding to the lightly and heavily compacted composites. The lightly compacted composites are the most severely misaligned, a result mainly of inferior control of tow regularity during the weaving process.

The statistics of misalignment extrema are essential in estimating strength and fatigue life (Section 5).

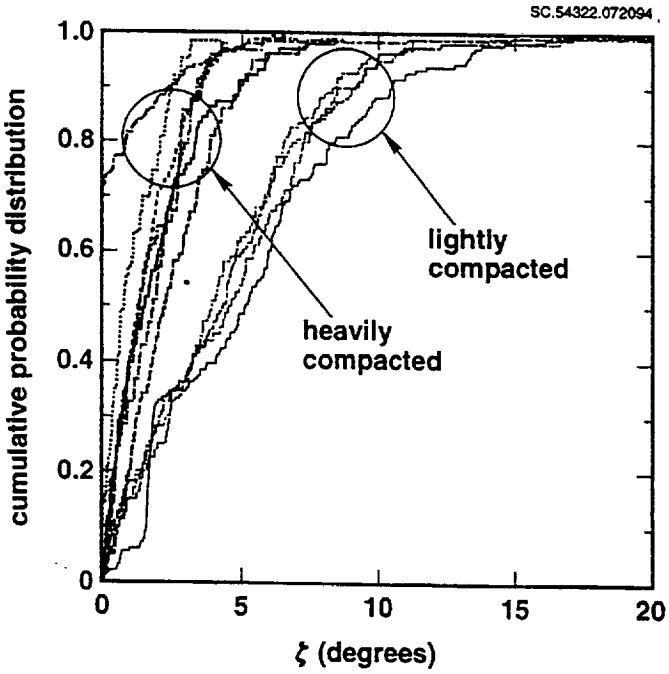

Figure 7. Cumulative probability distributions for measured misalignment extrema.

3. Macroscopic Elastic Constants

Properties related to failure, including strength and the degree of localization of damage, are sensitive to flaw statistics, especially the number and spatial distribution of extreme flaws. In the elastic regime, on the other hand, the effects of geometrical irregularity ought to be more moderate. Elastic constants measure a spatially averaged response, in which extremes carry only a small weight. Thus in [13] it was shown that Young's modulus in the primary load-bearing direction of 3D woven composites can be predicted well by combining rules of mixtures with crude estimates of the effects of random tow misalignment or waviness. In fact, the 3D woven composites studied in [12–14] behave in the elastic regime much like laminates. The idea of simple models for elastic constants is pursued in this section in a complete description of the elastic properties of the same class of 3D woven composites.

The emphasis in this section is on predicting *macroscopic* composite elastic properties, i.e., properties applicable over gauge lengths larger than the characteristic scale of the pattern of tows in the reinforcement. Experimental methods have been developed for characterizing the waviness of nominally straight tows, which are in practice far from straight. Tow waviness leads to reduction of the effective axial modulus of a single tow. A simple estimate of this softening is then incorporated in a model of the composite, in which spatially averaged composite properties are estimated by averaging the properties of constituent tows of different orientations.

The simple approach espoused in this section follows orientation averaging models presented for 3D composites many years ago [18-20]. More recent variants appear in [21] and [22]. The primary goal of this paper is to test how well macroscopic elastic constants can be predicted by such approximations for the current generation of 3D woven composite panels, provided tow irregularity is accounted for in an appropriate, spatially averaged way. Computationally, the models require nothing more than the inversion of a 9×9 matrix. Conceptually, they have the immense advantage of simplicity, which should be contrasted with the large computations that follow from finite element formulations of the same task.

While the simple approach works very well for predicting the in-plane macroscopic properties of flat panel specimens, in other problems a more complete description of the stress distribution throughout the composite is required. Important problems of this class include modeling the elastic properties of three-dimensionally

reinforced parts of complex shape; and analyzing the random distribution of loads in individual reinforcing tows when the tows are irregular. For these problems, finite element or similarly laborious computations are inevitable. The formulation of a new finite element model called the "Binary Model," which is designed to deal most efficiently with these and other problems, was presented in [23]. In Section 4, the calibration of the Binary Model for elastic problems is described in full and it is used to model statistical aspects of the composites studied here.

3.1 Experimental Data

Since the warp weavers generally contain a small fraction of the total fibers, the reinforcement is dominated by the orthogonal arrays of stuffers and fillers and is therefore approximately orthotropic. Detailed modeling confirms orthotropic symmetry over gauge lengths exceeding several tow diameters, even in the presence of local irregularities in tow positioning (Section 4). Therefore, macroscopic elastic properties are given by nine Voigt elastic constants, C_{ij}. With x_1 lying in the stuffer direction, x_2 in the filler direction, and x_3 in the through-thickness direction,

$$\begin{vmatrix} \sigma_1 \\ \sigma_2 \\ \sigma_3 \\ \tau_{23} \\ \tau_{31} \\ \tau_{12} \end{vmatrix} = \begin{vmatrix} C_{11} & C_{12} & C_{13} & 0 & 0 & 0 \\ C_{21} & C_{22} & C_{23} & 0 & 0 & 0 \\ C_{31} & C_{32} & C_{33} & 0 & 0 & 0 \\ 0 & 0 & 0 & C_{44} & 0 & 0 \\ 0 & 0 & 0 & 0 & C_{55} & 0 \\ 0 & 0 & 0 & 0 & 0 & C_{66} \end{vmatrix} \cdot \begin{vmatrix} \varepsilon_1 \\ \varepsilon_2 \\ \varepsilon_3 \\ \gamma_{23} \\ \gamma_{31} \\ \gamma_{12} \end{vmatrix} \quad . \tag{6}$$

The constants C_{ij} are often determined from measurements of Young's modulus and Poisson's ratio for uniaxial loading in each of the directions x_1, x_2, and x_3 together with measurements of the shear moduli G_{23}, G_{31}, and G_{12} (e.g., [24]):

$$[S_{ij}] = [C_{ij}]^{-1} \tag{7a}$$

$$[S_{ij}] = \begin{vmatrix} 1/E_1 & -\nu_{12}/E_1 & -\nu_{23}/E_1 & 0 & 0 & 0 \\ -\nu_{12}/E_1 & 1/E_2 & -\nu_{23}/E_2 & 0 & 0 & 0 \\ -\nu_{13}/E_1 & -\nu_{23}/E_2 & 1/E_3 & 0 & 0 & 0 \\ 0 & 0 & 0 & 1/G_{23} & 0 & 0 \\ 0 & 0 & 0 & 0 & 1/G_{31} & 0 \\ 0 & 0 & 0 & 0 & 0 & 1/G_{12} \end{vmatrix}, \tag{7b}$$

where E_i is Young's modulus for loading in the direction x_i, ν_{ij} is Poisson's ratio for the concomitant contraction in the direction x_j, and use has been made of the symmetry relation

$$\nu_{ij}/E_i = \nu_{ji}/E_j \quad . \tag{8}$$

In this work, the engineering constants E_1, E_2, ν_{23}, ν_{31}, and ν_{12} were determined by conducting uniaxial tension tests in the in-plane directions x_1 and x_2. Dog-bone specimens were used in these tension tests, with gauge sections approximately 10 mm × 20 mm x (specimen thickness). The through-thickness modulus E_3 was deduced from tests in which specimens were loaded in compression in the direction x_3 between flat platens. Since the in-plane dimensions of the compression specimens far exceeded their thicknesses, the in-plane strains in the compression tests remained approximately zero. The load-displacement data therefore yielded the stiffness matrix element C_{33}. Young's modulus E_3 was calculated from this value of C_{33} and the measured values of E_1, E_2, and ν_{ij} using Eq. (7). Test calculations showed that the uncertainty in E_3 due to measurement errors in the other engineering elastic constants was typically ~ 5%. Shear moduli were not measured. Some values taken from other work will be used to assess predictive models below.

In many of the tension tests, full-field strain maps were obtained by moiré interferometry. The moiré fringe maps always revealed significant nonuniformity in surface strain distributions. Fringes formed by in-plane displacements (i.e., displacements on x_1-x_2 planes) parallel to the load correspond to the pattern formed by warp weaver extrema at the surface being observed (e.g., Fig. 8a). The surface is revealed as an approximately periodic pattern of relatively soft and hard patches (shown by locally high or low fringe densities), with lattice parameters commensurate with the tow spacings. However, the pattern is always imperfect: significant, nonperiodic irregularity exists in the details of the strain distributions. In-plane displacements transverse to the load were almost always very small, leading to very sparse fringe systems and indicating very small Poisson's ratios (e.g., Fig. 8b).

Fringes formed by displacements on through-thickness sections by loads in the direction x_1 are typified by Fig. 9. Displacements in the loading direction reveal fairly uniform strain (Fig. 9a); whereas displacements in the through-thickness direction reveal

highly nonuniform strain (Fig. 9b). Relatively hard areas in Fig. 9b are directly correlated with warp weavers on the surface being examined.

Taking account of the roughly periodic patterns exemplified by Fig. 8a, in-plane Young's moduli representative of macroscopic strains were obtained by averaging strains over an area of approximately 10 mm × 10 mm. The in-plane Poisson's ratio was deduced from the total displacement across the specimen in the direction of the contraction, averaged over a length of approximately 10 mm along the load axis. The through-thickness modulus E_3 and Poisson's ratio ν_{13} were determined from the total displacement in the through-thickness direction.

The measured elastic constants are reported in Table 4. In a few cases, multiple tests were run to establish representative deviances. For all constants, the deviance was typically 5-10%. Factors contributing to the deviance will be discussed below.

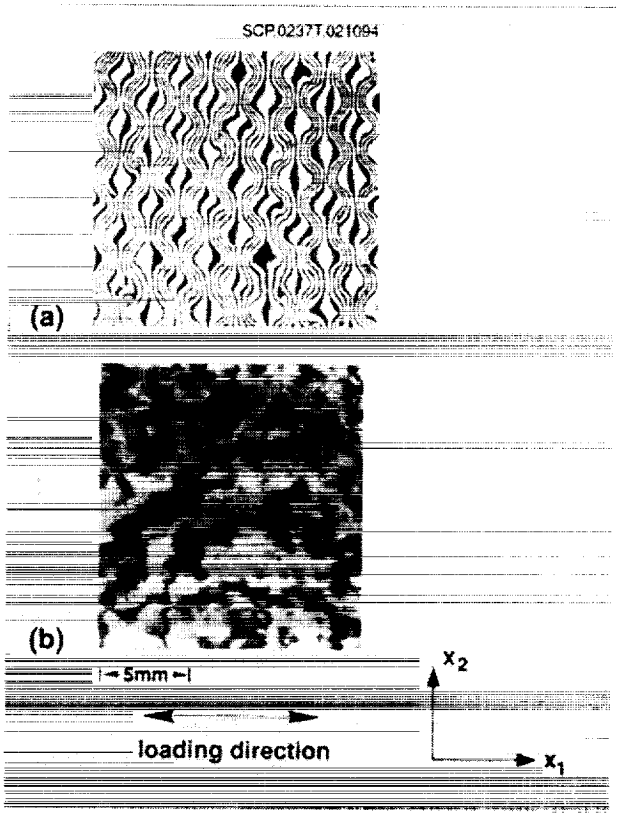

Figure 8. Moiré fringe patterns formed on an in-plane surface (x_1-x_2 plane) of a specimen of composite *h*-O-2 under uniaxial loading in the direction x_1. (a) Displacement in the direction x_1. (b) Displacement in the direction x_2.

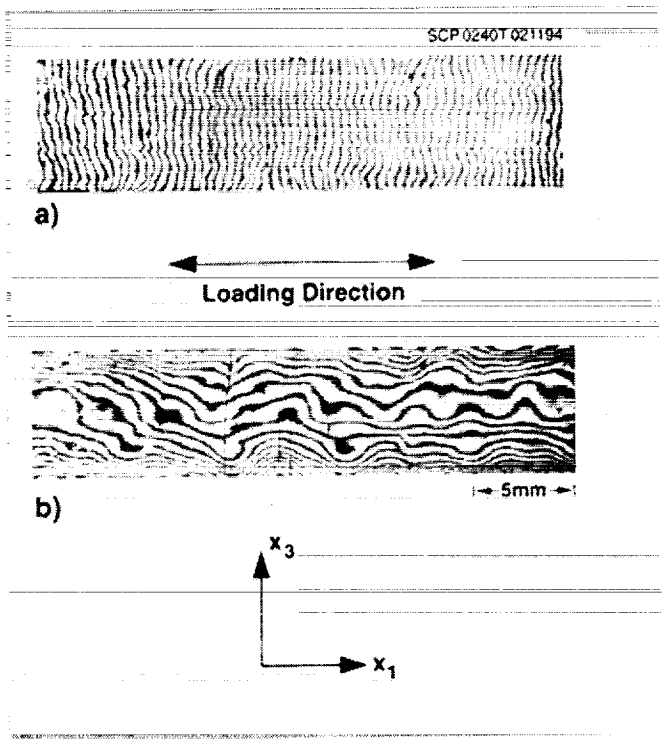

Figure 9. Moiré fringe patterns formed on a through-thickness section (x_1-x_3 plane) in a specimen of composite *h*-L-1 under uniaxial loading in the direction x_1. (a) Displacement in the direction x_1. (b) Displacement in the direction x_3.

3.2 An Orientation Averaging Model

Macroscopically averaged elastic constants have been estimated in the past for both 2D and 3D composites of stiff, continuous fibers in a soft matrix by simple "orientation averaging" models [18–22]. In these models, small volumes in which all fibers are aligned are treated as unidirectional composites. The whole composite becomes a 3D tessellation of transversely isotropic grains or domains whose orientations depend on the reinforcement architecture. Macroscopic properties are evaluated by averaging the response of the body to applied loads, usually under the assumption of either uniform stresses or, more often and more successfully, uniform strains. Such models are not particularly good for polycrystals containing highly anisotropic grains. It is likely that they owe their success for the continuous fiber composites studied so far to the high degree of long-range order that exists therein among the orientations of small volumes of fibers. Whether they will serve well in 3D composites containing short segments of multi-oriented tows remains to be assessed.

Table 4. Measured and Predicted Composite Elastic Constants

Composite Label	E_1 (GPa)			E_2 (GPa)			E_3 (GPa)		
	Expt.	OA[a]	OAW[b]	Expt.	OA[a]	OAW[b]	Expt.	OA[a]	OAW[b]
l-L-1	30±6	36.8	-		38.7		5.7	9.0	
l-L-2	28.5	34.9	29.4		47.6	22.8	5.9	7.0	6.9
l-T-1	27	47.3	41.3		59.5	40.1	8.0	9.4	9.4
l-T-2	39	43.5	37.1		51.6	34.0	7.9	7.0	7.0
l-O	30±2	51.9	45.4	45.5±1.5	63.9	62.6	7.0±1	13.7	13.7
h-L-1	85±8	91.5	88.6	43.8	56.2	40.8	16±2	12.1	12.1
h-L-2	80	81.2	77.6	42.3	55.0	20.9	14.0	10.2	10.1
h-T-1	79	88.6	87.0	42.5	54.4	50.2	13.8	12.8	12.8
h-T-2	72	85.1	82.4	45.8	57.6	48.8	13.9	11.2	11.2
h-O-1	88	93.1	93.0	39.9	56.4	50.8	15.4	17.3	17.3
h-O-2	69±5	83.8	82.5	41.6	55.9	54.2	22.3	20.4	20.4

Composite Label	ν_{12}			ν_{23}			ν_{13}		
	Expt.	OA[a]	OAW[b]	Expt.	OA[a]	OAW[b]	Expt.	OA[a]	OAW[b]
l-L-1	0.024	0.023			0.216		0.22	0.607	
l-L-2	0.11	0.027	.037		0.310	.225	0.50	0.457	.436
l-T-1	0.048	0.020	.022		0.243	.200	0.375	0.541	.527
l-T-2	0.21	0.027	.031		0.325	.267	0.37	0.428	.406
l-O	0.053	0.034	.032		0.183	.180	0.49	0.184	.173
h-L-1	0.061	0.034	.041		0.266	.237		0.456	.450
h-L-2	0.13	0.035	.065		0.298	.221	0.45±.05	0.425	.411
h-T-1	0.054	0.033	.035		0.248	.240		0.486	.483
h-T-2	0.097	0.033	.036		0.280	.262		0.443	.437
h-O-1	0.055	0.051	.054		0.192	.184		0.190	.189
h-O-2	0.07	0.052	.052		0.158	.156		0.157	.155

Composite Label	G_{12} (GPa)			G_{23} (GPa)			G_{31} (GPa)		
	Expt.	OA[a]	OAW[b]	Expt.	OA[a]	OAW[b]	Expt.	OA[a]	OAW[b]
l-L-1		2.3	-		2.1	-		6.0	-
l-L-2		2.4	2.4		2.2	2.2		3.2	3.2
l-T-1		3.0	3.0		2.7	2.7		5.6	5.6
l-T-2		2.6	2.6		2.4	2.4		3.1	3.1
l-O		3.1	3.1		2.8	2.8		2.7	2.7
h-L-1	6.2[c]	5.4	5.4		4.1	4.1		7.1	7.1
h-L-2	5.8[c]	4.6	4.6		3.6	3.6		5.3	5.3
h-T-1	5.6[c]	5.3	5.3		4.0	4.0		7.8	7.8
h-T-2	5.7[c]	5.0	5.0		3.9	3.9		6.2	6.2
h-O-1	5.0[c]	5.4	5.4		4.1	4.1		4.7	4.7
h-O-2		4.9	4.9		4.0	4.0		4.4	4.4

[a]Orientation Averaging Model of Section 3.2: straight fibers
[b]Orientation Averaging Model amended for out-of-plane waviness of stuffers and fillers
[c]Ref. [25]

Property Estimates for Individual Tows

The properties of the individual domains, i.e., of a unidirectional composite, can be estimated from the local fiber volume fraction and the fiber and matrix properties. In this work, five different closed form approximations were assessed for estimating the properties of unidirectional composites, including rules of mixtures and four models from the literature which offer more realistic partitioning of stress between fibers and matrix [22, 26-28]. Each method offers estimates in terms of the elastic constants of the fibers and resin of the five independent elastic constants available for the unidirectional composite when it is considered to be a transversely isotropic body. Of the five models, only Hashin's composite cylinder model [26] permits transverse isotropy in the fibers themselves; all the others treat the fibers as isotropic.

The resin and fiber properties used in this study are listed in Table 5. The properties of the resins were measured in [12] and [13]. The properties of S2 glass fibers, which are assumed isotropic, were taken from the literature (e.g., [24]) and manufacturer's data sheets*. The properties of AS4 carbon fibers, which are far from isotropic, were deduced by Naik [29] from the measured properties of a unidirectional AS4/3501-6 composite with V = 0.6 (Hercules† data sheet) using a finite element model of a composite of fibers in a square array. (Choosing a square array is hardly ideal, since it violates isotropy normal to the fibers. However, ensuing estimates of the properties of 3D composites will not be noticeably affected by such a minor consideration, as will become apparent below.) The value given in parentheses for the axial modulus of AS4 fibers is that given independently in the manufacturer's data sheets for bare AS4 fibers.†

Details of a comparison of the different models for the unidirectional composite are presented in Appendix B. Young's modulus and Poisson's ratio for loading in the fiber direction are essentially the same for all models and well approximated by the rule of mixtures. However, the transverse modulus, Poisson's ratio in the plane of isotropy, and the shear moduli all change significantly when the fiber anisotropy is taken into account. Therefore, Hashin's model with anisotropic fiber properties was used in further modeling.

---

* Owens Corning Glass Co., Detroit, Michigan.
† Hercules Inc., Salt Lake City, Utah.

Table 5. Fiber and Resin Elastic Constants

Fibers

	Axial Young's Modulus E_f (GPa)	Axial Poisson's Ratio ν_f	Axial Shear Modulus G_f (GPa)	Transverse Young's Modulus E_{ft} (GPa)	Transverse Poisson's Ratio[a] ν_f
AS4 carbon fibers	235 (250)	0.25	55	17	0.27
S-2 glass fibers	85	0.22	-[b]	-[b]	-[b]

Resin

	Young's Modulus E_r (GPa)	Poisson's Ratio ν_f
Tactix 138	3	0.3
Shell 1895	3.7	0.3

[a]Poisson's ratio in planes of isotropy
[b]S2 glass assumed isotropic

Orientation Averaging—Ideal Geometry

For orientation averaging, each 3D woven composite is divided into stuffer, filler, and two warp weaver domains occupying fractions A_α of the total composite volume (α = s, f, w_1, or w_2 for stuffer, filler, or either weaver domain; $\sum_\alpha A_\alpha = 1$).

Each domain is characterized by an orientation along which the fibers within it are presumed to lie. Tow waviness does not enter into the definition of these orientations, but will be introduced separately. Thus all fibers within the stuffer or filler domains are assumed to be parallel to the x_1-axis or x_2-axis respectively. While warp weavers are always assumed to be piecewise straight and lie within x_1 - x_3 planes, their orientations are defined differently for angle and orthogonal interlock weaves. For angle interlock weaves, the fibers occupying domain w_1 form an angle of 45° with the x_1-axis; while the fibers occupying domain w_2 form an angle of -45° with the x_1-axis. In angle interlock weaves, domains w_1 and w_2 are occupied by equal numbers of fibers. For orthogonal interlock weaves, domains w_1 and w_2 are assumed to contain fiber segments parallel to the x_1 axis and parallel to the x_3 axis respectively in the proportions a_1:t in composite *h*-O-1 or $2a_1$:t in composites *l*-O or *h*-O-2, where a_1 is the center-to-center spacing of fillers ($a_1 \approx 1/p$). The assignment of orientations for the warp weavers is crude but adequate,

because their contribution to overall properties is limited by their relatively low volume fraction.

Let $C^{(\alpha)}$ denote the stiffness matrix for domain α, i.e. the matrix of stiffness constants determined for the appropriate unidirectional composite by Hashin's model in the local coordinate system (x, y, z) in which the x-axis lies along the fiber direction. The composite stiffness matrix C is approximated by

$$C_{ij} = \sum_{\alpha} A_\alpha \overline{C}_{ij}^{(\alpha)} \tag{9}$$

where $\overline{C}^{(\alpha)}$ denotes $C^{(\alpha)}$ transformed into the composite coordinate system (x_1, x_2, x_3) of Fig. 1. This transformation is a well-known result of tensor algebra (e.g. [30]). Equation (9) is an exact representation of the composite if all three domains α = s, f, and $w = w_1 \cup w_2$ suffer equal strains under macroscopically uniform applied loads. Whether domain strains are in fact equal depends on the reinforcement architecture and the state of applied stress. An assessment of the effect of using other assumptions about the distribution of domain strains is deferred to the Discussion.

Equation (9) and Hashin's model for estimating $C^{(\alpha)}$ allow the composite elastic constants C to be estimated from the properties of the constituent fibers and resin. The solutions are closed by specifying the domain volume proportions A_α. In practice, it is difficult to specify A_α a priori, because of the complex geometry of resin pockets and voids between tows. In the following work, A_α was simply equated to the fiber fraction f_α of Table 2. To justify this assignment, the sensitivity of estimates of composite elastic constants to the choice of A_α was assessed by varying A_s with $A_w = f_w$, $\sum_\alpha A_\alpha = 1$, and total fiber fractions preserved by setting $V_\alpha = f_\alpha V/A_\alpha$ (with V the measured total fiber volume fraction). Within the bounds imposed on A_s by requiring $V_\alpha \leq 0.8$ for each domain, no composite elastic constant deviated by more than ~ 2%.

Engineering elastic constants computed via Eq. (9) and using Hashin's model for anisotropic fibers are compared with the experimental measurements in Table 4. Agreement is excellent for the shear modulus G_{12} and good for most other entries. However, the in-plane Young's moduli E_1 and E_2 are consistently overestimated by the orientation averaging model, while the in-plane Poisson's ratio ν_{12} is underestimated. The through-thickness modulus E_3 and Poisson's ratio ν_{13} are significantly high in some cases and significantly low in others. Nearly all of these variances can be attributed to geometrical irregularity.

The Influence of Stuffer and Filler Waviness

The most important effect of tow waviness on elastic properties is to reduce the axial stiffness of a tow. In the Orientation Averaging model, Young's modulus in the fiber direction in domain α is knocked down by a factor $\eta^{(\alpha)} \leq 1$, which can be estimated from the distribution of out-of-plane misalignment angles. Consider an axially loaded wavy tow as a sequence of misoriented unidirectional composite segments bearing equal stresses in the load direction.† The spatially averaged Young's modulus $\langle E_x^{(\alpha)} \rangle$ of such a tow is given by

$$\langle E_x^{(\alpha)} \rangle = \left\{ \int_{-\infty}^{\infty} \frac{f_\xi(\xi) d\xi}{\bar{E}_x^{(\alpha)}(\xi)} \right\}^{-1} \tag{10}$$

where $\bar{E}_x^{(\alpha)}(\xi)$ is Young's modulus for a unidirectional composite under a load oriented at angle ξ to the fiber direction x. A simple and adequate expression for $\bar{E}_x^{(\alpha)}(\xi)$ is (e.g., [27]).

$$1/\bar{E}_x^{(\alpha)}(\xi) = \frac{\cos^4\xi}{E_x^{(\alpha)}} + \cos^2\xi \sin^2\xi \left(\frac{1}{G_{xy}^{(\alpha)}} - \frac{2\nu_{xy}^{(\alpha)}}{E_x^{(\alpha)}} \right) + \frac{\sin^4\xi}{E_y^{(\alpha)}} \tag{11a}$$

$$\simeq \frac{1}{E_x^{(\alpha)}} + \left(\frac{1}{G_{xy}^{(\alpha)}} - \frac{2\left(1+\nu_{xy}^{(\alpha)}\right)}{E_x^{\alpha}} \right) \xi^2 \qquad \text{(small } \xi\text{)} \tag{11b}$$

where $E_x^{(\alpha)}$, $E_y^{(\alpha)}$, $G_{xy}^{(\alpha)}$, and $\nu_{xy}^{(\alpha)}$ are engineering elastic constants for a unidirectional composite when load and fibers are both aligned along the x-axis. With the integral in Eq. (10) evaluated for f_ξ of Eq. (5b), the knockdown factor $\eta^{(\alpha)}$ is just

$$\eta^{(\alpha)} = \langle E_x^{(\alpha)} \rangle / E_x^{(\alpha)} \tag{12a}$$

$$\simeq \left\{ 1 + \sigma_\xi^2 \left[\frac{E_x^{(\alpha)}}{G_{xy}^{(\alpha)}} - 2\left(1 + \nu_{xy}^{(\alpha)}\right) \right] \right\}^{-1} \qquad \text{(small } \sigma_\xi\text{)}. \tag{12b}$$

† Detailed simulations of load distributions confirm the validity of assuming uniform stress along an individual wavy tow, rather than uniform strain (Section 4.4). However, the differences found in waviness effects when Eq. (10) is based on isostrain conditions in a wavy tow are minor (zero to order ξ^2). Appendix A of [23] also demonstrated that the highly anisotropic tows in typical polymer composites deflect laterally by shear rather than bending; and this is a much more important distinction. Thus the analysis preferred here differs from that appropriate to isotropic wavy layers in a soft matrix [31].

The term multiplying σ_ξ^2 in Eq. (12b) vanishes if the domain α is isotropic. It takes a value near 40 for the composites studied here. Equations (11b) and (12b) fall within 5% of Eqs. (5b), (10), and (11a) for $\sigma_\xi \leq 10°$. For smaller angles, Eq. (12b) can be further simplified to

$$\eta^{(\alpha)} \approx 1 - \sigma_\xi^2 \left[\frac{E_x^{(\alpha)}}{G_{xy}^{(\alpha)}} - 2\left(1 + \nu_{xy}^{(\alpha)}\right) \right]. \tag{12c}$$

Waviness knockdown factors computed for stuffers and fillers without the approximations of Eq. (12b) or (12c) are listed in Table 3. The stiffness loss is 2–20% for stuffers and 5-50% for fillers.

Waviness knockdowns for stuffers and fillers are incorporated in the estimates for 3D woven composite properties by substituting $E_x^{(\alpha)} \rightarrow \eta^{(\alpha)} E_x^{(\alpha)}$ and $\nu_{xy}^{(\alpha)} \rightarrow \eta^{(\alpha)} \nu_{xy}^{(\alpha)}$ in the stuffer and filler domains in the Orientation Averaging Model. The latter substitution preserves the symmetry relations between Young's moduli and Poisson's ratios. The resulting composite predictions are listed in Table 4 under the heading "OAW". The agreement with experimental data is significantly improved. In many cases, the remanent discrepancy between prediction and experiment is less than the scatter in the experimental data and in data reported by different laboratories for the same materials. Nevertheless, in many cases, the predicted in-plane Young's moduli remain higher than the experimental data.

The Influence of Warp Weaver Crimp

Since warp weaver crimp is so severe, a meaningful lower bound to its effect can be found by the extreme assumption that the axial modulus $E_x^{(w)}$ of the warp weavers is reduced to the value $E_z^{(w)}$ of their transverse modulus. Symmetry relations are preserved by the substitution $\nu_{xy}^{(w)} \rightarrow \nu_{yz}^{(w)}$. Some composite elastic constants predicted with these conditions are compared in Table 6 with predictions for warp weavers of ideal geometry. Young's modulus E_1 is only weakly affected by weaver crimp, as is E_2 (not shown in Table 6). The through-thickness modulus E_3, Poisson's ratio ν_{13}, and the shear modulus G_{31} are more substantially affected, falling to values near those expected for a 2D laminate. Other Poisson's ratios and shear moduli are insignificantly affected.

Table 6. Effects of Warp Weaver Crimp

Composite Label	E_1 (GPa)		E_3 (GPa)	
	OAW[a]	OAWW[b]	OAW[a]	OAWW[b]
l-L-1	36.8	35.7	9.0	5.6
l-L-2	29.4	28.9	6.9	5.9
l-T-1	41.3	40.2	9.4	6.7
l-T-2	37.1	36.8	7.0	6.2
l-O	45.5	42.1	13.7	6.9
h-L-1	88.6	87.6	12.1	9.7
h-L-1	77.6	77.0	10.2	8.8
h-T-1	87.0	85.7	12.8	9.6
h-T-1	82.4	81.6	11.2	9.3
h-T-1	93.0	90.0	17.3	9.6
h-O-2	82.5	80.0	20.4	9.2

Composite Label	ν_{13}		G_{31} (GPa)	
	OAW[a]	OAWW[b]	OAW[a]	OAWW[b]
l-L-1	0.607	0.323	6.0	2.2
l-L-2	0.436	0.320	3.2	2.3
l-T-1	0.527	0.306	5.6	2.6
l-T-2	0.406	0.325	3.1	2.4
l-O	0.173	0.310	2.7	2.7
h-L-1	0.450	0.299	7.1	4.7
h-L-1	0.411	0.313	5.3	4.0
h-T-1	0.483	0.294	7.8	4.6
h-T-1	0.437	0.311	6.2	4.3
h-T-1	0.189	0.317	4.7	4.7
h-O-2	0.155	0.308	4.4	4.4

[a]Orientation Averaging Model amended for out-of-plane waviness of stuffers and fillers

[b]as for OAW but with extreme softening of warp weavers

Bending

For many purposes, it will be accurate enough to represent any of the 3D woven composites studied here as orthotropic and homogeneous. However, in bending applications, the coarseness of typical tows suggests that account must be taken of the sequence in which stuffers and fillers appear through the thickness (e.g. Fig. 2). This

effect can be measured as the ratio χ_j (j=1,2) of the flexural rigidity estimated for the actual layer sequence to that estimated under the assumption of through-thickness homogeneity. The required ratio follows easily from the distribution of layer stiffnesses and stresses in pure bending.[1] For a symmetric through-thickness sequence and bending about the x_j-axis (j=1,2), the bending moment M_j is given by

$$M_j = \int_{-t/2}^{t/2} \sigma_j(x_3) x_3 dx_3 . \tag{13}$$

Ignoring the modest effect of transverse stresses, the ratio χ_j is well approximated by

$$\chi_j = \frac{4}{3t} \sum_{i=1}^{n_a+1} \left(u_i^3 - u_{i-1}^3\right) E_j^{(\alpha_i)} \Big/ \frac{t^2}{6} E_j \tag{14a}$$

$$= \sum_{i=1}^{n_a+1} \left[\left(\frac{u_i}{t/2}\right)^3 - \left(\frac{u_{i-1}}{t/2}\right)^3\right] E_j^{(\alpha_i)} / E_j \qquad (j=1,2) \tag{14b}$$

where E_j is Young's modulus in direction x_j for the composite; and $E_j^{(\alpha_i)}$ is Young's modulus in direction x_j for the individual layer (or tow domain) α_i. The moduli $E_j^{(\alpha_i)}$ are either the axial or transverse Young's modulus predicted for a unidirectional composite; the former knocked down by the factor $\eta^{(\alpha_i)}$ to allow for tow waviness.

Values computed for χ_j by Eq. (14) are summarized for all the composites in Table 7. Since fillers are always the outermost plies, χ_2 exceeds unity (bending about the x_1 - axis) while χ_1 is less than unity (bending about the x_2 - axis).

Given χ_1 and χ_2, the flexural rigidities E_{f1} and E_{f2} that should be used to predict the response to pure bending under the assumption that the composite is homogeneous can be estimated from the in-plane moduli E_1 and E_2. Results for E_{f1} are compared in Table 7 to values deduced from the linear portions of bending experiments. The predictions are consistently higher than the available data. The discrepancy can be attributed to overestimates in E_1, since the proportional discrepancies in E_1 (Table 4) and E_{f1} (Table 7) are nearly the same. Thus, the effects of inhomogeneity are well estimated by Eq. (14).

[1]The ratio χ_j is to be applied as a correction factor to the OAM, which already contains estimates of the effects of warp weavers. The influence of warp weavers on the correction factor itself must be negligible.

Table 7. Flexural Rigidity

Composite Label	Factor for Inhomogeneity		Flexural Rigidity E_{f1}[a](MPa)	
	χ_1[a]	χ_2[b]	expt.	prediction[c]
l-L-1	0.79	1.19	20	29
l-L-2	0.78	1.15	-	23
l-T-1	0.78	1.17	-	32
l-T-2	0.79	1.18	-	29
l-O	0.78	1.17	-	35
h-L-1	0.85	1.24	72	75
h-L-2	0.89	1.14	-	69
h-T-1	0.85	1.25	63	74
h-T-2	0.89	1.16	63	73
h-O-1	0.84	1.25	60	78
h-O-2	0.89	1.16	-	73

[a]bending about the x_2-axis
[b]bending about the x_1-axis
[c]Equation (14)

3.3 Discussion of Macroscopic Elastic Constants

3.3.1 In-Plane Properties

The in-plane elastic properties are essentially those of a 0/90° laminate, with relatively minor modifications due to the through-thickness reinforcement and tow irregularity. Thus Poisson's ratio ν_{12} is very small, because the fillers resist transverse contraction when loading is parallel to the stuffers; and ν_{12} and the in-plane Young's moduli E_1 and E_2 are dominated by the axial stiffness of the stuffers and fillers. Consequently, using rules of mixtures rather than Hashin's model for tow domain properties leads to very similar predictions of the composite elastic constants E_1, E_2, and ν_{12} (Appendix B). On the other hand, the in-plane shear modulus G_{12} is matrix dominated: it is very nearly equal to the axial shear modulus predicted for the stuffers and fillers. The rule of mixtures leads to an underestimate for G_{12} (Appendix B).

The in-plane elastic constants E_1, E_2, and ν_{12} are influenced significantly by waviness in stuffers and fillers, but negligibly by waviness in the warp weavers.

3.3.2 Other Elastic Constants

The orientation of the warp weavers and any crimp in them is much more significant for the through-thickness composite modulus E_3, Poisson's ratios ν_{13} and ν_{23}, and the shear modulus G_{31}. As tow orientations would suggest, the highest values of E_3 are found for orthogonal interlock weaves. Similarly, ν_{13} and ν_{23} are less than Poisson's ratio for the matrix for orthogonal interlock weaves, but are quite high in angle interlock weaves. The warp weavers resist through-thickness contraction in the former architecture, but abet it in the latter. Of the shear moduli, only G_{31} depends on the warp weavers: no axial strains arise in any segments of warp weavers under shear strains γ_{12} or γ_{23}.

3.3.3 Unresolved Discrepancies Between Theory and Experiment

When out-of-plane stuffer and filler waviness and warp weaver crimp are accounted for, predicted and measured composite elastic constants agree in most cases to within experimental error. However, the tendency is still for predicted in-plane Young's moduli to be too high, especially for composites *l*-T-1, *l*-0, and *h*-O-2; while experiment and theory occasionally disagree significantly in either direction for the through thickness modulus E_3 and Poisson's ratio ν_{13}.

The remaining overestimate of in-plane moduli is very likely to arise from unaccounted irregularity in stuffers and fillers. Only out-of-plane waviness was measured and modeled, yet other forms of distortions can also be found. Many consist of inconstancy in the aspect ratios of tow cross-sections. In some composites, especially layer-to-layer angle interlocks, this was manifested as tapering, oscillating skirts along the sides of stuffers or fillers, giving them a shape reminiscent of long flatworms. In all composites, aspect ratios are also disrupted by "pinching," i.e., locations where a tow is flattened by lateral loads during processing. Other possible irregularities include yarn twist, which is assumed zero in accord with the weaver's specifications; and in-plane waviness. Unfortunately, it is *virtually impossible* to measure all such irregularities, or even to identify them clearly in specimens. Indeed there will very likely always be some uncertainty in the degree of irregularity existing in textile composites. It is consequently unrealistic to expect to predict even in-plane elastic constants to within better than ~ 10%.

While a 10% uncertainty will usually be deemed quite acceptable in a prediction based on constituent properties, the situation for out-of-plane properties is more

challenging. Three distinct problems exist. (i) The isostrain assumption is wrong in the through-thickness direction, as clearly borne out by moiré data such as Fig. 9b. Model calculations that allow a natural partitioning of loads between warp weavers and the rest of the composite appear in Section 4. They demonstrate that the isostrain assumption exaggerates the influence of warp weavers, by not allowing the rest of the composite to relax around them. (ii) The volume fraction, $f_w V$, of warp weavers depends on the crimp factor, c_w, of Table 1 via Eq. (1). The crimp factor can be measured quite well on average, but it may fluctuate throughout the material to a degree determined by the consistency of the weaving process. The local values of c_w are the most likely cause of measured values of E_3 being higher than predictions in several instances in Table 4. (iii) Waviness and other distortions are relatively severe for warp weavers. Knockdowns of the effective axial stiffness of warp weavers to values near the transverse tow stiffness are implied in several cases studied.

Unfortunately, it is difficult even to categorize the forms of distortion exhibited by warp weavers, let alone to measure them all. However, rough estimates show that the effects of warp weaver irregularity on E_3, ν_{13}, and G_{31} are of similar magnitude to the effects of relaxing the isostrain condition. Thus, when through-thickness property estimates are required in composite design, the simple Orientation Averaging Model with isostrain conditions might just as well be used, with suitably stated levels of uncertainty. Table 4 suggests that an uncertainty of ~ 20% is typical for current 3D woven composites.

4. Details of Stress Distributions via the Binary Model

In Section 3, it was shown that the macroscopic elastic properties of flat panels of woven composites with three-dimensional (3D) reinforcement can be successfully modeled by simply formulated, computationally trivial models. The term macroscopic here refers to a length scale λ that is much larger than the characteristic dimensions of the reinforcement; e.g. center-to-center tow spacings. In typical woven or braided composites, $\lambda \sim$ 1-10 mm. For macroscopic properties, the influence of the reinforcement architecture can be dealt with by orientation averaging, a method with a long history [18-21,32]. Further, if the through-thickness fibers are much less numerous than the in-plane fibers, as preferred in many skin or sheet applications [33,34], the woven composites behave macroscopically in the elastic regime essentially as laminates.

However, some important problems concerning 3D composites in the elastic regime cannot be solved by simple models. One such problem is the question of how irregularity in tow alignment might affect the distribution of loads throughout the composite. Random tow waviness will cause soft spots where tows are highly misaligned. Neighboring tows will be excessively stressed. The question then arises of the extent to which uneven load distribution can affect the onset of tow failure.

A second problem concerns the treatment of reinforcement architectures that are much more complicated than those in the flat panels studied here. Indeed, one of the great promises of woven and braided textiles is the formation of integral structures to near net shape. Typical examples from weaving technology include hollow box beams, in which the upper and lower faces are rich in longitudinal tows for tensile and compressive strength, while the side faces contain mainly $\pm 45°$ tows for shear [35]; and integrally woven skin/stiffener panels for airframes (e.g., [36]). In such structures, tows pass continuously from one part to another; e.g. from face to face in the box beam or from skin to stiffener in the airframe panel. At the critical junctions between parts, tows follow complicated, interlocking paths with no semblance of laminae. The isostrain assumption underlying the orientation averaging method may be invalid here. Nor can the material be modeled as elastically homogeneous. The scale over which critical stress variations occur is no longer significantly greater than the tow separation. A new model is needed to predict the stress distributions in all tows in such junctions and in other regions of geometrical complexity.

An appropriate model was formulated in a prior contract [37] to deal not only with such complex problems in the elastic regime but also with the problems of damage tolerance, localization/nonlocalization transitions, and fatigue damage accumulation. Based on extensive, detailed observations of failure mechanisms in [12,13,14], a new model containing two types of constitutive elements, called the "Binary Model," was proposed. A numerical solution based on the finite element method was outlined.

The Binary Model contains various parameters describing the physical properties of fibers and resin and the reinforcement geometry, both ideal and irregular. Some parameters may be specified a priori, using independently acquired data; others must be evaluated by calibrating the Binary Model against experimental data. This section deals in detail with the calibration process for 3D woven composites in the elastic regime. It also deals with the statistics of load distribution in randomly wavy tows. The effect of load unevenness on first tow failure is assessed.

The calibration procedure is based on the flat panel interlock weaves studied under this contract. All calculations presented here are for those eleven composites, which are identified by the composite labels shown in Table 1.

4.1. The Binary Model of Interlock Weaves

In the Binary Model, the axial properties of tows are represented by two-noded line elements, while the transverse stiffness, shear stiffness, and Poisson's effects of the composite are represented by solid "effective medium" elements. The element size is chosen to be the largest that preserves a one-to-one correspondence between the positioning of tows in the composite and in the model; the topology of the tow pattern is preserved with the minimum degrees of freedom. Calculations with the Binary Model usually involve hundreds or thousands of effective medium and tow elements. When dealing with realistic, irregular tow geometry, the volume modeled is usually considerably greater than the minimum repeating unit or "unit cell" from which the ideal tow geometry could be generated by translation operations.

A typical fragment of a composite as it is represented by the Binary Model is shown in Fig. 10. The example illustrated is an orthogonal interlock weave. While the composite remains elastic, the nodes of stuffer and filler tow elements coincide with those of the effective medium elements, indicated in Figure 10 by black dots. In modeling

progressive failure, tow nodes near a site of tow failure are allowed to displace relative to effective medium nodes to mimic tow sliding [37].

The warp weavers in an interlock weave are modeled here very simply. Warp weaver tow elements are coupled to the rest of the composite solely via springs that connect them to fillers (Fig. 10). The coupling springs allow relative displacement in the x_3 direction only.

Node patterns have been generated for all eleven angle interlock weaves. Complete details are provided in Appendix A. The node patterns can be regarded as defining the weave architecture. They reflect the specifications provided by the manufacturer.

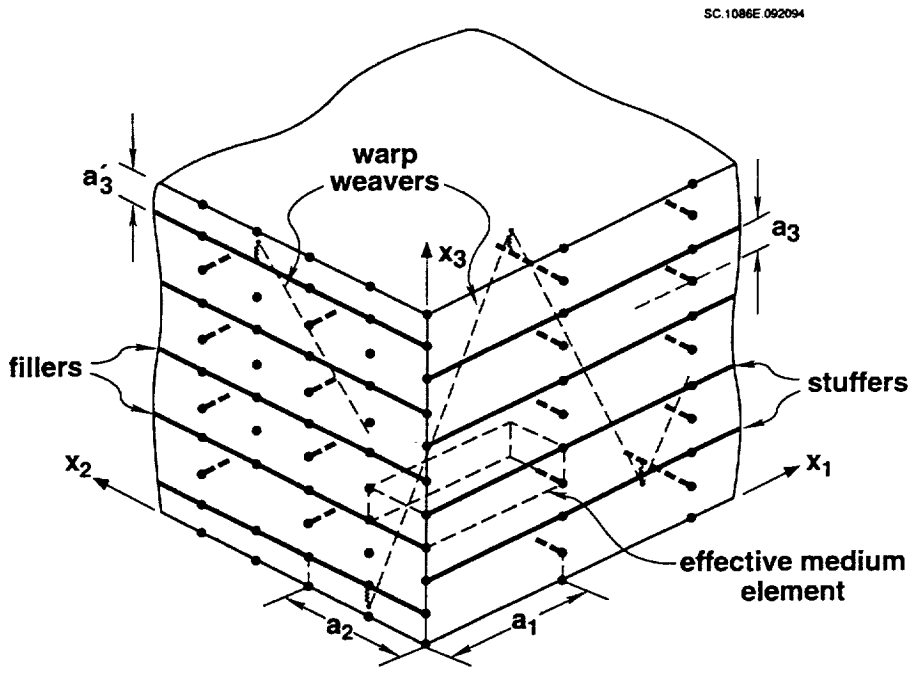

Figure 10. Modeling elements, dimensions, and coordinate system for the Binary Model. The illustrative case is a fragment of a through-the-thickness angle interlock composite.

The mechanical response of the assemblage of effective medium elements, tow elements, and springs exemplified by Fig. 10 is computed by the finite element method. The virtual work principle can be expressed as

$$\int_V \underset{\sim}{\sigma} : \delta\underset{\sim}{\varepsilon}\, dV + \Sigma \underset{\sim}{Q} \cdot \delta\underset{\sim}{l} = \int_S \underset{\sim}{T} \cdot \delta\underset{\sim}{U}\, dS \qquad (15)$$

where $\underset{\sim}{\varepsilon}$ and $\underset{\sim}{\sigma}$ are the strain and stress tensors of the effective medium and V is its volume. The second term on the left hand side of Equation (15) is the virtual work pertaining to all the tow elements and springs. The vector $\underset{\sim}{l}$ denotes the length and orientation of a tow or spring element, while $\underset{\sim}{Q}$ denotes the force acting along it. The displacements $\underset{\sim}{u}$ are given on S_u and the tractions $\underset{\sim}{T}$ are given on S_T, where S_u and S_T are subregions of the external surface S satisfying $S_u \cap S_T = \varnothing$ and $S_u \cup S_T = S$.

In the current formulation, all effective medium elements are represented as eight noded isoparametric solid elements. An updated Lagrangian formulation allows effective treatment of the large deformations expected in later modeling of composite failure. Details of the updated Lagrangian formulation will be given when that work is presented.

4.1.1 Composite Dimensions for Modeling

In modeling macroscopic elastic properties, it is paramount to get the right count of fibers in each orientation. In Section 2, it was argued that the total count is estimated most reliably from the total fiber volume fraction, V, and the proportions by volume f_s, f_f, and f_w of all fibers that belong to stuffers, fillers, and warp weavers ($f_s + f_f + f_w = 1$). The fraction V can be measured experimentally. The proportions f_s, f_f, and f_w are assumed not to change during consolidation and are calculated from the weaver's specifications. Details of these calculations and values for V, f_s, f_f, and f_w for the subject composites are to be found in Section 2 and Tables 1 and 2.

For predicting macroscopic elastic properties by orientation averaging methods, the only information required about tow spacing is the distribution of stuffers and fillers through the thickness, which affects the flexural rigidity. However, when composites are analyzed by the Binary Model, the average tow spacings in all directions must be specified. The required dimensions a_1, a_2, a_3, and a'_3 are illustrated in Fig. 10. They define the separations of the centers of gravity of tows in a composite of ideal geometry. The in-plane separations must be consistent with the measured total volume fraction V and the fractions f_s and f_f. Thus

$$a_1 = \frac{n_s + 1}{f_f V y_f \rho_f t} \tag{16a}$$

and

$$a_2 = \frac{n_s}{f_s V y_s \rho_s t} \tag{16b}$$

where n_S is the number of layers of stuffers, y_S and y_f are the yields (length per unit mass) of the stuffer and filler yarns, ρ_S and ρ_f are densities of the fibers in the stuffers and fillers (both 1800 kg/m^3 for AS4 graphite), and t is the measured composite thickness. The through-thickness dimensions a_3 and a'_3 fix the separations of layers of fillers or stuffers, which are important mainly in bending applications. They are determined via estimates of the average thicknesses t_S and t_f of stuffers and fillers in the through-thickness direction, where $t_f = 2a'_3$ and $t_f + t_s = 2a_3$. If the stuffers and fillers are compacted in processing to equal degrees, then

$$\frac{t_s}{t_f} = \frac{y_f e}{y_s p} \tag{17a}$$

where e and p are the numbers of ends (stuffers) or picks (fillers) per unit length measured normal to the tow direction; while

$$(n_s + 1)\, t_f + n_s t_s = t \quad . \tag{17b}$$

Hence,

$$a_3 = \frac{t}{2} \frac{p y_s + e y_f}{(n_s + 1)\, p y_s + n_s e y_f} \tag{18a}$$

and

$$a'_3 = \frac{t}{2} \frac{p y_s}{(n_s + 1)\, p y_s + n_s e y_f} \tag{18b}$$

For the eleven composites studied in here, values of all the quantities appearing on the right hand sides of Eqs. (16) and (18) have been tabulated in Section 2. The resulting values of a_1, a_2, a_3, and a'_3 are listed here in Table 8.

The separations of stuffers and fillers and the composite thickness are the only spatial scales required in modeling the eleven subject composites: the warp weavers are assigned loci midway between columns of stuffers. See Appendix A.

4.1.2 Elastic Constants

The elastic constants of tow and effective medium elements can be estimated from the properties of individual tows, which in turn can be modeled as unidirectional composites. Suitable approximations for the elastic constants of unidirectional composites are available in the literature. Following assessment of their merits in Section 3, two models will be used here: Hashin's model [26], which alone deals adequately with the pronounced anisotropy of graphite fibers; and rules of mixtures, which are the simplest model available and treat the fibers as isotropic. Since unidirectional material is transversely isotropic, the models provide estimates for five independent elastic constants. In the local coordinate system (x, y, z), with the x-axis the fiber direction in any tow, the constants may be chosen to be Young's modulus $E_x^{(UD)}$ and Poisson's ratio $\nu_{xy}^{(UD)}$ for loading along the fibers, the axial shear modulus $G_{xy}^{(UD)}$, and the shear modulus $G_{yz}^{(UD)}$ and Poisson's ratio $\nu_{yz}^{(UD)}$ in planes of isotropy. The superscript UD signifies "unidirectional composite."

Effective Medium Elements

When the axial stiffness of tows has been removed to tow elements in the Binary Model, it remains for the effective medium elements to represent transverse stiffness, Poisson's effect, and shear stiffness. The interlock weaves of Table 9 are dominated in their elastic properties by the stuffers and fillers, which behave elastically much like a 0°/90° laminate (Section 3). For such reinforcement geometry, the effective medium elements account almost entirely for the in-plane composite shear modulus G_{12} and for a large part of the through-thickness composite modulus E_3 and the composite Poisson's ratios ν_{13} and ν_{23}. Other composite elastic constants are determined by the effective medium elements and tow elements acting in combination.

Therefore, effective medium properties should be selected to give good values for the composite elastic constants G_{12}, E_3, ν_{13}, and ν_{23}. Ignoring warp weavers, a typical effective medium element contains one region occupied by part of a stuffer and another

occupied by part of a filler (Fig. 11). Since the fibers in stuffers and fillers lie parallel to the x_1-axis or the x_2-axis, the in-plane composite shear modulus, G_{12}, should be very near the axial shear modulus, $G_{xy}^{(UD)}$, computed for the unidirectional composite. Thus

$$G_{12}^{(m)} = G_{xy}^{(UD)} \quad , \tag{19}$$

with the superscript m denoting the effective medium. Through-thickness loads applied to the composite act transversely to the stuffers and fillers. Thus

$$E_3^{(m)} = E_y^{(UD)} \quad . \tag{20}$$

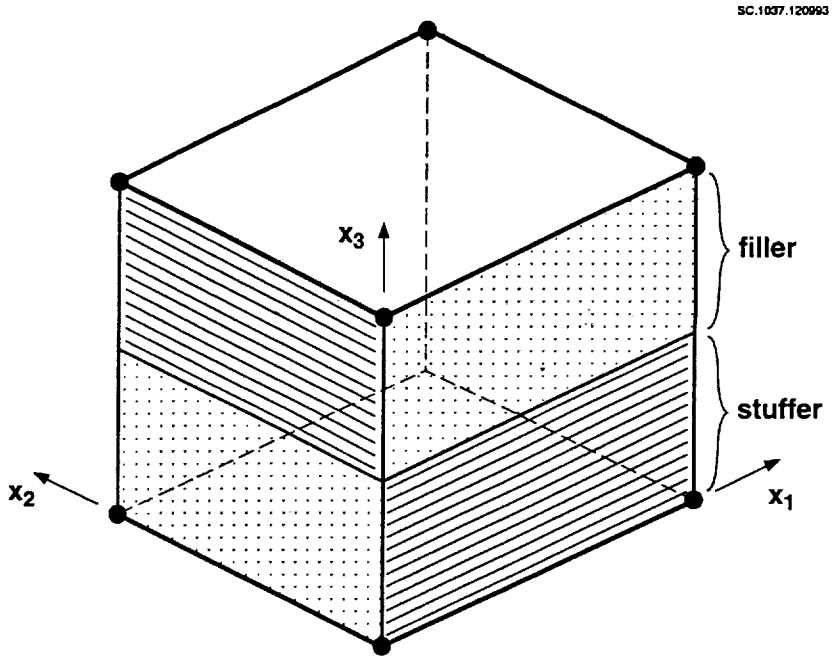

Figure 11. A typical effective medium element contains portions of filler and stuffers tows, within which the fiber direction is as shown.

Poisson's effect for an element such as Fig. 11 might be thought to be more complex. However, there is only a modest difference between $\nu_{xy}^{(UD)}$ and $\nu_{yz}^{(UD)}$; and Poisson's ratios ν_{13} and ν_{23} in the composite are influenced to some extent by the tow elements. Therefore, it is expedient and adequate simply to assign

$$\nu_{13}^{(m)} = \nu_{23}^{(m)} = \nu_{xy}^{(UD)} \qquad (21)$$

For an orthotropic body assembled from elements such as that in Fig. 11, there are nine independent elastic constants. However, most of this symmetry is imposed on the scale of the composite by the tow elements. It is superfluous to require orthotropy in the effective medium. Equations (19) to (21) can be implemented instead by assuming that the effective medium is transversely isotropic, filling out the remaining degrees of freedom by the assignments

$$\nu_{12}^{(m)} = \nu_{xy}^{(UD)} \qquad (22)$$

and

$$G_{31}^{(m)} = G_{23}^{(m)} = G_{xy}^{(UD)} \quad ; \qquad (23)$$

with

$$E_1^{(m)} = E_2^{(m)} = 2\left(1 + \nu_{12}^{(m)}\right) G_{12}^{(m)} \quad . \qquad (24)$$

Whether Eqs. (19) to (24) are optimal should be tested by comparing the predictions of the Binary Model against experiment. This will be done below. Given the dominant role of tow elements, one might guess in advance that an even simpler approach might suffice. Therefore, assignments for an isotropic effective medium following rules of mixtures were also assessed, viz.

$$E_1^{(m)} = E_2^{(m)} = E_3^{(m)} = E_y^{(UD)} \qquad (25)$$

$$\nu_{12}^{(m)} = \nu_{31}^{(m)} = \nu_{23}^{(m)} = \nu_{xy}^{(UD)} \quad . \qquad (26)$$

When irregular geometry is modeled, effective medium elements are no longer perfect cuboids. Nevertheless, the assignments of Eqs. (19) to (26) are retained, with subscripts referring to the global coordinate system.

Tow Elements

Tow elements, being one dimensional, are defined in the Binary Model by a spring constant, $k_\alpha^{(i)}$:

$$F^{(i)} = k_\alpha^{(i)} \varepsilon^{(i)} \qquad (\alpha = s, f, \text{ or } w;\ i = 1, \ldots..,N) \qquad (27)$$

where α = s, f, or w denotes stuffer, filler, or warp weaver; the superscript i refers to one of a total of N tow elements; and F and ε are force and strain. For an ideal geometry, $k_\alpha^{(i)}$ is independent of i. In the presence of tow irregularity, $k_\alpha^{(i)}$ may be a random variable.

Table 8. Tow Spacing Dimensions

Composite Label	Architecture	a_1 (mm)	a_2 (mm)	a_3 (mm)	a'_3 (mm)
(a) Lightly Compacted					
l-L-1	Layer-to-Layer	2.31	2.01	1.41	0.66
l-L-2	Angle Interlock	1.57	1.81	1.37	0.73
l-T-1	Through-the Thickness	1.78	1.88	1.13	0.58
l-T-2	Angle Interlock	1.96	1.91	1.08	0.53
l-O	Orthogonal Interlock	1.91	2.07	0.97	0.51
(b) Heavily Compacted					
h-L-1	Layer-to-Layer	2.06	1.91	0.65	0.21
h-L-2	Angle Interlock	1.30	1.45	0.49	0.18
h-T-1	Through-the Thickness	2.10	1.95	0.66	0.21
h-T-2	Angle Interlock	1.35	1.50	0.45	0.16
h-O-1	Orthogonal Interlock	2.00	1.86	0.67	0.21
h-O-2	Orthogonal Interlock	1.39	1.54	0.46	0.17

The stiffnesses k_s and k_f are prescribed so as to ensure reasonable contributions of stuffers and fillers to the composite Young's moduli, E_1 and E_2. Loads along the x_1 - axis are aligned with the stuffers, transverse to the fillers, and either transverse or at intermediate angles to the warp weavers. Thus to a good approximation

$$E_1 \simeq f_s E_x^{(UD)} + (1-f_s) E_y^{(UD)} \quad . \tag{28}$$

Now there are n_S stuffer tow elements through the thickness, t, of the composite; and $1/a_2$ per unit length in the direction x_2. The stiffness in the x_1 direction in the Binary Model is the sum of the effects of the stuffer tow elements and the effective medium elements. Since the latter fill all space, k_s must satisfy

$$\frac{n_s}{a_2 t} k_s + E_1^{(m)} = f_s E_x^{(UD)} + (1-f_s) E_y^{(UD)} \tag{29a}$$

or

$$k_s = \frac{a_2 t\, f_s}{n_s} \left(E_x^{(UD)} - E_y^{(UD)} \right) \quad . \tag{29b}$$

Similarly

$$k_f = \frac{a_1 t\, f_f}{n_s + 1} \left(E_x^{(UD)} - E_y^{(UD)} \right) \quad . \tag{30}$$

These expressions were derived by ascribing the fractions f_s and f_f of the whole composite volume to stuffers and fillers. The correct total fiber count in each class of tow will be preserved as long as the unidirectional composite properties appearing in Eqs. (29) and (30) are evaluated for a composite of volume fraction equal to V, the *measured* total fiber volume fraction.

The multiplicative factors on the right hand sides of Eqs. (29b) and (30) can be viewed as estimates of the cross-sectional area of a single stuffer or filler. The subtraction of the term $E_y^{(UD)}$ multiplied by this area avoids double counting of the contribution of the effective medium, which occupies all space. This interpretation suggests the alternative prescription for k_α (α = s, f, or w)

$$k_\alpha = D_\alpha \left(E_x^{(UD)} - E_y^{(UD)} \right) \quad , \tag{31}$$

where D_α is the cross-sectional area estimated by any means. Figure 10 suggests writing $t_s a_2$ and $t_f a_1$ for the cross-sectional areas of stuffers and fillers, leading to

$$k_s = t_s a_2 \left(E_x^{(UD)} - E_y^{(UD)} \right) \tag{32a}$$

and

$$k_f = t_f a_1 \left(E_x^{(UD)} - E_y^{(UD)} \right) \quad . \tag{32b}$$

Because of the way various quantities have been defined, the total fractions of the composite volume occupied by stuffers and fillers with cross-sections $t_s a_2$ and $t_f a_1$ are $f_s/(1-f_w)$ and $f_f/(1-f_w)$. Therefore, if Eq. (31) is preferred, the unidirectional composite properties should be evaluated for a composite of volume fraction $(1-f_w)V$, to conserve total fiber counts. With this adjustment, the difference between Eq. (31) and Eqs. (29) and (30) is very small.

The tow cross-sectional area can also be estimated from the fiber volume fraction, the tow yield, and the fiber density f_α for the fibers in tows of kind α (α = f, s, or w):

$$D_\alpha = \frac{1}{y_\alpha V \rho_\alpha} \quad . \tag{33}$$

This estimate in conjunction with Eq. (31) is the most practical if the tows are not nominally straight, i.e., for warp weavers. To conserve total fiber counts, the same fiber volume fraction must be used in Eq. (33) and in calculating the unidirectional composite properties in Eq. (31). The measured total fiber volume fraction V is the obvious choice.

Coupling Spring Constants

The stiffness, k_{wf}, of the coupling springs between fillers and warp weavers (Fig. 10) is defined as

$$k_{wf} = a_1 h_w E_y^{(UD)} \quad , \tag{34}$$

where h_w is the width of the warp weaver where it comes into contact with the filler; and $a_1 h_w$ approximates the contact area. Most composite properties are very insensitive to the value of k_{wf} (see below). Therefore, a crude but effective estimate of h_w is

$$h_w = \sqrt{\frac{1}{y_w V \rho_w}} \quad . \tag{35}$$

Similarly, the unidirectional composite modulus $E_y^{(UD)}$ used in Eq. (34) could be that computed for either filler or warp weaver. Since $E_y^{(UD)}$ is matrix dominated, the end effect on composite properties is barely detectable.

4.2. Calibration of the Binary Model

4.2.1 Ideal Geometry

The effectiveness of the Binary Model was assessed by comparing its predictions of macroscopic elastic constants with experiment and with the predictions of the Orientation Averaging Model of Section 3. This was done first for ideal geometry. Macroscopic properties were computed with the Binary Model for a simulated slab of material whose dimensions were somewhat greater than the largest period of any of the tow patterns shown in Appendix A. The slab contained twelve effective medium elements in the x_1 direction, 10 in the x_2 direction, and $2(n_S+1)$ in the x_3 direction. Thus it also contained 60 n_S stuffer elements representing $5n_S$ stuffers and 130 $(n_S + 1)$ filler elements representing 13 $(n_S + 1)$ fillers. The number of warp weaver elements depended on the architecture, as indicated by Table A.1 and Figure A.2. Because warp weavers only have nodes where they turn, many warp weavers do not have a node on one or both end plane. The load (or force) in any partial warp weaver element left hanging in such cases was equated to that in the same tow at the other end plane.[1] This device maintains reasonable force balance at all warp weaver nodes.

Uniaxial tension or shear loads were imposed by requiring one component of displacement to be uniform on one pair of opposing sides of the slab. All other boundary displacements were allowed to relax to make all other boundary stresses zero. Young's moduli and shear moduli follow trivially from this procedure. However, Poisson's effect is more complex. When uniaxial tension is applied in the stuffer direction, the lateral boundaries of the slab displace nonuniformly. On the sides normal to the fillers, the magnitude of the displacements is much larger at nodes which are not shared by fillers than at nodes which are. The fillers resist lateral contraction very effectively. This boundary effect influenced lateral displacement even in the middle of the slab. Poisson's ratio ν_{12} should in fact be calculated by constraining the sides of the slab normal to the fillers to displace as planes when the *average* normal stress is zero. Since the fillers would dominate the displacement in such a calculation, ν_{12} was defined by the displacement of the nodes shared by fillers when the sides were *locally* stress-free.

[1] This periodic condition applies to some warp weavers only. The simulated slab overall is *not* periodic.

Poisson's ratio ν_{13}, on the other hand, involves lateral displacements in the thickness direction. These are nonuniform in reality. For comparison with the orientation averaging model, ν_{13} was defined by averaging the displacements on the upper and lower surfaces of the slab.

Calculations were performed for all eleven architectures of Table 8. Fiber and resin properties used were those of Table 5; Hashin's model was used to estimate the domain elastic constants $E_x^{(UD)}$, etc.; effective medium elements were defined by Eqs. (20)-(25); and tow elements were defined by Eqs. (29) and (30) for stuffers and fillers and Eqs. (31) and (33) for warp weavers.

Selected composite constants calculated by the Binary Model and the Orientation Averaging Model (from Table 4) are compared with experimental data in Table 9.

The in-plane constants E_1, E_2, and ν_{12} predicted by the two models are in close agreement. The slight differences can be attributed to the larger differences that arise in through-thickness properties. The shear modulus G_{12} is not shown in Table 9: it remains identical to $G_{xy}^{(m)}$ and to the value found in the Orientation Averaging Model (see Table 4).

Experimental values for in-plane Young's moduli tend to be significantly lower than predicted by either model. This is due to tow waviness. Estimates of waviness effects have already been incorporated in the Orientation Averaging Model, and bring predictions reasonably close to data (Section 3). Waviness effects in the Binary Model are dealt with below.

The through-thickness modulus E_3 is generally lower in the Binary Model than in the Orientation Averaging Model. The difference can be explained by considering the strains in warp weavers, which are the main load-bearing tows in the direction x_3. In the Binary Model, the axial strains in the warp weavers can be reduced by shearing strains between warp weavers and the softer, surrounding composite, which lowers E_3. In orientation averaging, isostrain conditions are assumed: the strain in the warp weavers must remain the same as that in the surrounding composite. This leads to a stiffer structure. The predictions of the Binary Model should be regarded in principle as superior to those of the Orientation Averaging Model.

Table 9. Comparison of Orientation Averaging and Binary Models

Composite Label	E_1 (GPa)			E_2 (GPa)			E_3 (GPa)			
	Expt	OA[a]	BM[b]	Expt	OA[a]	BM[b]	Expt	OA[a]	BM[b]	OAWW[c]
l-L-1	30[d]	36.8	36.0		38.7	38.5	6	9.0	6.8	5.6
l-L-2	29	34.9	36.3		47.6	50.1	6	7.0	6.7	5.9
l-T-1	27	47.3	46.4		59.5	59.4	8	9.4	8.4	6.7
l-T-2	39	43.5	44.8		51.6	53.5	8	7.0	7.8	6.3
l-O	30	51.9	48.9	46	63.9	63.7	7	13.7	9.4	6.9
h-L-1	85	91.5	92.0	44	56.2	56.3	16	12.1	11.5	9.7
h-L-2	80	81.2	81.2	42	55.0	55.1	14	10.2	10.2	8.9
h-T-1	79	88.6	88.7	43	54.4	54.5	14	12.8	11.5	9.6
h-T-2	72	85.1	85.3	46	57.6	57.8	14	11.2	11.3	9.3
h-O-1	88	93.1	90.2	40	56.4	56.3	15	17.3	12.5	9.6
h-O-2	69	83.8	81.3	42	55.9	55.9	22	20.4	13.8	9.2

Composite Label	ν_{12}			ν_{13}				G_{31} (GPa)		
	Expt	OA[a]	BM[b]	Expt	OA[a]	BM[b]	OAWW[c]	OA[a]	BM[b]	OAWW[c]
l-L-1	0.02	0.023	0.029	0.22	0.607	0.481	0.323	6.0	2.1	2.2
l-L-2	0.11	0.027	0.022	0.50	0.457	0.476	0.320	3.2	1.9	2.3
l-T-1	0.05	0.020	0.024	0.38	0.541	0.477	0.306	5.6	2.6	2.6
l-T-2	0.21	0.027	0.025	0.37	0.428	0.493	0.325	3.1	2.4	2.4
l-O	0.05	0.034	0.027	0.49	0.184	0.428	0.310	2.7	2.5	2.7
h-L-1	0.06	0.034	0.038		0.456	0.463	0.299	7.1	3.8	4.7
h-L-2	0.13	0.035	0.037	0.45	0.425	0.463	0.313	5.3	3.8	4.0
h-T-1	0.05	0.033	0.037		0.486	0.480	0.294	7.8	4.2	4.6
h-T-2	0.10	0.033	0.036		0.443	0.48	0.311	6.2	3.3	4.3
h-O-1	0.06	0.051	0.040		0.190	0.407	0.317	4.7	4.2	4.7
h-O-2	0.07	0.052	0.043		0.157	0.375	0.308	4.4	4.0	4.4

[a] Orientation Averaging Model of [1].

[b] Binary Model (engineering strain = 0.001).

[c] Orientation Averaging Model of [1] with highly softened warp weavers.

[d] Measurement scatter typically ~ 10% [1].

Experimental values of E_3 are sometimes lower than the predictions of even the Binary Model. This is the effect of warp weaver distortion, which is often quite severe (Section 2). Lower limits to E_3 can be found by reducing the axial modulus of warp weavers to the transverse modulus. The effects in the Orientation Averaging Model are listed in Table 9 under the heading OAWW (taken directly from Table 6). Similar numbers can be obtained in the Binary Model by setting the axial modulus of warp weavers to zero; in which case E_3 for the composite becomes identical to $E_y^{(UD)}$ via Eq. (3). Unfortunately, as discussed in Section 3, it is exceedingly difficult even to measure all forms of warp weaver distortion in current 3D interlock weaves.

Other experimental values of E_3 are *higher* then predicted values. Some of this discrepancy might be experimental error. The through-thickness modulus is relatively difficult to measure. It is also influenced more strongly by the volume fraction of warp weavers, which is more prone to measurement error than the volume fractions of stuffers or fillers. Warp weaver volume fractions depend on a "crimp" or "take-up" factor, which defines the total length of yarn in a unit length of composite. For warp weavers, the crimp factor is large (~ 1-3 for angle interlock and ~ 4 for orthogonal interlock composites - Table 1) and probably subject to substantial variance over lengths comparable to the size of specimens used in this work. Variations in the warp weaver crimp factor would be caused by inconstancy of tension or beating up during weaving. The difficult of measuring warp weaver distortions and crimp factors preempt more accurate agreement of experiment and theory on the value of E_3.

Some significant discrepancies between the two models for ν_{13} and G_{31} can also be accounted for by expected differences in internal load distribution. For example, the Orientation Averaging Model gives high values for ν_{13} for composites *l*-L-1 and *l*-T-1, and low values for composites *l*-0, h-0-1, and h-0-2. The first two values are high because of a trellis or scissor effect: the warp weavers lie at 45° to the load axis. The last three are low because the warp weavers lie parallel to the x_3 axis and strongly resist through-thickness contraction. In the Binary Model, both of these effects are moderated by nonuniform strain distributions. The values of ν_{13} tend away from the extremes implied by the warp weaver geometry and back towards the intermediate values expected for the rest of composite. The same principle is clearly at work in the shear modulus G_{31}. Agreement of the Binary Model with experimental values of ν_{13} is fair. Discrepancies can be attributed largely to warp weaver distortion.

In summary, comparison with experiment shows that the Binary Model predicts the in-plane macroscopic elastic properties of 3D woven sheets with acceptable accuracy *without the use of adjustable parameters*. Comparison with measured out-of-plane elastic constants is made more difficult by warp weaver distortion, which is often severe and difficult to measure, and likely variance in the warp weaver volume fraction. With this caveat, predictions of out-of-plane constants are also very reasonable.

4.2.2 The Effects of Effective Medium and Coupling Spring Assignments

For graphite fibers in epoxy resin at volume fractions typical of textile composites, Hashin's formulae accounting for fiber anisotropy and rules of mixtures assuming isotropic fibers give very similar values for the single tow properties $E_x^{(UD)}$, etc. The sole exception is the axial shear modulus, $G_{xy}^{(UD)}$, which the rule of mixtures underestimates by approximately 30%. Since most composite properties in the Binary Model are dominated by tow elements, which reflect the axial Young's modulus of tows, the simplified prescriptions of Eq. (26) for the effective medium, based on rules of mixtures and assumed isotropy in the effective medium, ought to work quite well. To bear this out, Binary Model predictions based on Eq. (26) were compared with those based on Eqs. (20)-(25), i.e. those listed in Table 9. Of the engineering elastic constants, all Young's moduli and Poisson's ratios differed by a few per cent at most, differences that are well beneath experimental resolution. The composite shear moduli differed by 10-30%. The in-plane modulus G_{12} is the most affected, since it alone is entirely determined by the effective medium. In a reinforcement architecture with in-plane tows aligned in more than two directions, G_{12} would also be dominated by the axial properties of tows and crude treatment of the effective medium would be even more accurate.

The role of the coupling spring constant k_{wf} was tested by arbitrarily doubling its value over that prescribed by Eq. (34). The changes in all composite engineering elastic constants were insignificant.

Thus in the Binary Model, the most important consideration by far is the proper definition of the elastic properties of the tow elements. In other words, macroscopic elastic properties of 3D weaves are dominated by the axial stiffness of tows. The details of the prescription of matrix dominated elements, i.e. the effective medium elements and coupling springs, are relatively unimportant. The same should be true of other

architectures, including 2D and 3D braids, 2D weaves, and the more complex tow arrangements found in integral structures.

4.3 The Effects of Tow Waviness

For the composites studied here, the main irregularity affecting in-plane elastic constants is out-of-plane waviness of nominally straight in-plane tows. In the Binary Model, reinforcement irregularity is introduced by offsetting nodes in the initial, stress-free configuration.

Out-of-plane waviness was modeled by offsetting all stuffer and filler nodes in the x_3 direction only. The amplitude of the offset of the i^{th} such node was

$$\delta_i = \beta_i \, g_\alpha \, a_3 \tag{36}$$

where β_i is a random variable; g_α is a dimensionless amplitude parameter, with α = s or f depending on whether the node lies on a stuffer or filler; and a_3 is defined in Fig. 10. The random variable β_i is distributed according to a symmetric normal distribution with second moment equal to unity. Thus the average magnitude of the nodal offset was $\sqrt{2/\pi} \cdot g_\alpha \, a_3$ (α = s or f). The influence of tow waviness was assessed by varying the parameters g_s or g_f. The statistics of composite properties were computed by the Monte Carlo method. For each pair (g_s, g_f), 20 simulations were executed. In each simulation, values of β_i were assigned by invoking a pseudo-random number generator and then applying Eq. (36) to obtain $\{\delta_i\}$.

No correlation was imposed between the offsets on neighboring nodes. However, if two neighboring nodes had offsets so large that they exchanged places, the simulation was not executed. This filtering sets the practical limit $g_\alpha \leq 0.2$ to the values of the amplitude parameters.

Composite elastic constants were computed by averaging over the ensemble of all simulations. The most significant impact of stuffer and filler waviness is on the in-plane Young's moduli. Representative results are shown in Fig. 12, where the relative magnitude of E_1 is plotted against the stuffer offset amplitude parameter g_s. In Fig. 12a, the plot symbols show computed values found for one architecture for various values of the filler offset parameter g_f. As might be expected, filler offset has very little effect on

E_1, since the fillers are transverse to the load. The continuous curve shows a fitted Lorentzian function, which has the correct functional form at $g_s = 0$ and a physically reasonable form for high g_s.

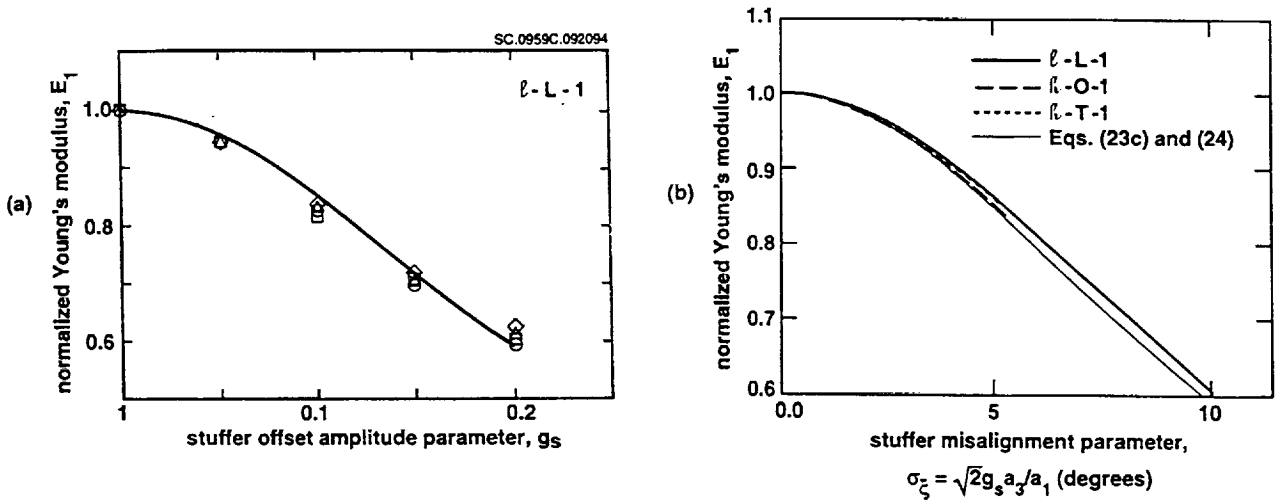

Figure 12. Diminution of the composite Young's modulus E_1 with increasing out-of-plane tow waviness. (a) Binary Model results for composite *l*-L-1. (b) Heavy curves: Binary Model results for composites *l*-L-1, *h*-L-1, and *h*-O-1, with the abscissa normalized as in Eq. (37); fine curve: orientation averaging estimate of Eqs. (38c) and (39).

It is useful in comparing the effects of waviness in composites with different proportions a_1:a_2:a_3 to relate the parameter g_s to a distribution of misalignment angles. Given offsets δ_i and δ_{i+1} on successive nodes, the misalignment of the intervening tow element with respect to the applied load axis may be trivially deduced (Fig. 13). If δ_i follows a symmetric normal distribution of second moment $\mu = g_s a_3$, then δ_{i+1}-δ_i follows a symmetric normal distribution with second moment $\sqrt{2} g_s a_3$; and the misalignment angle ξ, if it is small, follows the same distribution with second moment

$$\sigma_\xi = \sqrt{2}\, g_s a_3/a_1 \quad . \qquad (37)$$

Softening in the stuffer direction is shown as a function of σ_ξ for three composites in Fig. 12b (heavy curves). The curves shown are Lorentzian functions fitted to Monte Carlo results for five values of σ_ξ (or g_s) in each case. The curves show a high degree of consistency, considering the range of total fiber volume fractions and reinforcement architectures represented.

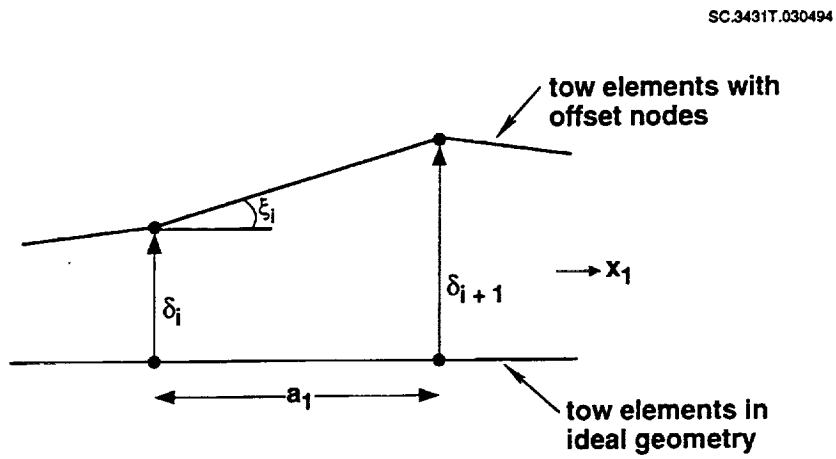

Figure 13. Schematic of misalignment angle implied by specified nodal offsets.

From Eq. (10), the axial modulus of a wavy tow with such normally distributed misalignment angles falls by the factor

$$1-\eta_t = 1-\frac{1}{E_x^{(UD)}}\left\{\int_{-\infty}^{\infty}\frac{e^{-\xi^2/2\sigma_\xi^2}}{\sigma_\xi\sqrt{2\pi}}\frac{d\xi}{\overline{E}_x^{(UD)}(\xi)}\right\}^{-1} \tag{38a}$$

using the notation of this section, where $\overline{E}_x^{(UD)}(\xi)$ is Young's modulus for a unidirectional composite under a load oriented at angle ξ to the fiber direction, x. Using Eq. (11), this gives for small ξ

$$1-\eta_t \approx \left\{1+\sigma_\xi^2\left[\frac{E_X^{(UD)}}{G_{xy}^{(UD)}}-2\left(1+\nu_{xy}^{(UD)}\right)\right]\right\}^{-1} \qquad \left(\sigma_\xi \le 10^\circ\right) \quad ; \tag{38b}$$

$$1-\eta_t \approx 1-\sigma_\xi^2\left[\frac{E_x^{(UD)}}{G_{xy}^{(UD)}} - 2\left(1+\nu_{xy}^{(UD)}\right)\right] \qquad \left(\sigma_\xi \le 3°\right). \tag{38c}$$

The restrictions on σ_ξ shown in Eqs. (38b) and (38c) apply for the degree of anisotropy typical of graphite/epoxy composites. The composite modulus E_1 should fall approximately by the factor

$$\frac{f_s E_x^{(UD)}(1-\eta_t) + (1-f_s)\, E_y^{(UD)}}{f_s E_x^{(UD)} + (1-f_s)\, E_y^{(UD)}} \tag{39}$$

The "orientation averaging" estimate of Eqs. (38b) and (39) has been added to Fig. 12b as a fine curve. The agreement with the results of the Binary Model is very good.

Measurements of typical 3D woven composites show misalignment parameters for stuffers ranging up to $\sigma_\xi \sim 5°$. Figure 12b implies concomitant reductions of up to ~ 15% in E_1. When the estimates of in-plane Young's moduli are reduced using values of σ_ξ measured for each composite, agreement with experiment becomes significantly improved. Since estimates of waviness effects are the same in the Orientation Averaging Model and the Binary Model (Section 3), further details are superfluous.

4.4 The Problem of a Single Wavy Tow

To explore distortions of local stresses due to tow waviness, some calculations were performed for a simplified composite containing a single wavy tow. The composite contained 25 stuffers in a 5 x 5 array with no filler or warp weaver tows. The nodes of the central stuffer in the array were given offsets that followed a cosine curve of amplitude d and wavelength λ (Fig. 14a). Each stuffer was 12 elements long. The spacing of the stuffers and the length of each stuffer element were chosen to be the same as in simulations of composite *I*-L-1. Because of symmetry, the entire body could be loaded uniaxially in the direction x_1 by specifying uniform displacement in that direction over the end planes.

As expected, the stress computed in the elements of the wavy tow varied sinusoidally, being maximum at the ends and center of the specimen, where the element misalignment is least, and minimum in between, where the element misalignment is

greatest. However, the amplitude, σ_λ, of the stress variation was remarkably small compared to the average drop in stress along the tow, $\delta\sigma_t$. This is shown in Fig. 14b, where $\sigma_\lambda/\sigma_t(0)$ and $\delta\sigma_t/\sigma_t(0)$ are plotted against the amplitude d/a_3 of the initial nodal offset, with $\sigma_t(0)$ the load in the tow when it is straight. Thus the load along the tow remains very nearly uniform. Inequality in the effective stiffness of successive tow segments because of their different misalignments is evidently accommodated by easy shear of the effective medium elements. This reflects the high anisotropy of the tows.

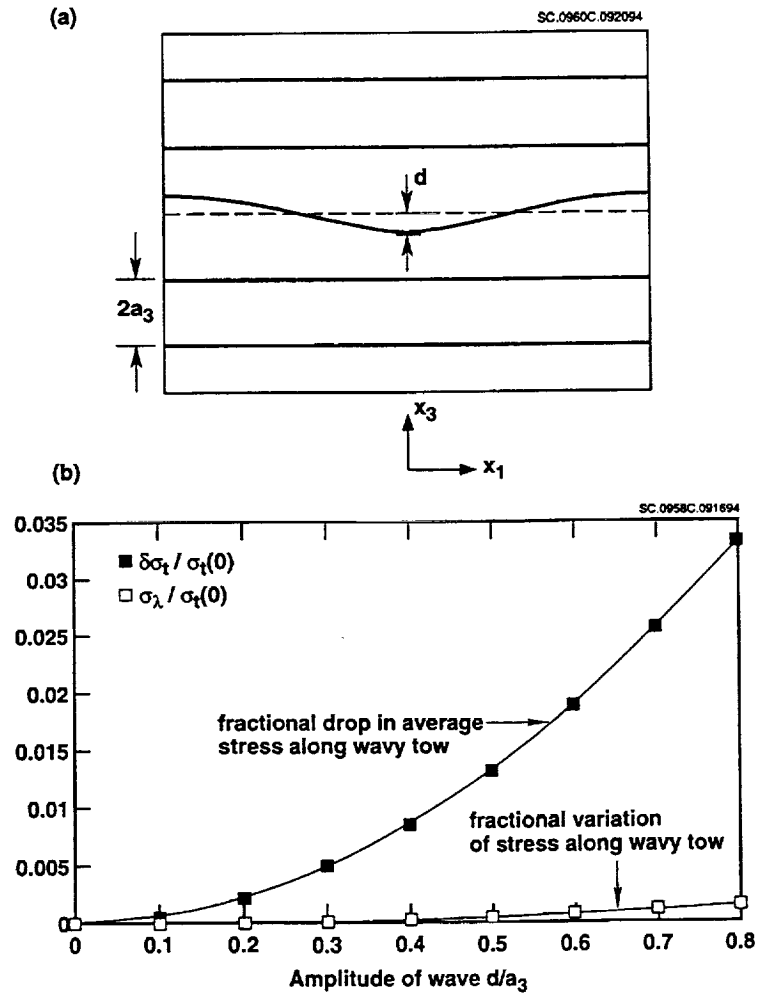

Figure 14. (a) Central section of a simulated composite containing a single wavy tow. (b) Dependence of the average drop, $\delta\sigma_t$, of the stress in the wavy tow and the amplitude, σ_λ, of the variation in stress along the wavy tow with the amplitude of the initial offset. Stresses normalized by the stress in the tow when it is straight. All calculations at fixed applied strain.

Analytical estimates of knockdown factors for the axial tow modulus due to waviness should therefore be based on isostress rather than isostrain conditions in the wavy tow. Isostress conditions were assumed in deriving Eq. (38). However, the approximation of Eq. (38c) turns out also to be correct for isostrain conditions along the wavy tow; and therefore whether isostress or isostrain conditions are assumed *for the purpose of estimating the effects of tow waviness* is inconsequential unless σ_ξ is large.

4.5 Distribution of Loads in Tow Elements - Effect on Strength

4.5.1 Results from the Binary Model

Under in-plane loading along the stuffers, ultimate failure is the result of stuffer failure either by kink band formation in compression or rupture in tension [12,37]. The onset of such local failure events depends in part on the distribution of loads in short segments of the stuffers - the stuffer elements in a Binary Model simulation. The effect of tow waviness on the statistics of load distribution was assessed by analyzing the output of Monte Carlo simulations similar to those described in Section 4.3.

Figure 15(a) shows cumulative probability distributions (cpd's), denoted F_Q, for the forces $|\underset{\sim}{Q}_i|$ in stuffer elements for selected values of σ_ξ, the width of the distribution of stuffer misalignment angles (related to g_s by (Eq. (37)), with the filler waviness parameter $g_f = 0$. The axial stress $\sigma_s^{(i)}$ in the i^{th} stuffer element (in coordinates aligned with the stuffer element) is related to Q_i by the simple proportionality

$$Q_i = \frac{a_2\, t\, f_s}{n_s}\, \sigma_s^{(i)} \tag{40}$$

following Eq. (16b). Each cpd contains 4800 data points (20 simulations; 240 stuffer elements). Results for $g_f > 0$ are very close to those shown for $g_f = 0$: filler waviness has little effect on stuffer loads. The forces are normalized against the average value in each case; and simulations for different values of σ_ξ are further normalized so that the total axial load in the composite was the same in all cases. When $\sigma_\xi = 0$, there is a very slight dispersion in the stuffer element forces, induced by the symmetry-breaking presence of the warp weavers. As σ_ξ increases, the distribution broadens, as expected, and becomes increasingly skewed. Values of σ_ξ between 1° and 5° are found for stuffers in current 3D woven composites (Section 2).

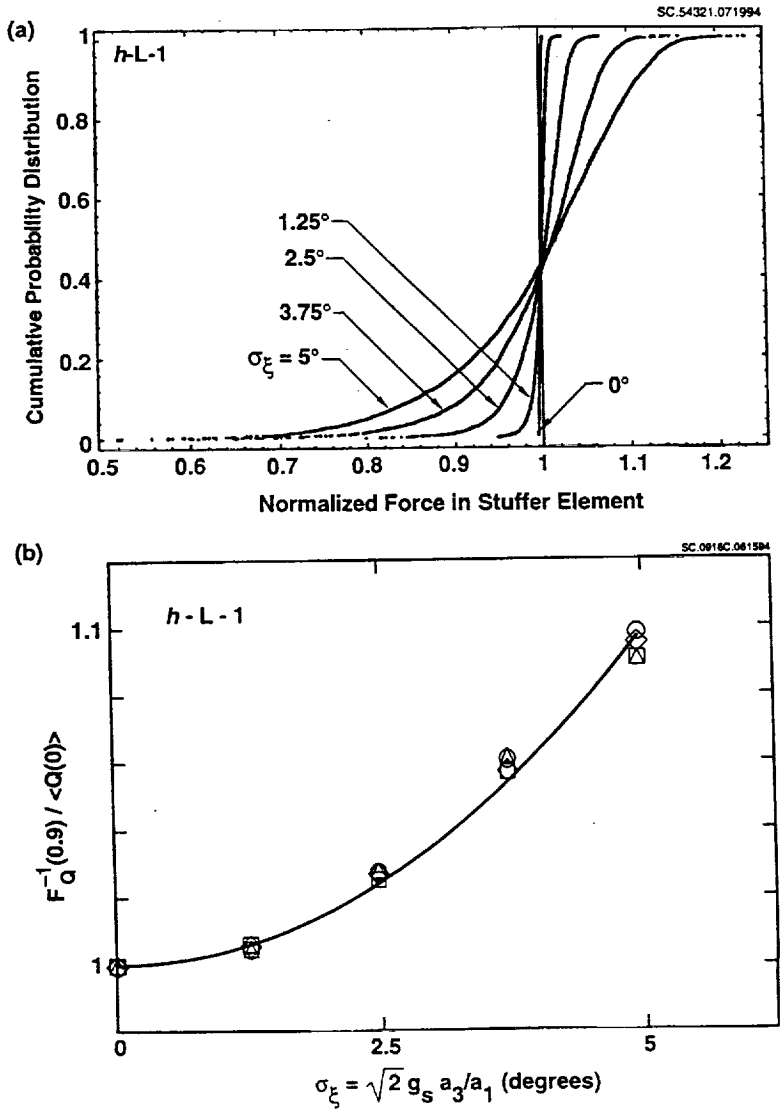

Figure 15. Results of the Monte Carlo simulations for composite h-L-1. (a) Cumulative probability distributions of normalized tow element forces for various values of sx, which is related to the stuffer waviness parameter gs by Eq. (37). (b) Variation of the 90th percentile of tow element forces with sx. The points show results of Monte Carlo simulations for the filler waviness parameter gf = 0, 0.05, 0.1, 0.15, and 0.2. The smooth curve is a fitted parabola.

Analytical approximations to the distributions of Fig. 15(a) will be presented elsewhere. They are based on shear lag analysis of stress redistribution around a misaligned tow segment, and take advantage of the high degree of anisotropy present in typical graphite/epoxy tows. The analytical models confirm that the size of the slab used

in the Monte Carlo simulations reported here should be sufficient to make boundary errors negligible.

The peak load bearing capacity of a typical 3D woven composite specimen is reached when only a few localized tow failures have occurred, which would be represented in Binary Model simulations by just a small fraction of all tow elements. Thus the upper extremity of the cpd of tow element forces is most relevant to strength. The 90th percentile or 0.9 quantile, $F_Q^{-1}(0.9)$, will be taken here as representative of these high values. It rises approximately as the square of σ_ξ, as shown in Fig. 15(b).

Whether uneven load distribution is significant in determining strength depends on how $F_Q^{-1}(0.9)/<Q>$ (Fig. 15b) compares with the width of the distribution of intrinsic flaws. For failure in tension, statistics of intrinsic flaws in tows have not yet been measured. Tow rupture strength in a 3D composite is probably influenced by waviness and damage to fibers during weaving, among other things [12,37]. Since the strength of 3D woven composites is ~ 30% lower than values estimated from tape properties [12,37], one might guess that intrinsic flaws for tensile failure are quite broadly distributed; and therefore that the effects of uneven load distribution are relatively minor. Discussion of the case of compressive failure follows.

4.5.2 The Distribution of Critical Loads for Kink Band Formation

Kink band formation under compressive loading occurs at the critical axial stress σ_c given by Argon's law [38]

$$\sigma_c = \frac{\tau_o}{|\xi|} \tag{41}$$

where τ_o is the shear flow stress for the matrix. Values of ~ 75 MPa are found for τ_o in the composites studied here [12,37]. The stress σ_c can be regarded as a random variable taking a specific value for each tow segment according to its misalignment angle ξ.[1] If ξ

[1] In Section 2 and [9], which dealt with experimental measurements of waviness, the symbol ξ was used to represent a continuously varying misalignment angle along a smooth, wavy tow; while ζ represented extreme values of ξ between successive locations of zeroes of ξ. The reduction in stiffness due to waviness depended on the distribution of ξ. Strength depended on the distribution of ζ. In this section, ξ and ζ become identical because of the piecewise linear representation of tows in the Binary Model.

is normally distributed with zero mean and second moment σ_ξ, then the density function f_c for σ_c must be

$$f_c(\sigma_c) = f_{|\xi|}\frac{d|\xi|}{d\sigma_c}$$

$$= \frac{\tau_o}{\sigma_c^2}\sqrt{\frac{2}{\pi}}\frac{1}{\sigma_\xi}e^{-\tau_o^2/2\sigma_\xi^2\sigma_c^2} \tag{42}$$

The corresponding cpd F_c is

$$F_c(\sigma_c) = \int_0^{\sigma_c} f_c(u)du$$

$$= \mathrm{erfc}\left[\frac{\tau_o}{\sqrt{2}\sigma_\xi\sigma_c}\right] \tag{43}$$

where erfc is the complementary error function. Statistical aspects of kink band failure will be governed by the lowest values of σ_c; or equivalently, low values of F_c. The 10th percentile $F_c^{-1}(0.1)$ can be taken as representative of extreme flaws in specimens of the size tested here. The density f_c has an unbounded mean - the mean is dominated by the very large values of σ_c predicted by Eq. (41) when $|\xi| \to 0$.[2] However, the dispersion of flaw strengths can be gauged by comparing $F_c^{-1}(0.1)$ to the median flaw strength $F_c^{-1}(0.5)$:

$$\frac{F_c^{-1}(0.1)}{F_c^{-1}(0.5)} = \frac{\mathrm{erfc}^{-1}[0.5]}{\mathrm{erfc}^{-1}[0.1]} \approx 0.41 \tag{44}$$

Thus, *independently of* σ_ξ *and* τ_o, flaws for compressive failure by kinking are always broadly distributed in relative strength when misalignment angles are normally distributed. The spread in flaw strength implied for normally distributed ξ by the law Eq. (41) is much greater than the spread in loads because of elastic inhomogeneity (Fig. 15), unless σ_ξ is relatively large (>10°). Recall that σ_ξ is less than ~ 5° for all the composites studied here.

[2] If σ_c is regarded as the strength of a tow element then other failure modes such as fiber collapse would intervene as σ_c rises; and $<\sigma_c>$ would be bounded.

4.5.3 The Distribution of Shear Stresses

The tow elements in the Binary Model support no shear stresses - they are line elements. However, the shear stress in any real tow segment can be estimated from the shear stresses in the effective medium elements surrounding the corresponding tow element in a simulation. For example, in this work each stuffer element is surrounded by four eight-noded effective medium elements. The axial shear stresses τ_{12} and τ_{13} can be evaluated by averaging the values of these stress components at the two integration points in each of the effective medium elements that share nodes with the stuffer element in question; i.e. an average over eight integration points in all.

Figure 16 shows cpd's $F_{\tau_{12}}$ and $F_{\tau_{13}}$ for the two components of axial shear stress τ_{12} and τ_{13} in stuffer segments for the architecture *h*-L-1 and five levels of the stuffer misalignment distribution parameter σ_ξ. The data of Fig. 16 are from the same 20 simulations used to generate Fig. 15. The shear stresses are normalized with respect to the average axial stress in stuffer elements, $\langle Q_i \rangle$, for each value of σ_ξ. Since the stuffers have only out-of-plane misalignments, in keeping with experimental observations, τ_{13} is much greater than τ_{12}. Unlike Fig. 15, Fig. 16 shows significant dispersion in τ_{12} and τ_{13} even when $\sigma_\xi = 0$ (ideal geometry). This is the effect of the through-thickness reinforcement (warp weavers).

Both τ_{12} and τ_{13} can be decomposed into components $\tau_{1j}^{(w)}$ and $\tau_{1j}^{(m)}$ (j = 2,3), the former arising from the effects of warp weavers and the latter, a function of σ_ξ, from stuffer misalignment. A simple estimate of $\tau_{1j}^{(w)}$ is the shear stress found when $\sigma_\xi = 0$, i.e., for perfect stuffer alignment. The function $\tau_{1j}^{(m)}(\sigma_\xi)$ can be found from Monte Carlo simulations in which warp weavers have been omitted (or their stiffness set to zero). Numerical checks show that, to a good approximation,

$$\tau_{1j}(\sigma_\xi) = \tau_{1j}^{(w)} + \tau_{1j}^{(m)}(\sigma_\xi) \tag{45}$$

for each stuffer element when identical sets of pseudo-random element misalignments are used for the simulations with and without warp weavers. If $F_{\tau_{1j}}^{(w)}$ and $F_{\tau_{1j}}^{(m)}$ denote the cumulative probability distributions of $\tau_{1j}^{(w)}$ and $\tau_{1j}^{(m)}$, then from Eq. (45)

$$\left(F_{\tau_{1j}}^{(m)}\right)^{-1} = F_{\tau_{1j}}^{-1} - \left(F_{\tau_{1j}}^{(w)}\right)^{-1} \tag{46}$$

i.e., the distribution of the shear contributions $\tau_{1j}^{(m)}$ for any $\sigma_\xi > 0$ can be obtained from Fig. 16 by subtracting the inverse of the distribution for $\sigma_\xi = 0$ from that for σ_ξ. Thus Figure 16 shows that for $\sigma_\xi > 2°$, which is typical of current woven composites, *the shear stresses induced by the symmetry-breaking effects of warp weavers are much smaller than those due to stuffer misalignment.* This conclusion is reinforced by the observation that the computed axial shear stress τ_{13} is strongly correlated with the misalignment angle, ξ, of any stuffer segment, with $\tau_{13} \approx \xi\, \sigma_s^{(i)}$; and therefore with the knockdown in the axial stress σ_s due to waviness.

The criterion Eq. (41) for kink band formation is based on an estimate of the axial shear stress caused by misalignment. For out-of-plane misalignments,

$$\left|\tau_{13}^{(m)}\right| \approx \sigma_s \left|\xi\right| \quad . \tag{47}$$

The criterion simply states that kink instability occurs when

$$\left|\tau_{13}^{(m)}\right| = \tau_c \quad , \tag{48a}$$

the critical stress for shear flow. The additional axial shear stress due to warp weavers, $\tau_{13}^{(w)}$, lowers the threshold for kinking, which now occurs when

$$\left|\tau_{13}^{(m)} + \tau_{13}^{(w)}\right| = \tau_c \quad . \tag{48b}$$

When $\tau_{13}^{(m)}$ and $\tau_{13}^{(w)}$ have the same sign, this and Eq. (47) give

$$\sigma_k = \frac{\tau_c - \left|\tau_{13}^{(w)}\right|}{\left|\xi\right|} \tag{49}$$

instead of Eq. (41). The same knockdown is found with the simplest assumptions of kink geometry when $\tau_{13}^{(w)}$ is regarded as a remotely applied field [39].

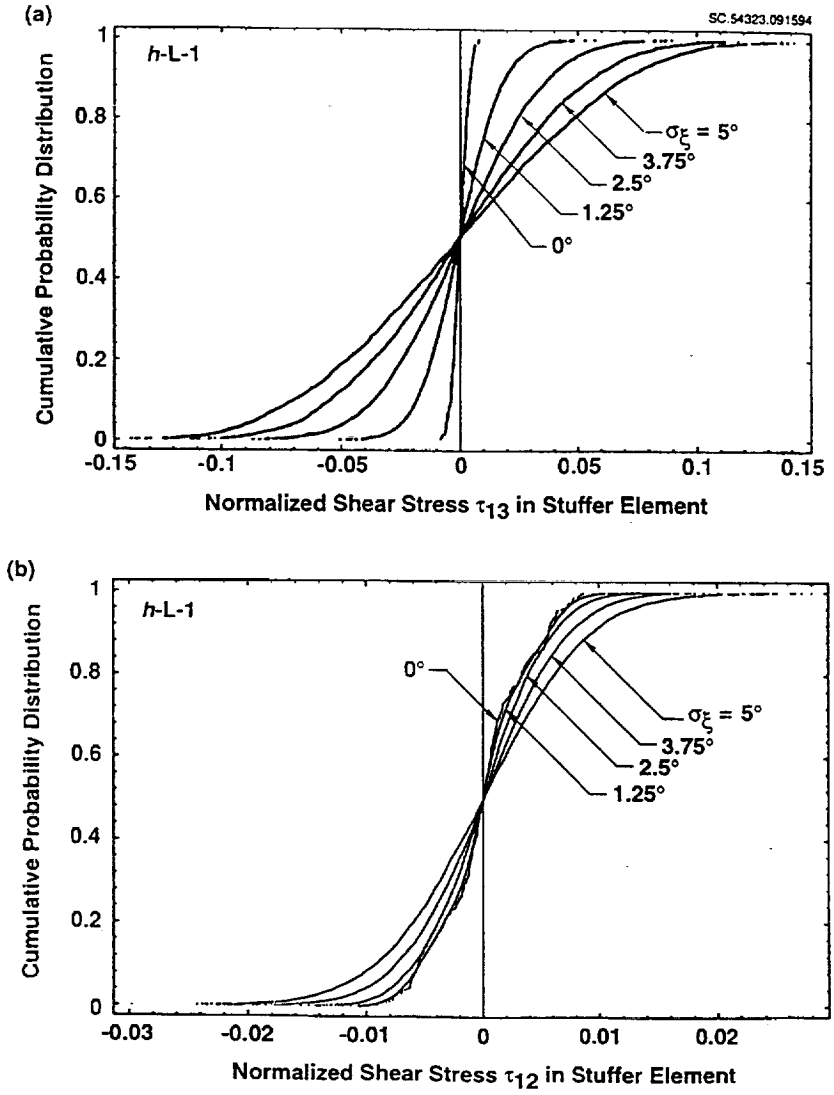

Figure 16. Cumulative probability distributions for shear stresses in stuffers inferred from Monte Carlo simulations of composite h-L-1: (a) t13 and (b) t12. Shear stresses normalized against average axial stress in stuffer elements. The stuffer misalignment parameter sx is defined by Eq. (37).

In the presence of warp weavers, Eq. (49) could be substituted for Eq. (41) in estimating compressive strength. However, since $\tau_{13}^{(w)} << \tau_{13}^{(m)}$ for realistic degrees of misalignment, the *stress effects of the warp weavers on the kink formation criterion are probably beneath the resolution of experiments.* (This is not to say warp weavers have no effect on kinking. They have an essential role in determining ξ, played out mainly during the weaving process - see Section 2.)

5. Fatigue under Compressive Loading

This section pursues the description of the mechanisms of failure of 3D woven interlock composites to compression - compression fatigue. As for monotonic compression (refs. [12,37]; summary below), kink band formation is found to be the principal mechanism. It is influenced by the same geometrical flaws that govern failure in monotonic loading. A formula for the elapsed cycles to first kink band formation is proposed based on the micromechanics of kink formation. Under load control, this leads at once to a formula for fatigue life.

5.1. Summary of Prior Observations in Monotonic Compression

Monotonic failure mechanisms were studied and reported under a prior contract [37]. This summary revises the essential points for understanding fatigue experiments.

Under monotonic compression aligned with the stuffers, several forms of reversible nonlinearity and irreversible damage usually precede formation of the first kink band [12,13]. Some degree of delamination between layers of stuffers and fillers nearly always occurs. If the through-thickness reinforcement is insufficiently stiff (too heavily deformed during consolidation), delamination cracks can grow unstably and premature failure ensues by Euler buckling of delaminated layers. However, in the preferable case of sufficiently stiff (undeformed) warp weavers, all delaminations remain relatively short, and failure by Euler buckling is avoided [12,37].

As long as large scale delamination and Euler buckling are suppressed, as should always be the case in a well manufactured 3D composite, the principal mechanism of compressive failure is kink band formation. The kink bands form in individual stuffers. They nearly always span the entire stuffer, but do *not* generally propagate into neighboring stuffers. There is a strong correlation between sites of kink band formation and the misalignment of the affected tow segment with the applied load. Thus local misalignment acts as a geometrical flaw. According to micromechanical models of kink band formation, for the simplest assumptions of kink band geometry the critical axial stress, σ_k, in the affected tow follows Argon's Law [38,40]

$$|\sigma_k| = \frac{\tau_c}{|\xi|} \tag{50}$$

where τ_c is the critical shear stress for shear flow in the matrix and ζ is the local misalignment angle.[1] Shear flow in these materials is mediated by myriad microcracks, each $\leq 1\mu m$ long, arrayed between adjacent fibers (e.g. Fig. 17). The distribution of strengths of geometrical flaws is related via Eq. (50) to the distribution F_ζ of ζ.

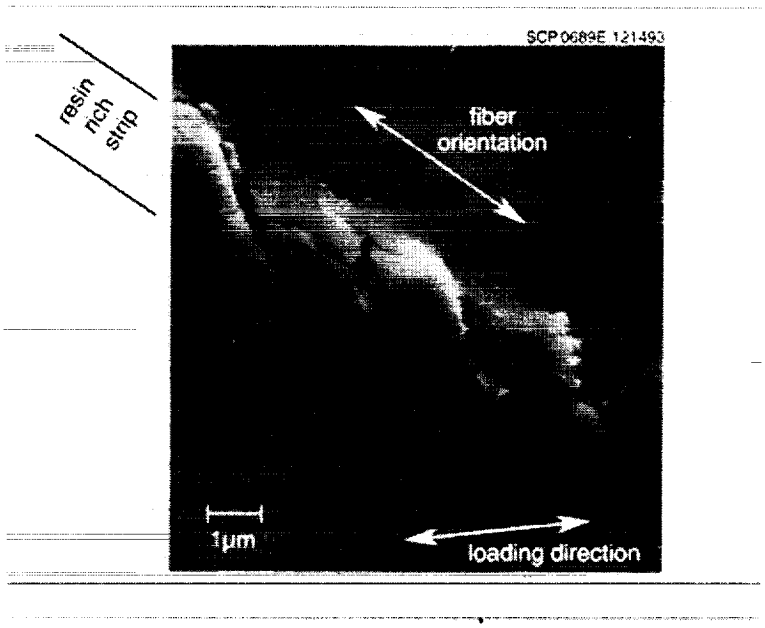

Figure 17. A linear array of microcracks in the resin of a ±45° AS4/1895 laminate, the source of the "plasticity" in Fig. A-1. The array follows the local fiber orientation.

The criterion Eq. (50) was derived for infinite, uniformly misaligned composites. Significant errors could arise in applying it to irregular finite tows in a 3D composite. Yet measured strengths correlate remarkably well with predictions based on Eq. (50), using values for τ_o and ζ obtained from independent measurements [12,37]. Further details of this agreement will be given below.

If finite tow size has no obvious effect on the kinking criterion, it should be inferred that kink instability occurs more or less uniformly over the cross-section of the

[1] Equation (51) introduces slightly different notation from Eq. (41). In fatigue, σ_k and τ_c will change with elapsed cycles and are therefore distinguished from σ_c and τ_o, which are their initial values; while ζ refers, as in Section 2, to an extremum of a continuously varying misalignment angle ξ.

tow, rather than being triggered by some kind of flaw on the tow's surface. This view is also implied by Eq. (50), which is based on the paradigm that compares most favorably with data for laminates [38,40].

The critical stress σ_k can also be knocked down by shear loads induced, even in perfectly aligned tows, by the symmetry breaking effects of warp weavers. However, calculations of stress distributions in the elastic regime show that, in the subject materials, such shear stresses are small compared to those due to misalignment, which are reflected in Eq. (50) as it stands (Section 4). Delamination microcracks between layers of stuffers and fillers permit some degree of barreling in the through-thickness direction, depending on the composite type and the loading configuration [12,37], which might exacerbate the shear stress generated by warp weavers. However, the barreling occurs at strains above that of peak load and therefore cannot influence strength, only strain to failure.

As well as delamination microcracks, shear microcracks are seen in angle interlock composites prior to peak load along the inclined boundaries of warp weavers where they are exposed to view on a machined specimen surface. These shear microcracks also initiate delaminating microcracks along the boundaries of stuffers (aligned tows). The latter are weakly correlated with microbuckling of short segments of stuffers at loads near the proportional limit. The microcracking appears to free the stuffers to buckle out of the surface, inducing kinking. However, this local failure sequence does not occur away from cut surfaces. It involves buckling and kinking deflections in the filler direction, which are evidently suppressed by the fillers' axial stiffness elsewhere. All kink bands revealed in the body of composites by post-mortem sectioning have deflections in the through-thickness direction, normal to the fillers. These are the kink bands that cause failure.

These remarks and the empirical success of Eq. (50) support the simple idea that kinking is essentially determined by a tow segment's misalignment, the axial load it bears, and the material property τ_c.

The statistics of geometrical flaws are also a primary factor in determining compressive strain to ultimate failure, ε_f. Geometrical flaws that are broadly distributed in both strength and space favor noncatastrophic, ductile failure. Thus, values of ε_f measured for lightly compacted composites, which are relatively irregular, have exceeded 15%. In the heavily compacted composites, misalignment angles are much lower and

failure is more brittle, with ε_f never exceeding a few percent.[4] Predicting this transition in ductility requires detailed computational modeling, in which the distribution of geometrical flaws in strength and space, the redistribution of load around a failed tow, and the finite size of the specimen are all considered [23,37].

5.2 Fatigue Experiments and Observations

Dog-bone specimens of the dimensions shown in Fig. 18 were cut by water jet from panels of the eleven materials of Table 1. With this specimen shape, most failure events in both monotonic loading [12,37] and fatigue are confined to the gauge section. Fully unloaded uniaxial compression-compression fatigue (load ratio $R \equiv \sigma_{min}/\sigma_{max} = -\infty$) was imposed at 1 Hz under load control using a 200 KIP test frame with self aligning hydraulic grips. All experiments were conducted in laboratory air of relative humidity 50%. In all tests, the stuffers were nominally aligned with the load axis. Stress/strain data were recorded continuously by a computer controlled acquisition system, reading strain values from a single 1/2 in. (12.7 mm) clip gauge attached to the specimen.

Both the external surfaces and interiors of specimens revealed by sectioning exhibit considerably less microcracking late in fatigue life than is observed under monotonic loading by the attainment of peak load. Notably absent are the greater or lesser delamination cracks found near peak monotonic load between layers of stuffers and fillers. However, some small matrix cracks aligned normal to the load are observed on specimen surfaces. These cracks are open at zero load and close under compression, which suggests that they have relieved tensile residual stresses in the resin. However, they do not appear to penetrate any deeper than the first layer of stuffers and have no apparent role in failure. They should have only a slight effect on Young's modulus, which is dominated by the stuffers.

Stuffers fail in fatigue as in monotonic compression by kink band formation. Figure 19(a) shows a kink band revealed by sectioning an angle interlock specimen. This particular fatigue test ended in run-out after 10^6 cycles, with little hysteresis broadening, suggesting minimal global damage. The low level of global damage has left the kink band in photogenic condition. Microscopy revealed almost no microcracking in its vicinity. The only cracks seen ran along the failed stuffer from both ends of the kink band, but in

[4] Without contradicting the brittle to ductile transition in going from heavily to lightly compacted materials, strains to ultimate failure also depend on the specimen configuration. See [12].

one direction only at each end. Thus the kink band probably caused the microcracking, rather than vice versa.

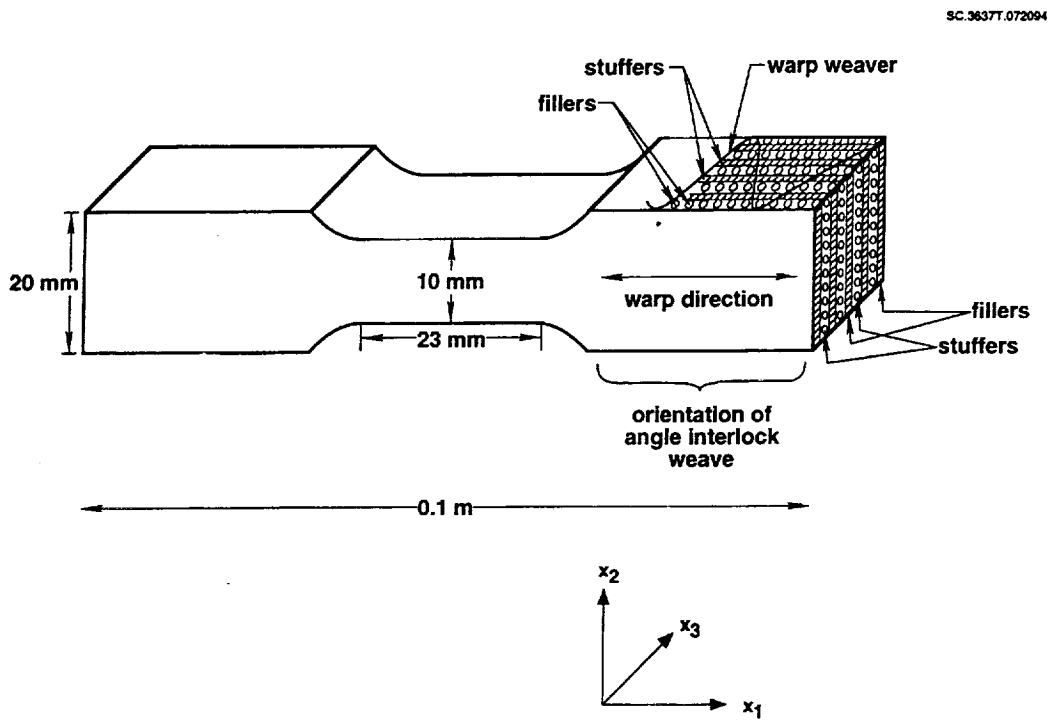

Figure 18. Specimen dimensions, coordinates, and reinforcement orientation.

The kink band in Fig. 19(a) has occurred at a site of high stuffer misalignment. The misalignment is associated with a common configuration of tows (Fig. 19(b)): a warp weaver just beneath the surface in Fig. 19(a) wraps around a filler and presses it into the stuffer, resulting in stuffer crimp. This distortion can arise during either the weaving of the dry fiber preform or from compaction pressure used in consolidating it with resin [12,37]. Figure 19 is one example of a common case. In both monotonic and cyclic loading, the majority of all kink bands have been found at similar sites in all composite types.

Figure 20 shows kink bands found on specimens sectioned just prior to failure. (Failure was presumed to be imminent because of changes in specimen compliance - see next paragraph.) These kink bands are much more complex than that of Fig. 19, suggesting successive waves of kink instability under the high strains achieved at ultimate failure. (See also [37], esp. Appendix D.)

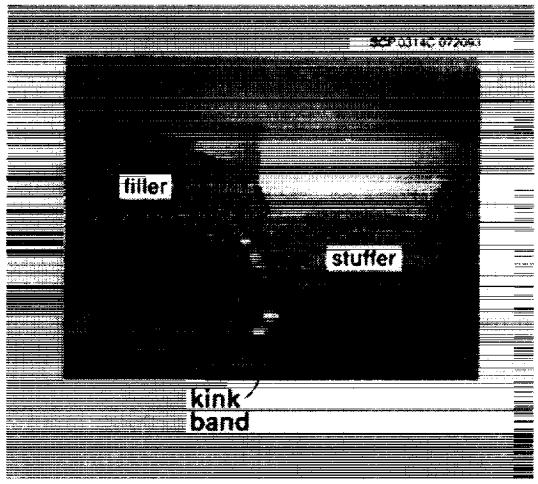

(a)

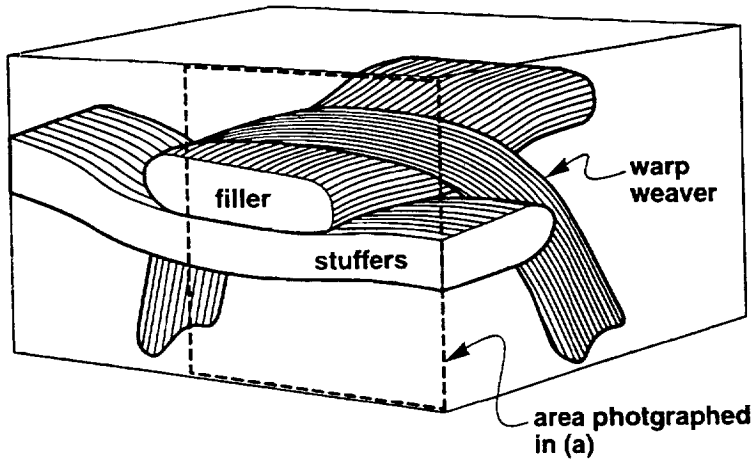

(b)

Figure 19. (a) A kink band in a stuffer of a specimen of type 1-T-1. (b) Schematic of the tow configuration associated with the stuffer misalignment around the site of the kink band.

Stress-strain hysteresis records taken from the clip gauge show that the loading and unloading elastic moduli remain nearly constant over 80-90% of the fatigue life. Only over the last 10-20% of fatigue life do softening and pronounced hysteresis develop. It is likely that the onset of softening and hysteresis is a manifestation of kink band formation (see below).

Load-life data are shown in Fig. 21 in the form load amplitude $\Delta\sigma$ vs. cycles to failure N. Data for monotonic loading (N=1) are reproduced from [37].

5.3 Modeling Fatigue Life

5.3.1 Fatigue Damage Accumulation Leading to Kinking

Here a law is sought to predict the onset of kink band formation. While the data of this program, which will be used to test the law, are for loading aligned with the stuffers, the law should work equally well for kink band formation in fillers when they are the aligned tows. It may also serve in composites with different reinforcement architectures, such as 2D weaves, braids, or even laminates.

The absence of evidence that microcracking around tows precedes kinking in fatigue suggests that Eq. (50) remains a valid criterion for kink band formation. In fatigue the criterion becomes

$$\left|\sigma_s^{(\min)}\right| = \frac{\tau_c}{|\zeta|} \tag{51}$$

where $\sigma_s^{(\min)}$ is the maximum local axial stress and ζ is the misalignment angle for any stuffer segment. Equation (51) describes an instability driven by axial shear stresses within the tow, whose magnitude under nominally aligned loads is proportional to ζ. The value of ζ does not change during fatigue, except perhaps when damage is very advanced. Neither does $\sigma_s^{(\min)}$ change significantly, at least until some other kink band forms and load redistribution affects the reference stuffer segment. Fatigue damage accumulation is therefore conjectured to consist of continuous lowering of the value taken locally by τ_c.

Physically, falling τ_c is conjectured to correspond to microcracking of the resin *within* the affected tow segment. The idea of accumulating resin damage as a fatigue mechanism was first put forward by Piggott and Lam, who reported fatigue induced resin damage in unidirectional tape laminates [41]. As yet, similar microcracking has not been observed prior to kink band formation in textile composites. It would presumably consist of submicron cracks between pairs of neighboring fibers (diameter ~7 μm; spacing ~ 1 μm); or the debonding of fiber/resin interfaces. Direct confirmation of its existence will require tedious sectioning and inspection of many specimens.

The rate of resin damage is assumed to increase with the axial shear stresses induced by misalignment. By speculation, the law of degradation of τ_c is written

$$\frac{d\tau_c}{dN} = -A(\Delta\tau_s)^m \approx A(\Delta\sigma_s\zeta)^m \tag{52}$$

where A and m are material constants; and $\Delta\sigma_s$ and $\Delta\tau_s$ are the cyclic ranges of the local axial stress and the local axial shear stress in the tow.[1] The applied load amplitude $\Delta\sigma$ may be substituted for $\Delta\sigma_s$ via

$$\Delta\sigma_s = \Delta\sigma \frac{E_s}{E_1} \quad , \tag{53}$$

where E_s and E_1 are Young's moduli for a single stuffer and the whole composite. The former is well approximated by Hashin's model [26]; the latter by isostrain volume averaging models (Section 3). The values used here are taken from Section 3. They are listed in Table 10. Variations from composite to composite are due to differences in fiber volume fractions. The relation between $\Delta\sigma_s$ for any stuffer segment and $\Delta\sigma$ is also influenced to some extent by random misalignment of neighboring stuffer segments, which makes load distribution uneven. However, this effect is small compared to the dependence of τ_s on the value of ζ for the subject segment (Section 4) and it is therefore neglected.

Equations (51)-(53) imply a relation between the applied load $\Delta\sigma$ and the cycles, N_k, to kink band failure, given ζ; i.e., the cycles required for τ_c to be reduced sufficiently for Eq. (51) to be satisfied on the next compressive loading:

$$N_k = \frac{\zeta|\Delta\sigma/(1/R-1)|E_s/E_1+\tau_o}{A[\zeta\Delta\sigma]^m} + 1 \quad , \tag{54}$$

where τ_o is the pristine value of τ_c and the load ratio $R \equiv \sigma_{min}/\sigma_{max}$. For fully unloaded compression-compression fatigue, $R = -\infty$.

[1] Whether it is appropriate to represent all stress effects by the stress range $\Delta\sigma_s$ will be assessed in more detail in Section 6.

Table 10. Young's Moduli for Composite, E_1, and Stuffers, E_s

Composite Label	E_1 (GPA)	E_s (GPA)	Composite Label	E_1 (GPA)	E_s (GPA)
1-L-1	35.7	84.2	*h*-L-1	88.6	142.3
1-L-2	34.5	88.8	*h*-T-1	87.0	142.6
1-T-1	46.3	111.1	*h*-T-2	82.4	135.9
1-T-2	43.2	97.7	*h*-O-1	93.0	147.0

5.3.2 The Fatigue Life of a Composite

Equation (54) predicts that N_k falls with increasing misalignment angle, ζ, as expected. The incidence of kink bands throughout any specimen will accordingly depend on the statistical distribution of ζ. As each successive kink band forms during fatigue, the axial stress in the affected stuffer segment will fall close to zero. The failed tow will then debond from the surrounding composite (Fig. 19a and [12,37]) over some characteristic slip length l_s from the failure site. Along the slip zone, axial load is restored from the surrounding composite to the failed tow by friction, until beyond the zone it regains its far field value. Since l_s is generally much larger than the tow diameter, the frictional load transfer is well described by the shear lag approximation. A complete description of fatigue failure requires simulating the stochastic process of kink formation, while computing redistributed loads in the entire composite sample (most simply by shear lag modeling) following each kink band event. Eventually so many stuffers will be softened by kink bands that complete failure will occur on a single cycle. A finite element formulation of this problem, the Binary Model, was described in [37] and above.

While the Binary Model can reveal details of the effects of misalignment distribution, load redistribution, stress concentrators, etc., rough estimates of fatigue life under load control can be deduced from Eq. (54) much more simply. Hysteresis observations indicate that fatigue life does not extend greatly beyond the first few kink bands. Consistently, peak load in monotonic compression is associated with the formation of two or three kink bands in specimens of the same size [12,37]. Therefore, fatigue life can be estimated by interpreting ζ in Eq. (54) as a value representative of the extremes of the distribution F_ζ. Equation. (54) becomes a law for constant load amplitude fatigue life: for $R = -\infty$

$$N_f = \frac{\zeta \Delta\sigma E_s / E_1 + \tau_o}{A[\zeta \Delta\sigma]^m} + 1 \equiv f(\Delta\sigma, \zeta, A, m). \tag{55}$$

Further remarks on the value of ζ to be used in Eq. (55) appear below.

5.3.3 Fitting the Fatigue Law to Data

The fatigue life data of Fig. 21 were first analyzed by treating the representative misalignment angle ζ for each composite as an unknown quantity to be determined by curve fitting. The fitted value for the i^{th} composite will be denoted $\zeta_{fit}^{(i)}$. It takes a different value for each material because the degree of irregularity varies from one composite to another.

To fit load-life data, values are also needed for the initial shear flow stress τ_o and the material constants A and m. For AS4/Shell 1895 composites (corresponding to the heavily compacted composites), tests on ± 45° laminates yield $\tau_o \approx 75$ MPa [12,37]. Following [12,37], the same value is assumed for AS4/Tactix 138 composites (the lightly compacted composites), since Shell 1895 and Tactix 138 have similar properties in tension and compression. Possible dependence of τ_o on fiber volume fraction is assumed weak and neglected. Since τ_o is the same for the two resins used, A and m are also assumed to be the same for all composites.

Denote the load-life data for the i^{th} composite $\{(N_{ij}, \Delta\sigma_{ij}),\ j=1,...,m_i\}$, where N_{ij} is elapsed cycles to failure; $\Delta\sigma_{ij}$ is the corresponding value of $\Delta\sigma$; and m_i is the number of data points. The load-life data were fitted by minimizing

$$S = \sum_i \left\{ \sum_j \left[f_1^{-1}\left(N_{ij}, \zeta_{fit}^{(i)}, A, m\right) - \Delta\sigma_{ij} \right]^2 \right\} \tag{56}$$

where $f_1^{-1}(N_f, \zeta, A, m)$ is the inverse of the function f defined in Eq. (55). Numerical methods for the fitting problem are outlined in the Appendix C.

The fitted load-life relations are shown in Fig. 21. The fit is satisfactory, although, of course, this does not of itself prove the correctness of Eq. (55) or the mechanics

underlying it. For large N, the load-life curve is nearly linear on the log-log plot shown, with slope ≈ -1/m. This limit is evident from Eq. (55). The fatigue exponent m is an indicator of fatigue sensitivity. It has the value m = 30 ± 4. Values and error bars for $\zeta_{fit}^{(i)}$ are shown in Fig. 22, which is described more fully in the next Section. The procedure for estimating the uncertainty in m or $\zeta_{fit}^{(i)}$ is given in Appendix C.

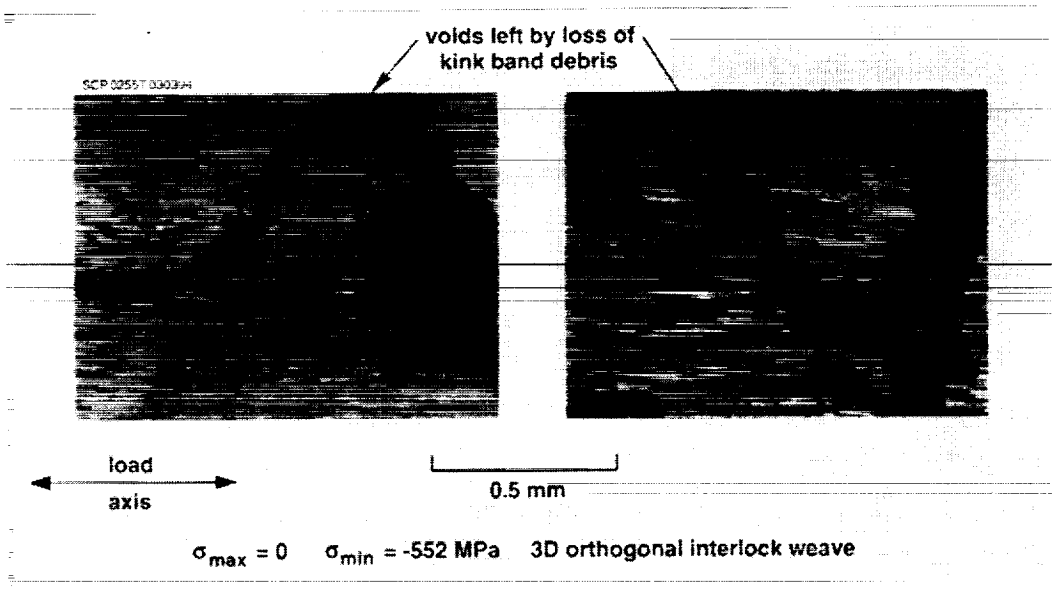

Figure 20. Kink bands found in heavily compacted composites after failure.

5.3.4 Measured Distributions of Misalignment Angles

Misalignment angles were measured for all the subject composites by methods described in Section 2. The largest misalignments are those in the out-of-plane direction. In-plane misalignments are small enough to be ignored.

Distributions of out-of-plane misalignment extrema were shown in Fig. 7. Fatigue life *under load control* in the test specimens is observed to be nearly exhausted when two or three kink bands have formed. The values of ζ for the corresponding tow segments ought to fall in the last 10% or so of the measured cpd. Thus the 0.9 quantile of the cpd, $\zeta_{0.9} \equiv F_\zeta^{-1}(0.9)$, where F_ζ^{-1} is the inverse of Fζ, should be a representative measure for substitution into the fatigue law Eq. (55) for specimens tested.

Values of $\zeta_{0.9}$ are compared in Fig. 22 with the misalignment angles, $\zeta_{fit}^{(i)}$, found for several composites by minimizing Eq. (56). The error bars shown for $\zeta_{0.9}$ arise from noise in the tow loci deduced from photographs and partly from sampling errors. Their computation has been described in [12,37].[5] Figure 22 broadly confirms the expected equality of $\zeta_{0.9}$ and $\zeta_{fit}^{(i)}$. The most significant variations in $\zeta_{0.9}$ and $\zeta_{fit}^{(i)}$ are between the groups of lightly and heavily compacted composites. The values inferred from fatigue data and the measured misalignments vary proportionately from one group to the other. However, within each group, the uncertainties in $\zeta_{0.9}$ and $\zeta_{fit}^{(i)}$ and the limits of the simple assumptions underlying Eq. (55) obscure any trends.

5.4 Discussion

5.4.1 Fitting Load Life Data

There is insufficient information in the data of Fig. 21 to test the validity of the model for fatigue life. Nevertheless, some characteristics of the predictions appear to be confirmed.

The experimental data are consistent with the prediction that the different load life curves should be parallel to one another. (i) This confirms that all fitted material properties, τ_o, A, and m are the same for all composites. Only the misalignment angle statistic, ζ, varies from curve to curve. Since ζ appears in Eq. (55) only in the product $\zeta\Delta\sigma$, changing ζ simply shifts the predicted curve along the stress axis. (ii) The product $\zeta\Delta\sigma$ is proportional to the axial shear stress in the tow segment whose misalignment is ζ. Thus the data falling on parallel curves also confirms that $d\tau_c/dN$ is a function of the axial shear stress only.

Equation (55) predicts load-life curves that are not quite straight on log-log plots, as close inspection of Fig. 21 bears out. However, the departure from linearity is less than the noise in the life data. The data would be fitted equally well by a Basquin law,

$$\log N_f = -m \log \Delta\sigma + \text{constant} \qquad (57)$$

[5] For reasons detailed in [12,37], the error in $\zeta_{0.9}$ that arises from noise in images is systematic; i.e., it amounts to an uncertainty factor in the scale of the abscissa of Fig. 22.

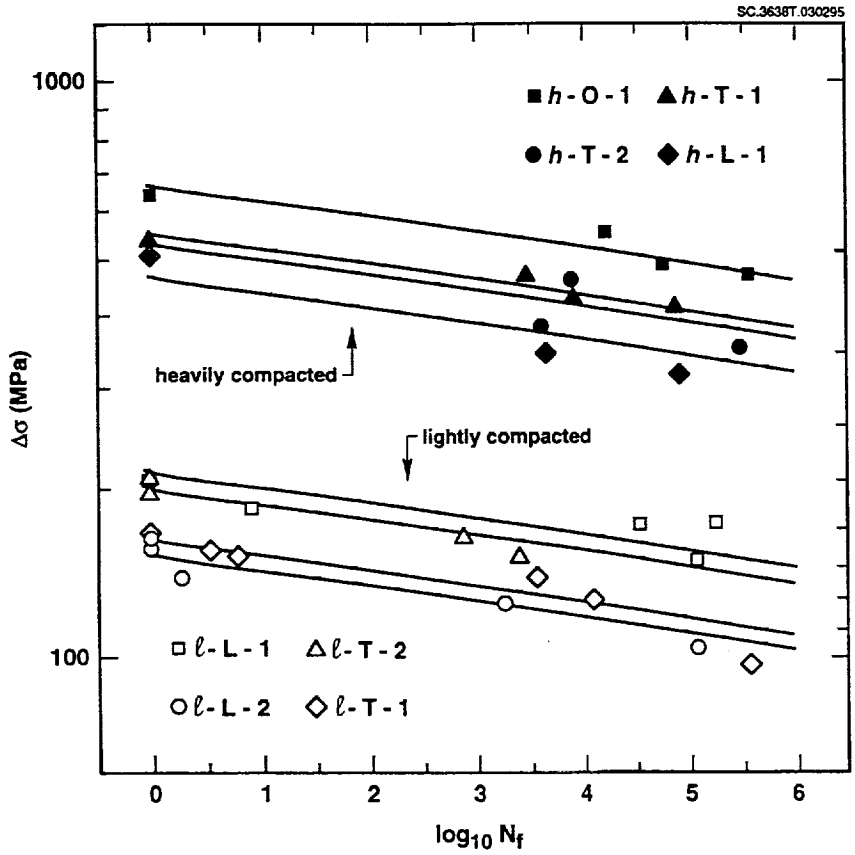

Figure 21. Load-life data and fitted curves based on estimates of the cycles to the formation of the first few kink bands.

Only the modeling steps leading to Eq. (55) argue for a nonlinear curve. Nevertheless, the near uniform slopes of the fitted curves and the data confirms the feature of the conjecture in Eq. (52) that $d\tau_o/dN$ varies as a fixed power of the axial shear stress, $\Delta\sigma\zeta$.

Given ζ, Eqs. (54) and (55) yield

$$\left|\frac{\Delta\sigma}{1/R-1}\right| = \frac{\tau_o}{\zeta}\frac{E_1}{E_s} \tag{58}$$

(where the left hand side is just $|\sigma_{min}|$) for failure on the first cycle. This prediction was compared with measurements of monotonic strength in [12,37], with a degree of

agreement similar to that of Fig. 22. In both cases, values of ζ implied by test data (strength or fatigue life) were slightly higher than those measured on specimen cross sections. However, the discrepancy is not significant given measurement errors and modeling uncertainties.

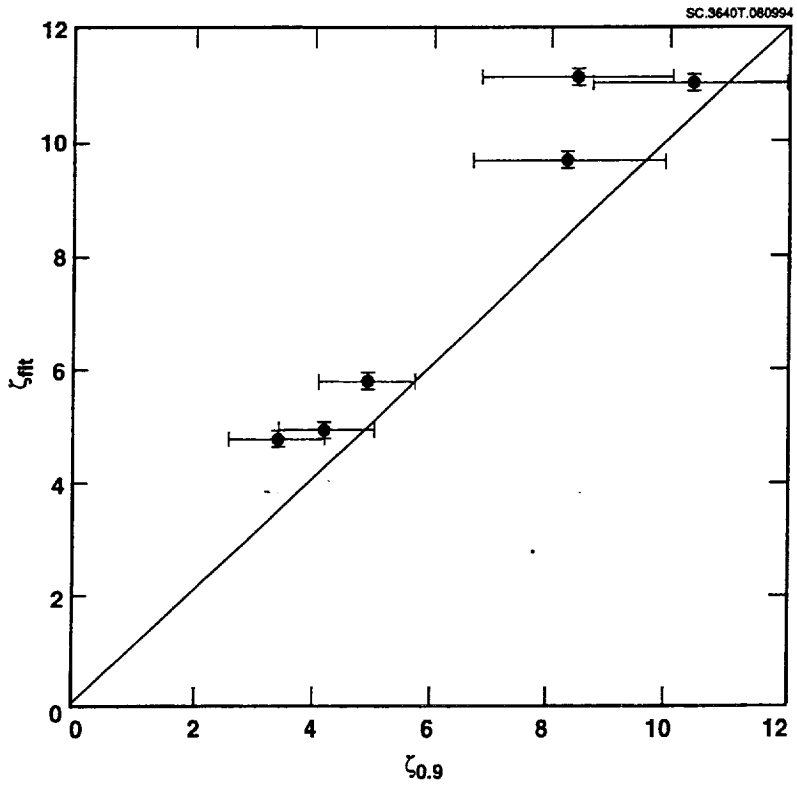

Figure 22. Measures of misalignment extrema: ζ_{fit} deduced from fitting Eq. (55) to load-life data; and $\zeta_{0.9}$, the 0.9 quantile of the measured distribution of maximum out-of-plane misalignment angles in tow segments.

5.4.2 Variations in Modulus

Young's modulus in the stuffer direction is dominated by the stuffers. Young's modulus of a single stuffer is reduced by tow waviness by a factor that depends on the continuously varying misaligned angle ξ (of which ζ measures extrema), which is

approximately normally distributed (Section 2). The reduction factor η ($\eta < 1$) is given approximately by (from Eq. (10))

$$\eta \approx \sigma_\xi \sqrt{2\pi} \left\{ \int_{-\infty}^{\infty} e^{-\xi^2/2\sigma_\xi^2} \left[1 + \left(\frac{E_s}{G_{xy}} - 2(1+\nu_{xy}) \right) \xi^2 \right] d\xi \right\}^{-1}, \tag{59}$$

where σ_ξ is the width of the distribution of ζ; while E_x, G_{xy} and ν_{xy} are the axial modulus, axial shear modulus, and axial Poisson's ratio of the stuffers in a local coordinate system in which the x-axis is aligned with the fibers. Equation (59) is essentially an average of axial stiffness along a wavy tow under conditions of uniform axial stress. The term $E_s/G_{xy} - 2(1+\nu_{xy})$ in Eq. (59) is a measure of the anisotropy of a single tow. For graphite fibers and pristine resin, it is typically ≈ 40.

Equation (59) suggests two mechanisms for softening: an increase in misalignment (i.e., in σ_ξ); or an increase in the anisotropy factor. Misalignment appeared not to change during fatigue, leaving only changes in anisotropy to consider.

Since E_x for a stuffer is dominated by the graphite fibers, any significant change in anisotropy must come from a decline in the axial shear modulus G_{xy}, which is resin dominated. This would be interpreted as another consequence of the resin damage that causes the decline in the shear flow stress, τ_c. To make some crude estimates, assume that G_{xy} declines according to a law similar to Eq. (52):

$$\frac{dG_{xy}}{dN} = -A \left(\Delta\sigma_s \xi \right)^m \tag{60}$$

with the same coefficients A and m that were determined for the shear flow stress, τ_c, but with ζ replaced by the continuously varying misalignment angle ξ. (Reductions in G_{xy} and τ_c do not necessarily go hand in hand. The former, as inferred from the loading modulus in hysteresis data, refers to strains $\lesssim$0.5%. The shear flow stress relevant to kink band formation, τ_c, refers to strains >1%.) Substitution of Eq. (60) into Eq. (59) implies a reduction in composite modulus that might accompany softening of the resin prior to kink band formation. The computed reductions turn out to be very small ($< 10^{-4}$). The integral in Eq. (59) is dominated by values of ξ that are much less than ζ, which measures extrema of ξ; but, because of the high values of the exponent m found empirically in

Section 5.3, dG_{xy}/dN is negligible unless $\xi \approx \zeta$. Thus, even at the end of life, when τ_c at a location of extrema misalignment has fallen substantially, the spatially averaged stiffness of a tow is essentially unchanged.

Only two credible sources of reduced stiffness remain: microcracking and the onset of kink band formation. From the observations reported above, kind bands cause most microcracking; and *therefore kink bands are inferred to be the source of softening late in life.*

5.5 Load Control and Strain Control

The simple relation between the result in Eq. (54) for kink formation at a single site and the fatigue life law in Eq. (55) is suggested for fatigue under load control. It is based on the prior observation that, under load controlled monotonic loading, the specimen cannot survive the formation of the first few kink bands [12,13,37]. However, the equivalence of a few kink bands and ultimate failure does not *necessarily* follow for fatigue. In fatigue, the distribution of the strengths of flaws evolves with cycles (Eq. [52]). Especially for high cycle fatigue, it may in principle become quite dissimilar to the pristine distribution, and several kink failures may no longer necessarily cause catastrophic failure. Yet the experimental evidence presented here is that they do; or at least that their occurrence accounts for 80-90% of fatigue life under load control, even for high cycle fatigue.

Under strain control, life prediction may be more difficult. The subject composites can exhibit remarkably high strain to failure for monotonic compression under displacement control, surviving high densities of kink bands in individual stuffers before ultimate failure [12,13,37]. One might consistently expect considerable life following the formation of the first kink bands under cyclic loading at constant strain amplitude. Ultimate failure will depend on the details of the redistribution of load around individual kink bands. A computational model of this process has been formulated, the Binary Model of [23,37]. The law Eq. (52) will serve as a local constitutive law within the Binary Model, with $\Delta\sigma_s$ the computed local axial stress, updated following each kink band event.

6. Tension-Compression Fatigue

Further load-controlled fatigue tests were conducted under fully reversed loading (R=-1), using the same specimen configuration used for compression-compression fatigue. Tests were limited to one weave architecture, viz. *h*-T-2.

Load-life data for the fully-reversed fatigue tests are compared in Fig. 23 with data from Fig. 21 for compression-compression fatigue. The ordinate in Fig. 23 is the magnitude of the maximum compressive stress on any cycle, $|\sigma_{min}|$. If fatigue life were governed by the cyclic load amplitude, then the data for fully-reversed fatigue ($\Delta\sigma=2|\sigma_{min}|$) should be a factor of two lower on the stress axis than the compression-compression data ($\Delta\sigma=|\sigma_{min}|$). However, they are in fact lower by only approximately 20% at the lives for which fully reversed data are available. The tensile half cycle is apparently far less injurious than the compressive half-cycle.

Because of limited resources, destructive examination of test specimens was not performed to probe fatigue mechanisms for fully-reversed loading. However, since fatigue life is correlated most strongly with the magnitude of the compressive cycle, the fatigue mechanism is very likely to be kink bands similar to those presented in Section 5. Following the conjecture of Section 5, fatigue life should be proportional to the cyclic range of the local shear stress in misaligned tow segments. Now the shearing of a misaligned tow is a nonlinear phenomenon: compressive loading exacerbates misalignment, allowing greater shear strain; while tensile loading straightens fibers, which minimizes shear strains. This nonlinearity was not incorporated in Eq. (52), which includes the linear approximation $\Delta\sigma\zeta$ for the cyclic range of the local shear stresses. If Eq. (52) was corrected to account for nonlinearity, the relative weight of tensile loads as a cause of fatigue damage accumulation would be reduced. A physically consistent model of fatigue for both compression-compression and tension-compression loading might result. Much more data is required to conclude this question.

The evolution of stress-strain hysteresis during one of the fully-reversed tests is shown in Fig. 24. Late in life, softening is evident in both the compressive and tensile load cycles. As for compression-compression tests (Section 5), the softening is most likely a manifestation of kink band events. Kink bands cause local softening in both tension and compression. No other damage observed on the specimens seems capable of causing such large changes in tangent stiffness.

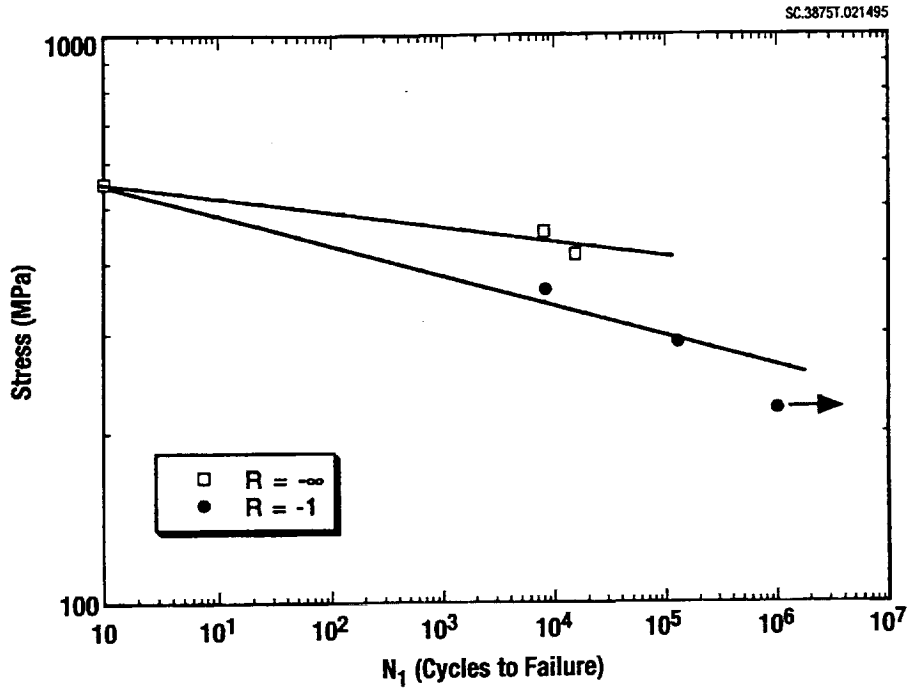

Figure 23. Comparison of fatigue data for composite *h*-T-2 under fully-reversed and compression-compression loading.

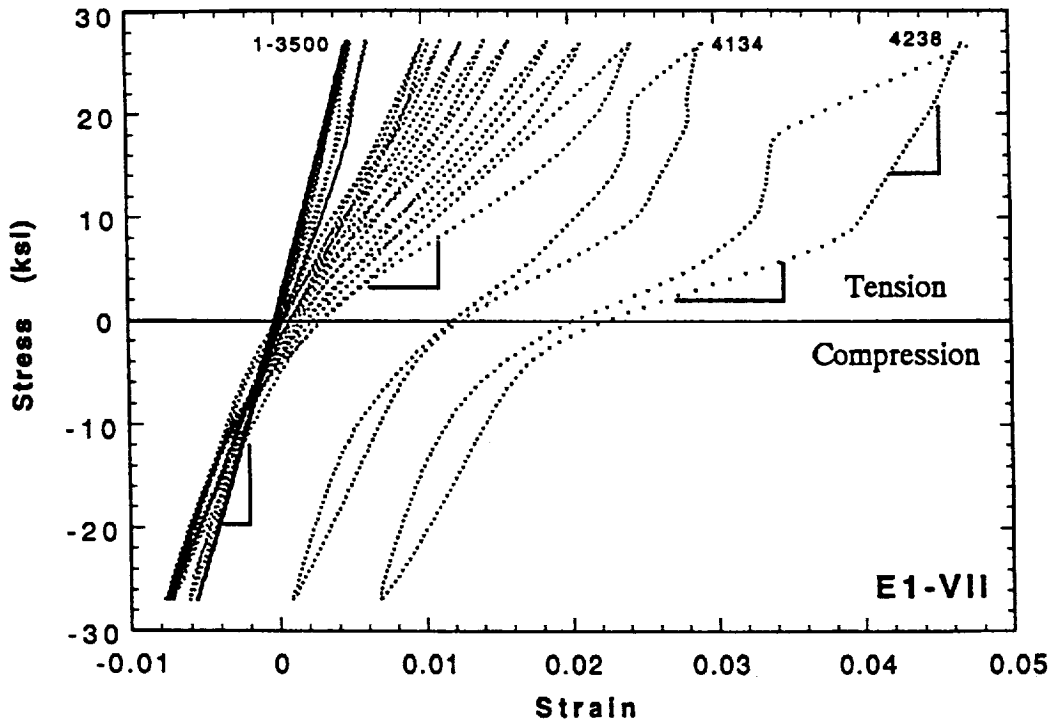

Figure 24. The evolution of hysteresis in composite *l*-O during fully-reversed cyclic loading.

7. Work of Fracture and Notch Sensitivity

Tensile tests of most 3D woven composites in our material matrix were reported in a prior contract [12,37]. Those tests showed exceptional strains to peak load and high implied work of fracture. However, quantitative analysis was restricted by unexpected inadequacy in the method of strain measurement. Damage was so broadly distributed along the gauge section ($\approx$ 25 mm) that, in many cases, it fell outside the 10 mm clip gauge used to measure axial strains. Some test data for cases where considerable damage happened to fall within the gauge are shown in Fig. 25(a)-(c). However, even in these tests it was unclear whether all nonlinearity had been measured; and important details of the mechanisms of failure and damage distribution remained undetermined. Additional studies were therefore undertaken.

7.1 Tensile Tests - Preliminary Observations

The additional tensile tests were performed for several heavily compacted composites, again with the dog-bone specimens of Fig. 18 loaded along the stuffer direction. The grips were placed a few millimeters away from the gauge section, allowing room to attach extensometer rods that measured the displacement, d, over the entire gauge section plus a millimeter or so at either end. This displacement was used as the control variable for loading. The relative displacement of the grip mountings was also recorded for qualitative confirmation of the extensometer data.

The extensometer displacement also yields an estimate, $\varepsilon_o = d/l$, of the engineering strain in the gauge section, with l the initial separation of the extensometer rods. The estimate is a lower bound to the actual strain because the shoulders of the specimen are included in the gauge length, l; but analysis shows that the difference is inconsequential in what follows.

Fig. 25(d)-(f) presents stress-strain histories for the new, long gauge length tests. With some variation from material to material, key characteristics are consistent. Substantial nonlinearity sets in at strains between 0.5% and 1%, usually in the form of continuous softening. At high loads, the smooth curve gives way to a series of jagged peaks and sharp, small load drops. The global peak load is 0.7-1 GPa. This is approximately 70% of the value that would be expected from the strengths of pristine

AS4 graphite fibers and the volume fraction of aligned fibers [12,37]. At a critical strain that varies from 2.3% to nearly 4%, an unstable, large load drop occurs, which will be called the primary load drop. Smaller but significant loads then persist to very large displacements, often similar to the initial gauge length. Similar long tails to the stress-strain histories would presumably have been recorded in Figs. 25(a)-(c) had the tests not been terminated at the primary load drop by operator decision.

The primary load drop common to all tests conveniently divides the material's response into two phases. The phase prior to the primary load drop will be called the "hardening phase," since the stress is generally increasing - the small load drops often seen near peak load will also be termed part of the hardening phase. The phase after the primary load drop will be called the "pullout phase."

As previously reported, stuffers generally rupture as discrete entities. The rupture of one stuffer does not generally cause failure of its neighbors at the same location. Instead, matrix cracking around the circumference of the failed tow debonds it from the surrounding composite, so that any stress concentration is minimized and neighboring aligned tows commonly remain intact. Sliding along circumferential debond cracks typically extends several mm from the location of the rupture. By this mechanism, stuffer failures develop over a broad damage band, often spanning the entire gauge section. The long tail in the load displacement curve corresponds to pullout of failed stuffers. The appearance of the pullout is typified by Fig. 26.

At strains of approximately 1% and generally well before stuffer failures, matrix cracks begin to appear between fillers, which were the orthogonally disposed tows in the tensile tests. These cracks become widespread after loading to high strains in all the heavily compacted composites studied. The layers of resin between fillers are clearly much weaker than the fillers themselves, since the fillers are rarely seen to fail internally. The interfiller cracks are analogous to the multiple cracks found in the 90° plies of 0/90° laminates, except that their spacing is dictated by the filler size rather than the mechanics of stress relief. Since graphite/epoxy tows are highly anisotropic and the fillers are loaded transversely in the tensile tests, the concomitant fractional change in the composite modulus is rather slight: $\leq 5\%$ (Section 3). Interfiller cracking does not contribute significantly to the substantial nonlinearity visible in Fig. 25 prior to peak load.

As the number of ruptured stuffers increases, interfiller cracks on one or more planes develop large openings, until, *beyond the primary load drop*, a macroscopic "tension crack" is evident. Such tension cracks may traverse the whole specimen, but since stuffer failures are not generally coplanar, they remain bridged by intact stuffers. Ultimate failure eventuates when the bridging stuffers are pulled out of the fracture surfaces.

Tension cracks do not always cross the whole specimen. When viewed on a cut side of the specimen, they are occasionally seen to terminate at a delamination crack running parallel to the load axis between a layer of stuffers and a layer of fillers. Ultimate failure may then consist of separation of the specimen along a path comprising the first tension crack, the delamination crack, and a second tension crack traversing the rest of the specimen. The two tension cracks may be offset from one another by as much as 10 mm.

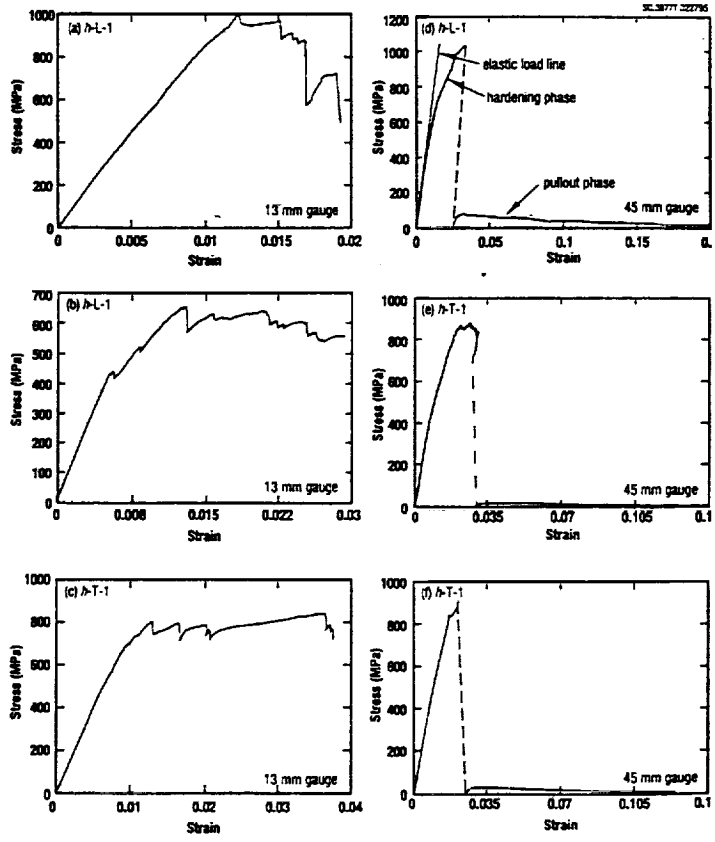

Figure 25. Stress-strain curves for tension tests of heavily compacted composites. The gauge length over which the displacement was monitored is as marked.

7.2 The Maximum Strain in the Hardening Phase

Fig. 27 is a summary of the range of strains to failure measured for AS4 fibers formed into unidirectional composites with different thermoset and thermoplastic matrices.[1] The failure strains are distributed around a median of approximately 1.5%. Nearly all values fall below the strain to failure of bare fibers, 1.65%, quoted by the fiber manufacturer.[2] The composite failure strains are slightly lower because the matrix concentrates stress around the first fibers to fail, leading more readily to failure of their neighbors.

The volume fractions of the composites represented in Fig. 27 are similar in many cases to those found in the interior of stuffers in the heavily compacted 3D weaves. One might therefore infer that the strains to failure of the stuffers, and therefore of the 3D woven composites themselves, ought to be similar. In fact, the hardening phase in the composite, over which loads are typically $\approx$ 1 GPa, survives to considerably greater strains than this: in the range 2.5-4%.

The extent of nonlinearity prior to peak load can be highlighted by comparing the measured stress-strain data curves with the linear projection of the initial elastic response (e.g. Fig. 25d). Stress-strain data for unidirectional materials follow linearity to peak load quite closely. Data for 0/90° laminates show some softening due to 90° ply cracking, but only of the order of a few percent, since the 0° plies dominate stiffness. Distinct mechanisms clearly operate in the 3D woven composites.

7.3 Damage Mechanisms in the Hardening Phase

Considerable energy was applied to explaining how the strain at peak load in the woven composites can be so much greater than in unidirectional composites. The answer lies partly in the effects of geometrical irregularity, especially stuffer waviness, crimp, and twist; and partly in the mechanics of load redistribution around sites of stuffer failure.

For loading along the stuffer direction, x_1, the response of the composite is dominated by the stuffers themselves. The fillers, which are orthogonal to the load, and the warp weavers, which follow oscillating paths mostly at large angles to x_1, are

[1] From data compiled by Dr. Norm Johnston and Mr. C.C. Poe, NASA Langley Research Center
[2] Data sheets, Hercules, Inc., Salt Lake City, Utah.

relatively compliant for loads along this axis. In the elastic regime, Young's modulus in the stuffer direction, E_1, is fairly well approximated by

$$E_1 \approx f_s E_x^{(UD)} + (1-f_s) E_y^{(UD)} \tag{61}$$

where f_s is the fraction of all fibers that lie in stuffers; and $E_x^{(UD)}$ and $E_y^{(UD)}$ are the axial and transverse Young's moduli for an individual tow considered as a unidirectional composite. For the heavily compacted composites, $f_s \approx 0.58$ (Table 2), $E_x^{(UD)} \approx 140$ GPa, and $E_y^{(UD)} \approx 8$ GPa (Table B.2). The fraction of the total external load borne by the stuffers is $f_s E_x^{(UD)}/E_1 \approx 0.96$.

Plastic Tow Straightening

All of the stress-strain curves show significant nonlinearity setting in when the applied load $\sigma_a \approx 500$ MPa, corresponding to strain $\varepsilon_o \approx 0.6\%$. It is very unlikely that any stuffers have ruptured at so low a strain. Interfiller cracks begin at this strain level, but they can lower Young's modulus only by about 4%, since they do not affect the modulus of stuffers. Between strains of 0.6% and 1% (at which strain stuffers have not yet begun to fail), the data of Fig. 25 show much larger declines in the tangent modulus.

This softening is believed to arise from plastic straightening of the stuffers, i.e., the reduction under load of the degree of their random waviness. If the straightening were an elastic process, Young's modulus should rise with strain, since a one-dimensional composite is stiffer when it is better aligned. However, if the straightening is plastic, then initially misaligned tow segments can elongate at approximately constant local axial loads; and the composite will appear macroscopically to soften.

The critical applied load for the onset of plastic straightening can be estimated from other data. The initial misalignment angle, ξ, of stuffer segments is approximately normally distributed (Section 2), with expectation value $<|\xi|> \approx 2°$ (Table 3) and the 90th percentile of $|\xi|$ lying near 5° (Fig. 22). The shear stress in any stuffer segment is given approximately by†

$$|\tau_{13}| \approx \sigma_1^{(s)}|\xi| \approx \sigma_a|\xi|/f_s \tag{62}$$

† Since stuffer waviness is primarily out-of-plane, the axial shear stress component τ_{13} has the largest magnitude.

where x_3 is the through-thickness direction, σ_a is the applied stress, and $\sigma_1^{(s)}$ is the axial stress in any stuffer. The critical shear stress, τ_c, for shear "flow"[2] inside a tow was independently measured in studies of kink band formation during compression (Section 5; [12]). Its value is approximately 75 MPa. Thus from Eq. (62), tow segments whose misalignment ranges from 2° to 5° should straighten plastically for applied stresses ranging from 500 to 1250 MPa. This is indeed the range over which softening is seen. The lower end of this range is also equal in magnitude to the compressive strength [12], which is determined by the occurrence of the first few kink bands. Kink bands are mediated by the same shear flow within tows.

Transition to Stuffer Rupture

The axial strain required to eliminate waviness from a tow is just c_w-1, where c_w is the crimp factor, defined as the total initial arc length per unit length along the tow's nominal axis. For a tow whose continuously varying misalignment angle ξ is normally distributed with second moment σ_ξ^2 (Eq. (5)),

$$c_w = \frac{1}{\sigma_\xi \sqrt{2\pi}} \int_{-\infty}^{\infty} \frac{e^{-\xi^2/2\sigma_\xi^2}}{\cos\xi} d\xi \tag{63a}$$

$$\approx 1 + \frac{1}{2}\sigma_\xi^2 \qquad \text{(small } \sigma_\xi\text{)} \qquad . \tag{63b}$$

Measured values of σ_ξ were listed in Table 3. The corresponding values of c_w lie in the range 1.00003-1.0012. Thus the maximum contribution to composite strain from plastic straightening of out-of-plane waviness is ~ 0.1%, which is a small part of the difference between the failure strain of the carbon fibers (1.5%) and the end of the hardening phase (2.5-4%).

However, both measurements of Young's modulus for the composite and more detailed examination of tow irregularity suggest that other significant distortions in stuffers need to be accounted for in estimates of tow straightening. Unfortunately, the additional distortions are not easy to describe, let alone to quantify - their magnitudes

[2] See [12] and [37] for a description of the microscopic nature of shear flow in these composites.

were left undetermined in Section 3. However, they can be inferred indirectly from measurements of Young's modulus. Assume that unmeasured distortions may continue to be described by a normal distribution of misalignment angles ξ, but now with an enhanced value of the variance σ_ξ^2. According to the Orientation Averaging Model of Section 3 (which concurs with the Binary Model of Section 4; see Fig. 12b), Young's modulus should be reduced by waviness by the factor

$$\eta \approx \left(1 + \sigma_\xi^2 \Gamma\right)^{-1} \tag{64}$$

where Γ is an orthotropy factor of value ≈ 40 for graphite/epoxy. The value of σ_ξ^2 can thus be deduced from the ratio of the measured Young's modulus to that predicted by the Orientation Averaging Model for a geometrically ideal composite. Thence ensues a new estimate of the crimp factor c_w via Eq. 63(b). The results of this procedure are shown in Table 11. The inferred values of σ_ξ are generally somewhat larger than those attributed to out-of-plane stuffer waviness alone (cp. σ_ξ of Table 3 with σ_ξ of Table 11). Since $c_w \propto \sigma_\xi^2$, the implied increase in c_w is greater; and the strains implied from tow straightening might be as high as 0.25%.

Table 11. Estimating the Crimp Factor for Stuffers from Measured and Predicted Young's Moduli

	E_1 (GPa)		η	σ_ξ[c]	c_w[d]
	expt[a]	OA[b]	(expt/OA)	(radians/degrees)	
h-L-1	85	91.5	0.929	0.044/2.5	1.0010
h-L-2	80	81.2	0.985	0.019/1.1	1.0002
h-T-1	79	88.6	0.892	0.055/3.2	1.0015
h-T-2	72	85.1	0.846	0.067/3.9	1.0023
h-O-1	88	93.1	0.945	0.038/2.2	1.0007
h-O-2	69	83.8	0.823	0.073/4.2	1.0027

[a] measured in the stuffer direction

[b] predicted by the Orientation Averaging Model for ideal geometry (straight stuffers)

[c] deduced from η via Eq. (64)

[d] from σ_ξ via Eq. (63b)

When this strain is added to the strain to failure for an initially straight tow, an estimate of the composite strain at which stuffers should fail results. Using the unidirectional composite data of Fig. 26 as a guide to the failure strain of a straight tow, say 1.65%, stuffers should fail at composite strains just short of 2%. Of course, the estimates of strains arising from tow straightening were based on the assumption that all tows are wavy to the same degree. In fact, there is considerable variance in the degree of waviness from composite to composite, from specimen to specimen, and from tow to tow within the same specimen. Furthermore, 1.65% is an upper bound to the failure strain of an initially straight tow. Damage during weaving is likely to reduce the strength and therefore the failure strain of at least some tows in a typical specimen gauge section. The knockdown in strength might be as much as 30% for some tows (see further remarks below). Overall it is realistic to expect that stuffers might fail at applied strains ranging from as little as 1% to perhaps 2.25%.

The stress-strain data of Fig. 25 indeed exhibit small, sharp load drops in the hardening phase once the strain exceeds a threshold that varies from 1% to 2%. These are believed to correspond to tow rupture events. Their commencement signals the attainment or near attainment of peak load.

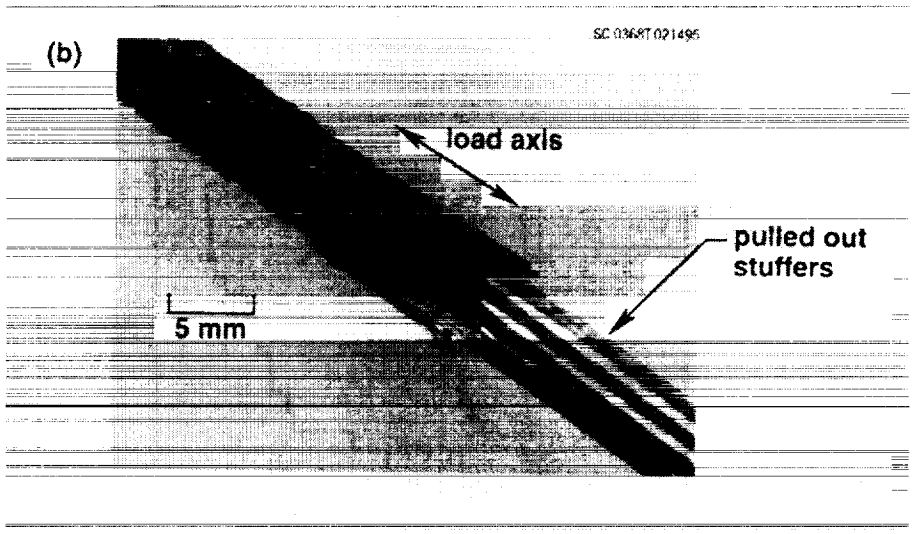

Figure 26. One half of a specimen after failure, showing evidence of extensive tow pullout.

Lockup

In most cases, the load remains very near its peak value until the primary load drop occurs at strains of 2.5-4%, well above the highest estimates for tow rupture strains. Thus some mechanism exists for transferring loads around sites of stuffer failure that are approximately equal to the load in the tow at the time it failed. This is a remarkable conclusion. It indicates an efficiency of load transfer quite beyond the realm of unidirectional composites of cross-plied laminates of any fibers in any kind of matrix.

The load transfer mechanism is believed to achieve its efficacy via a lockup mechanism involving tow waviness. Crimp features are found damaged but not entirely straightened on pulled-out tows following tensile failure, implying that they have been dragged through the composite during pullout in their crimped condition. Lockup occurs during the pullout process when crimp asperities on adjacent tows come into contact. The contact forces in 3D woven composites can be especially high because the warp weavers prevent contacting stuffers from separating to facilitate sliding.

Further remarks comparing lockup with frictional effects on smoother reinforcement appear below.

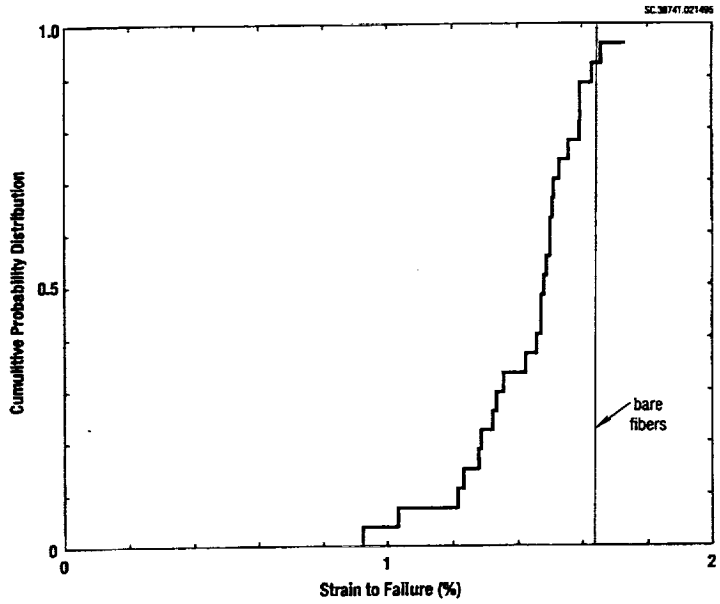

Figure 27. The distribution of strains to failure of unidirectional composites of AS4 carbon fibers in various thermoset and thermoplastic matrices. The failure of unidirectional composites is generally catastrophic: there is negligible load bearing capacity following attainment of peak load.

7.4 Flaws and Strength

The greatest unnotched strength that could ever be achieved in the composite would be that for ideally straight, undamaged stuffers. Ignoring the contributions of fillers and warp weavers (see below), one has by the rule of mixtures

$$\sigma_u \approx f_s V \varepsilon_f^{(c)} E_f \tag{65}$$

where $f_s V$ is the volume fraction of the composite constituted by the fibers in stuffers alone; $\varepsilon_f^{(c)}$ is the fiber failure strain; and E_f is the fiber modulus. For a failure strain of 1.5% for AS4 fibers in stuffers (the median of the data of Fig. 26), $f_s V = 0.35$ (an average for all the heavily compacted composites in Table 2), and $E_f = 235$ GPa (Table 5), Eq. (64) gives $\sigma_u \approx 1.2$ GPa. The measured peak loads (Fig. 25) are lower than this by 20-40%.

As previously conjectured [12], factors contributing to strength loss include damage to fibers during the weaving process; reduction of strength where stuffers are severely distorted in the composite; and the uneven distribution of loads due to random stuffer waviness. The first two of these are difficult to estimate a priori. The third, however, is amenable to modeling: this was one subject of the Binary Model calculations of Section 4. Intuitively, one sees that if one tow segment is relatively straight compared to its neighbors, then it is also relatively stiff and bears a disproportionate share of the external load. Thus the critical external load for tow failure falls as the degree of tow waviness increases. Figure 15b showed how the loads in the most highly stressed stuffer segments rise as the square of the deviance σ_ξ of the misalignment angles ξ, which represents tow waviness. Strength falls inversely with σ_ξ^2, following the reciprocal of the ordinate in Fig. 15b.

For the largest values of σ_ξ inferred by comparing measured and predicted Young's moduli (Table 11), the strength reduction due to unequal load distributions is ≈ 10%. This is about a quarter to a half of the reduction in measured peak stress from the value implied by fiber volume fractions and the strength of pristine AS4 fibers [12,37]. Thus it appears that uneven load distribution can be a significant determinant of strength, with effect in some of the tested composites comparable to the distribution of intrinsic flaws in stuffers. This conclusion gains further support from the observation that broken,

C-2

relatively straight segments of stuffers and unbroken, relatively wavy segments are often found side by side, the more wavy stuffer having ruptured elsewhere.

7.5 The Pullout Phase

Beyond the primary load drop, the stress falls monotonically and approximately linearly with displacement (Figs. 25(d)-25(f)). This is consistent with load transfer by uniform friction among stuffers whose contact length is decreasing in proportion to the separation of the two halves of a ruptured specimen. The friction stress, τ, which acts along the debonded length, l_s, of a broken stuffer (Fig. 28), can be related to the applied load, σ_a, by the shear lag approximation:

$$\sigma_a \approx f_s \sigma_s \approx f_s \frac{s\tau l_s}{A} \tag{66}$$

where s and A are the circumference and cross-sectional area of a stuffer. With $s \approx 5.4$ mm, $A \approx 1.5$ mm^2 (Table 8), $f_s \approx 0.58$ (Table 2), an average pullout length $l_s \approx 5$ mm, and $\sigma_a = 50\text{-}100$ MPa (Figs. 25(d)-25(f)), Eq. (65) yields $\tau = 5\text{-}10$ MPa.

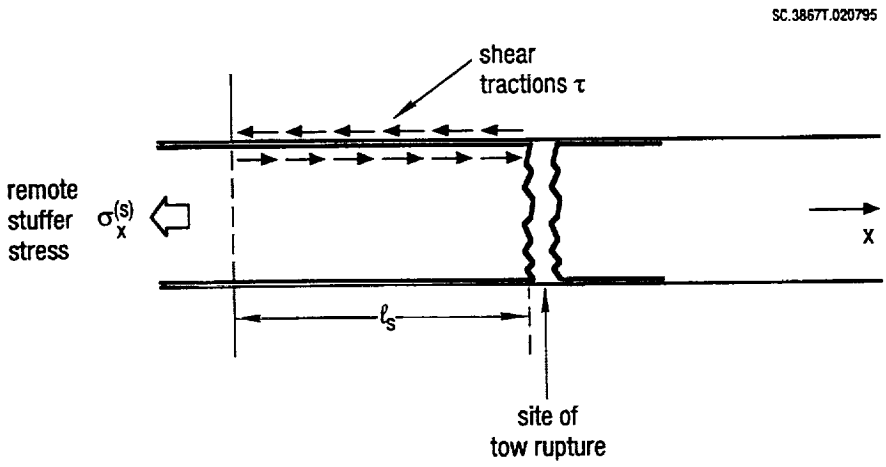

Figure 28. Cell model of frictional load transfer in the shear lag approximation.

7.6 Friction Stresses During Lockup

Stuffer rupture is always accompanied by debonding of the ruptured tow from the surrounding composite at the moment of rupture. Therefore, load transfer around failed

stuffers in the hardening phase might also be described as a frictional process. However, the frictional stresses must be very large. The macroscopic stress remains quite near peak load throughout the hardening phase, typically 700 MPa - 1 GPa. Taking l_s = 1-5 mm as representative slip lengths, Eq. (66) yields $\tau \approx$ 100-500 MPa. This range is one to two orders of magnitude greater than during the pullout phase. The friction process is clearly controlled by different mechanisms.

The critical mechanism is conjectured to be lockup: the arrest of sliding by the contact of asperities. Fig. 25 implies that the asperity contact persists from applied strains near 2% until the primary load drop (strain 2.5-4%). The primary load drop apparently corresponds to failed stuffers breaking through the restraints of asperity contact.

7.7 The Role of Warp Weavers

Warp weavers, which follow approximately sawtooth paths, fail at significantly higher applied strains than the stuffers, which are nominally straight. However, since the warp weavers contain 5-10 times fewer fibers than the stuffers (Table 2), they contribute only a few percent to Young's modulus and ultimate strength in the stuffer direction (Section 3). They are therefore unlikely to contribute significantly in a direct way to the nonlinearity prior to peak load. During the hardening phase, the load is borne predominantly by the stuffers.

The indirect effects of warp weavers, on the other hand, are profound. Their presence is the primary reason stuffers are disturbed during weaving (section 2); resulting in stuffer crimp or waviness. Without the geometrical distortion of stuffers, neither plastic tow straightening nor lockup would exist.

Equally importantly, warp weavers play a primary role in the mechanics of lockup. Under axial tension in the stuffer direction, warp weavers develop through-thickness compression. This aids lockup by increasing the contact forces between asperities. Indeed, the rupture of warp weavers has not been observed in any specimen prior to the primary load drop; while none or very few survive across the tension crack observed in the pullout phase. *Therefore, we conjecture that the primary load drop occurs exactly when warp weavers fail and permit already ruptured stuffers to spring apart and move relatively freely pass another.*

7.8 Bridging Tractions and the Work of Fracture

In a large specimen containing a stress concentrator such as a hole, tow rupture would be expected to develop as a band of damage that could be described macroscopically as a crack (Fig. 29). The nonlinear process of tow straightening, rupture, lockup, and pullout would form a cohesive zone behind the crack tip, defined here as the point of furthest advance of damage. At sufficiently large crack lengths, traction free fracture surfaces will develop in the far crack wake (Fig. 29).

The fracture mechanics of such a crack are determined by the relation between the tractions, p, across the cohesive zone and the displacement discontinuity or crack displacement, 2u, that it introduces into the body. It will be seen below that the cohesive zone in 3D woven composites is very long; at least an order of magnitude greater than the specimen width in the tensile tests. Consistently, damage is essentially uniform in the tensile tests, apart from statistical fluctuations deriving from random tow waviness. Therefore the tensile test yields a direct measurement of the relation p(u). The bridging tractions, p, can be identified with the applied load, σ_a. The displacement discontinuity, 2u, is related to the displacement, d, measured over the gauge length, l, by

$$2u = d - \frac{\sigma_a}{E_c} l \tag{67}$$

where E_c is the composite modulus and the second term represents the displacement that would have been measured in the absence of any nonlinearity.

Bridging traction laws p(u) deduced in this way from the data of Fig. 25(d)-(f) are shown in Fig. 30. In the cases where the extensometer gauge length was only 13 mm, damage that developed outside the measurement interval prevents meaningful inferences.

The work of fracture, W_f, is related to p(u) by [42,43]

$$W_f = 2\int_0^{u_c} p(u)du \quad , \tag{68}$$

where u_c is the critical opening displacement at which p vanishes. This is just the area under the curves of Fig. 30. Values for W_f for each of the cases in Fig. 30 are listed in Table 12.

The work of fracture of the 3D woven composites is very large - approximately an order of magnitude greater than that of unidirectional or cross-plied graphite/epoxy laminates. Indeed, the values of Table 12 appear to exceed those for any other class of materials (Fig. 31; [44]).

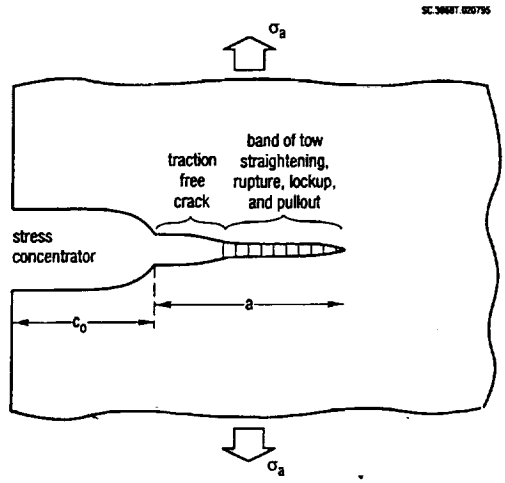

Figure 29. Conjectured appearance of tow failure near a stress concentrator as a propagating band of damage.

Table 12 also shows a breakdown of W_f into contributions $W_f^{(1)}$ from the hardening phase and $W_f^{(2)}$ from the pullout phase: $W_f^{(1)}$ is by far the larger. the contributions to $W_f^{(1)}$ from plastic tow straightening and from tow rupture and lockup can also be crudely separated. Assume that tow straightening finishes and tow rupture begins when the applied strain is 2%. Over the gauge length d the corresponding value $2u_s$ of 2u is given by

$$2u_s + \frac{\sigma_a}{E_c} d = 0.02 \qquad (69)$$

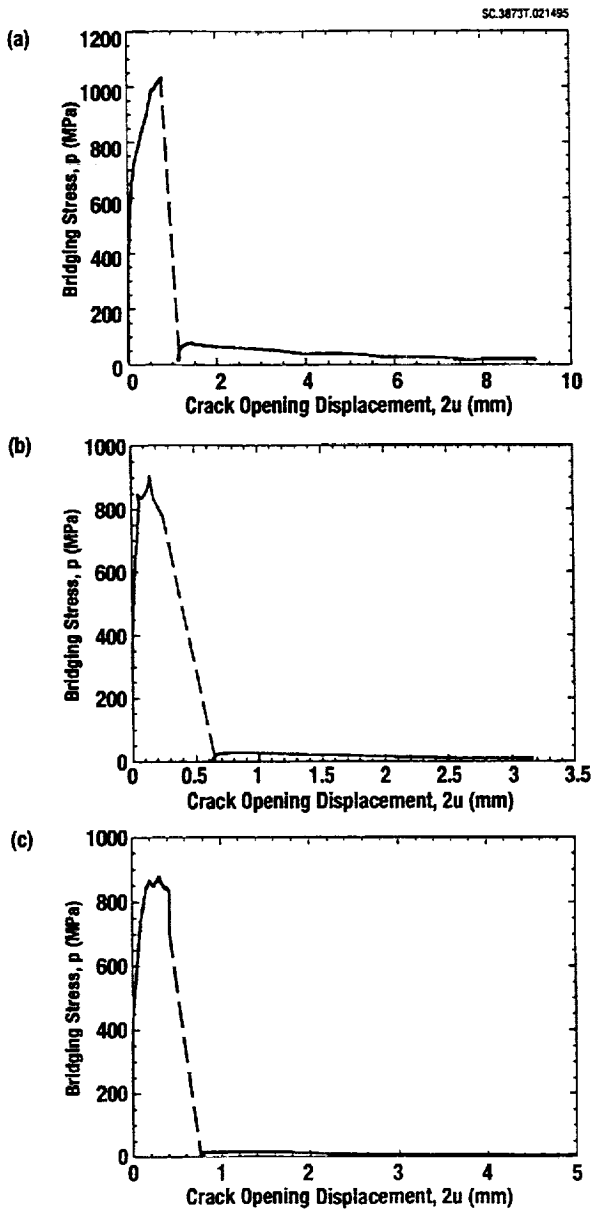

Figure 30. The measured relation between the bridging traction, p, and the displacement discontinuity, 2u.

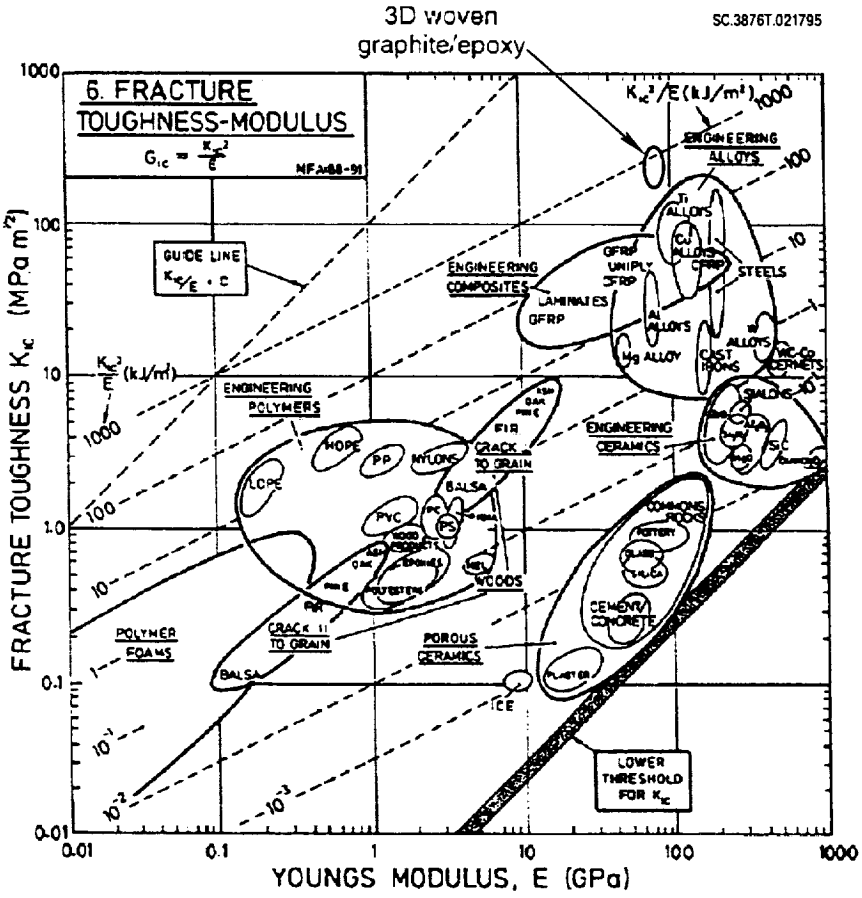

Figure 31. The work of fracture of 3D woven composites compared to ranges of values compiled for all other classes of structural materials (from [44] by kind permission of the author).

The contribution of tow straightening to $W_f^{(1)}$ is given roughly by the value of the integral Eq. (66) when $u_c = u_s$, with the remainder of $W_f^{(1)}$ being the contribution from tow rupture and lockup. The contribution from tow rupture can be estimated as $f_s W_f^{(UD)}$, where f_s is the area fraction of the stuffers and $W_f^{(UD)}$ is the work of fracture of a unidirectional carbon/epoxy composite. From Table 2, $f_s \approx 0.6$; while $W_f^{(UD)} \sim 100$ kJ/m^2. These crude estimates of the three separate contributions to $W_f^{(1)}$ are listed in Table 12. The

contribution from lockup, i.e., the effects of sliding and friction enhanced by asperity contact prior to the primary load drop, is generally the greatest but also probably the most variable.

7.9 Tow Waviness Effects in the Pullout-Phase

Further corroboration of the concept of lockup (or friction greatly enhanced by tow irregularity) is found from data in the pullout phase. Close inspection of Fig. 30(a) reveals an interesting feature of the pullout phase: the slope of $d\sigma_a/du$ possesses a succession of extrema at values of crack opening displacement 2u separated by approximately 2 mm. This implies a roughly periodic variation of the friction stress, which could be an effect of tow waviness. Indeed, stuffer distortions are often commensurate with the separation of fillers, which might be expected as a result of the weaving process. The filler separation is approximately 2 mm for the architecture *h*-L-1 of Fig. 25(d) (Table 8).

7.10 Notch Sensitivity

Notch sensitivity when damage propagates in a band defined by the constitutive law p(u) is most generally expressed in terms of the characteristic length, l_{ch}, of the nonlinear cohesive zone [45-9]. To order of magnitude

$$l_{ch} \sim \frac{E_c W_f}{p_{max}^2} \quad , \tag{70}$$

where p_{max} is the maximum value of p(u), i.e., the unnotched material strength. If any smooth stress concentrator is much larger than l_{ch}, then the strength, σ_c, of the part will be reduced from p_{max} by the stress concentration factor computed for an elastic body, e.g., 1/3 for a circular hole. If the length a_o of a sharp notch is much greater than l_{ch}, then

$$\sigma_c \propto \sqrt{\frac{W_f E_c}{a_o}} \quad ; \tag{71}$$

i.e., strength falls indefinitly as $a_o^{1/2}$. On the other hand, if any stress concentrator or sharp notch is much smaller than l_{ch}, then the strength loss is minimal; the reduction of σ_c from p_{max} is not far from that implied by net section considerations. Thus l_{ch} characterizes the transition from notch sensitivity to notch insensitivity.

Values of l_{ch} deduced from the laws p(u) of Fig. 30 are listed in Table 12. Commensurate with their high work of fracture, 3D woven composites are exceptionally notch insensitive, with $l_{ch} \approx 40$ -100 mm. Values of l_{ch} for unidirectional or cross-plied graphite/epoxy composites or for tough alloys are typically just a few mm.

Table 12 . Contributions to the Work of Fracture

			Hardening Phase			Pullout Phase		
Composite Label	Work of Fracture W_f (kJ/m^2)	$W_f^{(1)}$ (kJ/m^2)	Plastic Tow Straightening	Tow Rupture	Lockup	$W_f^{(2)}$ (kJ/m^2)	Pmax (MPa)	Cohesive Zone Length l_{ch} (mm)
h-L-1	1140	830	~70	~60	~700	310	1000	100
h-T-1	395	350	~70	~60	~220	45	900	40
h-T-1	500	460	~70	~60	~330	40	900	50

8. Summary of Results for Textile Modeling

In the course of this research, we have developed guidelines for modeling textiles in general, including 2D and 3D braids and weaves and stitched/woven or stitched/knitted materials. We have consistently sought the simplest model for predicting any given property that is physically correct and has the fewest unknown parameters. Specifying the degree of modeling sophistication necessary in different applications is one of our primary accomplishments.

8.1 Elastic Regime

Flat or curved panels

The macroscopic elastic constants of flat or curved panels can be predicted by the simplest of all models, viz. orientation averaging calculations based on isostrain or isostress conditions. Here, "macroscopic" signifies gauge lengths at least several times any scale of the underlying fabric architecture. For most current textile composites, this means $\gtrsim$ 10 mm. We have delivered a computer code (Appendix D) in this program which applies orientation averaging to the geometry of 3D interlock weaves. The code includes an input parameter for waviness in nominally straight tows. Simple, analytic estimates are provided for the extent to which waviness knocks down tow stiffness (following Eqs. (10)-(12)) and the concomitant effects on composite elastic constants.

Analyzing Structures

Many vital potential applications of textiles involve geometrically complex structural parts, e.g. woven or braided beams, ribs, and window belts; and integrally woven or stitched skin/stiffener assemblies. To design such internally complex structures and predict their reliability, the arrangement of tows must be modeled explicitly. When triaxial stress states exist, the isostrain or isostress assumptions of orientation averaging are likely to fail. At the same time, a very efficient formulation is necessary to deal with significant volumes of material, i.e., one with the fewest degrees of freedom permitted by the physics of the problem. Our Binary Model was designed for such applications.

Calibration tests using flat panels of 3D weaves indicate that for calculations in the elastic regime, stiffness parameters in the Binary Model can be specified a priori in

terms of fiber and resin properties (Chap. 4). The Binary Model is now being adapted to model 3D braided engine mounting structures in ARPA's Affordable Composite Technology program[1]; to model stitched structures in aircraft wings; and to model brittle fracture and creep rupture in ceramic and intermetallic matrix composites.[2]

Effects of Irregular Geometry

Tows in textile composites are inevitably irregular. The Binary Model allows Monte Carlo simulations of the effects of irregularity by permitting random initial tow offsets. Theoretical studies using the Binary Model have shown that stress variations in primary load bearing tows *due to their own waviness* are commonly much greater than those caused by local configurations of the ideal tow architecture (Section 4). We infer that detailed analysis of local stress distributions based on finite element simulations using highly refined grids to represent *geometrically ideal* unit cells are of questionable value in predicting strength. Insofar as such calculations are right, i.e., in their predictions of average stresses that are not sensitive to details of the unit cell, they could be replaced by simpler models.

8.2 Modeling Unnotched Strength

Compression

We have shown by extensive and detailed experimental analysis that textile composites fail in monotonic compression by kink band formation when the external load is aligned with one set of tows. Kink band formation follows Argon's law: the critical stress is the ratio of the critical shear stress for large shear strains in the tow divided by the local tow misalignment angle (Eq. (41)). The keys to predicting compressive strength are therefore 1) to measure the distribution of misalignment angles and 2) to predict the axial stress in a tow for a given external load.

The local axial stress can be computed by either the Modified Laminate Model (Appendix D) or the Binary Model (Appendix E), depending on whether the part or reinforcement geometry implies important triaxial stress distributions (e.g., on whether

---

[1] Work in collaboration with UC Santa Barbara in a Pratt and Whitney program.

[2] Joint work between Rockwell and UC Santa Barbara (in their ARPA URI) on the design of advanced, high temperature engine materials.

the part is a nearly laminar skin or a complex shape). The misalignment *cannot* be predicted. It must be measured. *Its control in manufacture will always be a critical issue for textile composites.*

Tension

For aligned loads, tensile failure occurs by tow rupture. Tensile failure strains or the stresses in aligned fibers at peak load are fairly consistent over different composites of the fiber and resin within the same textile class. However, strengths are generally substantially reduced from those that might be expected from data for unidirectional tape laminates. Textile processing is apparently injurious to fiber tows; and nonuniform load distribution due to random tow waviness promotes early failure in relatively straight tows. Strength predictions should be based on calculations of tow stresses, e.g. via the Modified Laminate Model or the Binary Model, coupled with experimental tensile test data to calibrate tow strength and waviness effects.

8.3 Modeling Fatigue

Compression

Compression-compression cyclic loading results in tow failure by kink band formation. A new rule for fatigue damage accumulation has been postulated, extending Argon's law by introducing a degradation rate for the critical shear flow stress (Eq. (52)). A procedure has been established for deducing unknown fatigue parameters from load-life data (Section 5). Given this calibration, fatigue life can be predicted for general tow arrangements by computing the local axial tow stress via the Modified Laminate Model or the Binary Model, as applicable; and combining this with distributions of measured misalignment angles. From these data, the expected number of kink bands in a critical structure after N cycles can be predicted. The critical number of kink bands for failure of the part should be determined by calibrating experiments.

Tension-Compression Fatigue

Experiments of 3D interlock weaves show that most fatigue damage occurs on the compressive load cycle. Empirical laws for the moderate but significant effects of the tensile load cycle await more test data.

8.4 Modeling Notched Strength

Predictions of ultimate strength when a notch exists should be based on a cohesive zone model with the bridging relation p(u) of Section 7.8. If p(u) is known, then damage propagation, strength, fracture toughness, and specimen size and shape effects can be computed by now standard methods for solving line spring, bridged crack models by integral equation formulations (e.g. [50]) or using finite element methods. There are two viable approaches to determining the material property p(u). It can be measured directly via tensile tests, as in Section 7; or it can be deduced from crack growth and/or notch sensitivity data for some set of standard specimens. In the latter method, p(u) could conveniently be expressed in parametric form. Key parameters are p_{max}, the maximum value of p, which determines unnotched strength; $W_f = 2\int pdu$, the work of fracture for a cohesive zone in the steady state or small scale bridging limit (e.g. [42], [43], [48], [49]); and u_c, the critical opening displacement at which p vanishes. Other details of the shape of p(u) may prove to be of minor significance.

Section 7 warns of considerable variance in measurements of p(u) for different specimens cut from the same composite panel. Randomness in p(u) will be reflected in randomness in notched strength. A viable approach would be to establish distributions for parameters such as W_f, p_{max}, and u_c; and then compute distributions for notched strength.

References

1. F.J. Bradshaw, G. Dorey, and G.R. Sidey, *Impact Resistance of Carbon Fiber Reinforced Plastics*, Tech. Rep. 72240. Royal Aircraft Establishment, England (1973).

2. R.C. Novak, *Materials Variables Affecting the Impact Resistance of Graphite and Boron Composites — II*, Rep. TR-74-196, Part II. U.S. Air Force Materials Laboratory, Dayton, Ohio (1975).

3. L.E. McAllister and W.L. Lachman in *Fabrication of Composites, Handbook of Composites*, Vol. 4, P.109, Elsevier, New York (1983).

4. T.R. Guess and E.D. Reedy Jr., *J. Comp. Tech. Res.* **7**, 136 (1985).

5. E.D. Reedy Jr. and T.R. Guess, *J. Comp. Tech. Res.* **8**, 163 (1986).

6. L.A. Mignery, T.M. Tan, and C.T. Sun, in *Delamination and Debonding*, ASTM Spec. Tech. Publ. 876 (edited by W.S. Johnson) pp. 371–385. ASTM, Philadelphia, PA (1985).

7. P.J. Smith and R.D. Wilson, *Damage Tolerant Composite Wing Panels for Transport Aircraft*. Boeing Commercial Airplane Company, NASA Contractor Report 3951 (1985).

8. T.-W. Chou, R.L. McCullough and R.B. Pipes, "Composites," *Scientific American* **254** [10], 193–203 (1986).

9. F. Ko in *Textile Structural Composites, Composite Materials*, 3, ed. T.-W. Chou and F. Ko (Elsevier, New York, 1989) Chapter 5.

10. R.E. Horton and J.E. McCarty in *Engineered Materials Handbook, Vol. 1, Composites*, (edited by C.A. Dostal), Am. Soc. Metals, Metals Park, Ohio (1987).

11. J. Brandt, K. Dreschler and R. Meistring, *The Application of Three-Dimensional Fiber Preforms for Aerospace Composites*, Proc. ESA Symp. on Space Applications of Advanced Structural Materials, ESTEC, Noordwijk, Netherlands, March 1990 (ESA SP-303, June, 1990) pp. 71–77.

12. B.N. Cox, M.S. Dadkhah, W.L. Morris and J.G. Flintoff, "Failure Mechanisms of 3D Woven Composites in Tension, Compression, and Bending," *Acta Metall. Mater.*, 42 3967-84 (1994).

13. B.N. Cox, M.S. Dadkhah, R.V. Inman, W.L. Morris and J. Zupon, "Mechanisms of Compressive Failure in 3D Composites," *Acta Metall. Mater.*, **40** 3285–98 (1992).

14. A. Falcone, H. Dursch, K. Nelson, and W. Avery, "Resin Transfer Molding of Textile Composites," NASA Contractor Report CR 191505, July, 1993.

15. B.N. Cox, M.S. Dadkhah, R.V. Inman, J. Flintoff, M.R. Mitchell, and W.L. Morris, "Design and Reliability Guide for Triaxially Braided Composites" Rockwell International Science Center, Report to Rockwell Plastic Products Division, November 1993.

16. B.N. Cox, M.S. Dadkhah, M.R. Mitchell, and T.W. Kniveton, "Simple Models for Triaxially Braided Composites," *Composites*, in press.

17. S.S. Wilks, *Mathematical Statistics,* John Wiley and Sons, New York, 1962.

18. Y.M. Tarnopol'skii, V.A. Polyakor, and I.G. Zhigun, "Composite Materials Reinforced with a System of Three Straight, Mutually Orthogonal Fibers, I: Calculation of Elastic Characteristics," *Polymer Mechanics* **5**, 853–860 (1973).

19. A.F. Kregers and Y.G. Melbardis, "Determination of the Deformability of Three-Dimensional Reinforced Composites by the Stiffness Averaging Method," *Polymer Mechanics* **1**, 3-8 (1978).

20. A.F. Kregers and G.A. Teters, "Determination of the Elasto-Plastic Properties of Spatially Reinforced Composites by the Averaging Method," *Mech. Comp. Mater.* **17**, 25-31 (1981).

21. J.-M. Yang, C.-L. Ma, and T.-W. Chou, "Fiber Inclination Model of Three-Dimensional Textile Structural Composites," *J. Composite Materials* **20**, 472–84 (1986).

22. Y.A. Gowayed and C.M. Pastore, "Analytical Techniques for Textile Structural Composites: A Comparative Study of US-USSR Research," Fiber-Tex 90, Clemson,

South Carolina, August, 1990, NASA Conf. Publ. 3128, ed. J.D. Buckley (NASA, 1991).

23. B.N. Cox, W.C. Carter, and N.A. Fleck, "A Binary Model of Textile Composites. I Formulation," *Acta Metall. Mater.*, in press.

24. M.R. Piggott, *Load-Bearing Fiber Composites,* Pergamon, Oxford, 1990. Chapt. 1.

25. P.G. Ifju, Univ. Florida, private communication.

26. Z. Hashin, "Analysis of Properties of Fiber Composites with Anisotropic Constituents," *J. Appl. Mech.* **46**, 543-50 (1979).

27. R. Hill, "Theory of Mechanical Properties of Fiber-Strengthened Materials-III. Self-Consistent Model," *J. Mech. Phys. Solids* **13**, 189-98 (1965).

28. R.M. Christensen, "A Critical Evaluation for a Class of Micromechanics Models," *J. Mech. Phys. Solids* **38**, 379-404 (1990).

29. R. A. Naik and J. H. Crews, Jr., "Closed Form Analysis of Fiber-Matrix Interface Stresses Under Thermo-Mechanical Loadings," NASA TM-107575, 1992.

30. A.E.H. Love, "A Treatise on the Mathematical Theory of Elasticity," Dover, New York, 1944. Articles 12 and 49.

31. J.-W. Lee and C.E. Harris, "A Deformation-Formulated Micromechanics Model of the Effective Young's Modulus and Strength of Laminated Composites Containing Local Ply Curvature," ASTM STP 1059, ed. S.P. Garbo, ASTM, Philadelphia, 1990, pp. 521-63.

32. C.M. Pastore, North Carolina State University, Report to Rockwell Automotive Operations (1992).

33. B.N. Cox, "Fundamental Concepts in the Suppression of Delamination Buckling by Stitching," *Ninth DoD/NASA/FAA Conf. on Fibrous Composites in Structural Design, Lake Tahoe, Nevada, November 1991*, ed. J.R. Soderquist, L.M. Neri, and H.L. Bohon (FAA Tech. Ctr., Atlantic City, 1992, pp 1105-10.

34. B.N. Cox, "Delaminations and Buckling in 3D Composites," *J. Comp. Mater.*, 28, 1114-26 (1994).

35. R. Edgeson, Cambridge Consultants, Cambridge, UK, private communication, 1992.

36. D. Stover, "Near-net Preforms and Processes Take Shape," *Advanced Composites,* July/August, 1992.

37. B.N. Cox, "Micromechanics of Fatigue in Woven and Stitched Composites," *Final Report on NASA Contract NAS1-18840, NASA CR- 4626,* 1994.

38. A.S. Argon, *Fracture of Composites, Treatise of Materials Science and Technology,* Vol. 1, Academic Press. New York (1972).

39. W.S. Slaughter, N.A. Fleck, and B. Budiansky, "Compressive Failure of Fiber Composites: The Roles of Multiaxial Loading and Creep," *J. Engng. Mater. Tech.* 115, 308-13 (1993).

40. B. Budiansky and N.A. Fleck, "Compressive Failure of Fiber Composites," *J. Mech. Phys. Solids* 41 183-211 (1993).

41. M.R. Piggott and P.W.K. Lam, "Fatigue Failure Processes in Aligned Carbon-Epoxy Laminates," in ASTM-STP 1110 (ASTM, Philadelphia, 1991).

42. B. Budiansky, J.W. Hutchinson, and A.G. Evans, "Matrix Fracture in Fiber-Reinforced Ceramics," *J. Mech. Phys. Solids* 34, 167 (1986).

43. L.R.F. Rose, "Crack Reinforcement by Distributed Springs," *J. Mech. Phys. Solids* 34, 383 (1987).

44. M.F. Ashby, "Materials Selection in Mechanical Design," Chart 6. Pergamon, Oxford, 1992.

45. A.H. Cottrell, "Mechanics of Fracture," Tewksbury Symposium on Fracture, University of Melbourne (1963) pp. 1-27.

46. J.R. Rice, "The Mechanics of Earthquake Rupture," in *Physics of the Earth's Interior, Proceedings of the International School of Physics, "Enrico Fermi,"* ed. A.M. Dziewonski and E. Boschi (North Holland, Amsterdam, 1980) pp. 555-649.

47. A. Hillerborg, "Analysis of One Single Crack," in *Fracture Mechanics of Concrete,* ed. F.H. Wittmann (Elsevier Science, Amsterdam, 1983) pp. 233-49.

48. G. Bao and Z. Suo, "Remarks on Crack Bridging Concepts," *Appl. Mech. Review* 45 (1992) 355-66.

49. B.N. Cox and D.B. Marshall, "Concepts for Bridged Cracks in Fracture and Fatigue," *Acta Metall. Mater.*, 42 (1994) 341-63.

50. B.N. Cox and D.B. Marshall, "Stable and Unstable Solutions for Bridged Cracks in Various Specimens," *Acta Metall. Mater.* 39, 579-89 (1991).

51. G.A. Van Fo Fy, *Polymer Mechanics* 2, 593-602 (1966).

Appendix A. Weave Patterns

This index provides details on the patterns of yarns found in the composites of Table 1.

In every composite, the stuffers and fillers form a coarse 0/90° array. Stuffers and fillers alternate in layers through the thickness, with fillers always occupying the outermost layers. The through-thickness reinforcement, or warp weavers, traverse the thickness of the specimen in planes normal to the fillers. They bind together fillers in different layers as they turn around them (e.g. Fig. A.1). The warp weavers also serve to hold the stuffers roughly in columns standing normal to the filler direction. The number of warp weavers between columns of stuffers, n_w, is usually one or two.

In angle interlock weaves, the warp weavers follow approximately sawtooth paths. Successive segments make angles of approximately 45° to the stuffer direction. In through-the-thickness angle interlock weaves, warp weavers turn only around fillers in the outermost layers (Fig. A.1b). In layer-to-layer angle interlock weaves, most warp weavers couple fillers in successive fillers; a few, lighter warp weavers oscillate entirely within either of the outermost layers of fillers, passing alternately under and over successive fillers (Fig. A.1a).

In orthogonal interlock weaves, the warp weavers pass right through the specimen approximately at right angles to the stuffer direction (Fig. A.1c). In composite *h*-O-1, they pass around a single filler in the outer layer of fillers before reversing back through the thickness. In composites *l*-O and *h*-O-2, they pass around two fillers before reversing. Thus the warp-weavers in orthogonal interlock weaves follow approximately rectangular wave paths of height t, the specimen thickness, and half wavelength either a_1 (*h*-O-1 and *h*-O-2) or $2a_1$ (*l*-O), where a_1 is the center-to-center separation of fillers.

The grids used in Binary Model simulations can be described conveniently as a sequence of planes lying normal to the filler direction. Most of these planes are shown in Fig. A.2. Additional grid plane patters are derived from those shown as follows: pattern $S^{(6)}$ is similar to $S^{(4)}$; pattern $O^{(6)}$ is similar to $O_1^{(4)}$; and patterns $T_1^{(6)}$ ... $T_7^{(6)}$ are similar to $T_1^{(4)}$ ... $T_5^{(4)}$; but all with two extra layers of stuffers and fillers. The grid and thus the reinforcement architecture in any case is defined by the sequence in which planes are encountered upon progressing down the filler direction (along with data for spatial scales

- see Eqs. (16)-(18) and Chapter 3. The sequences are listed for all composites in Table A.1.

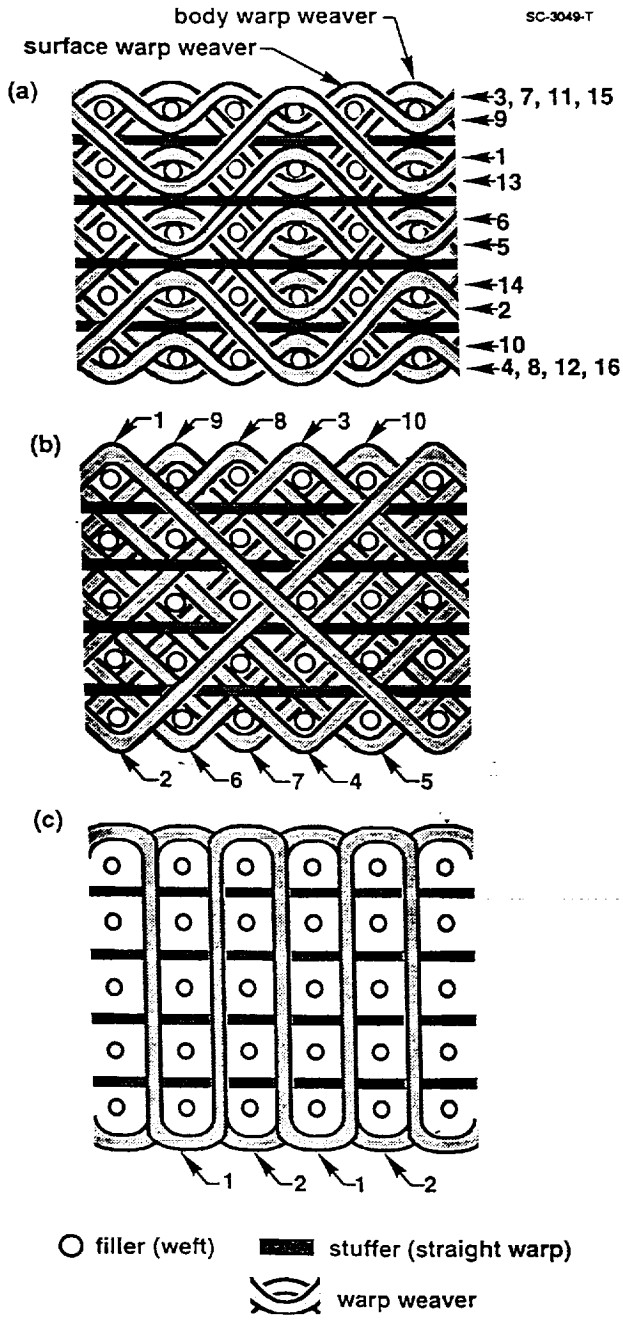

Figure A.1. Schematics of the three 3D weave architectures studied in this work. (a) Layer-to-layer angle in interlock. (b) Through-the-thickness angle interlock. (c) Orthogonal interlock. The numbers indicate the order in which warp weavers are encountered in progressing down the filler direction.

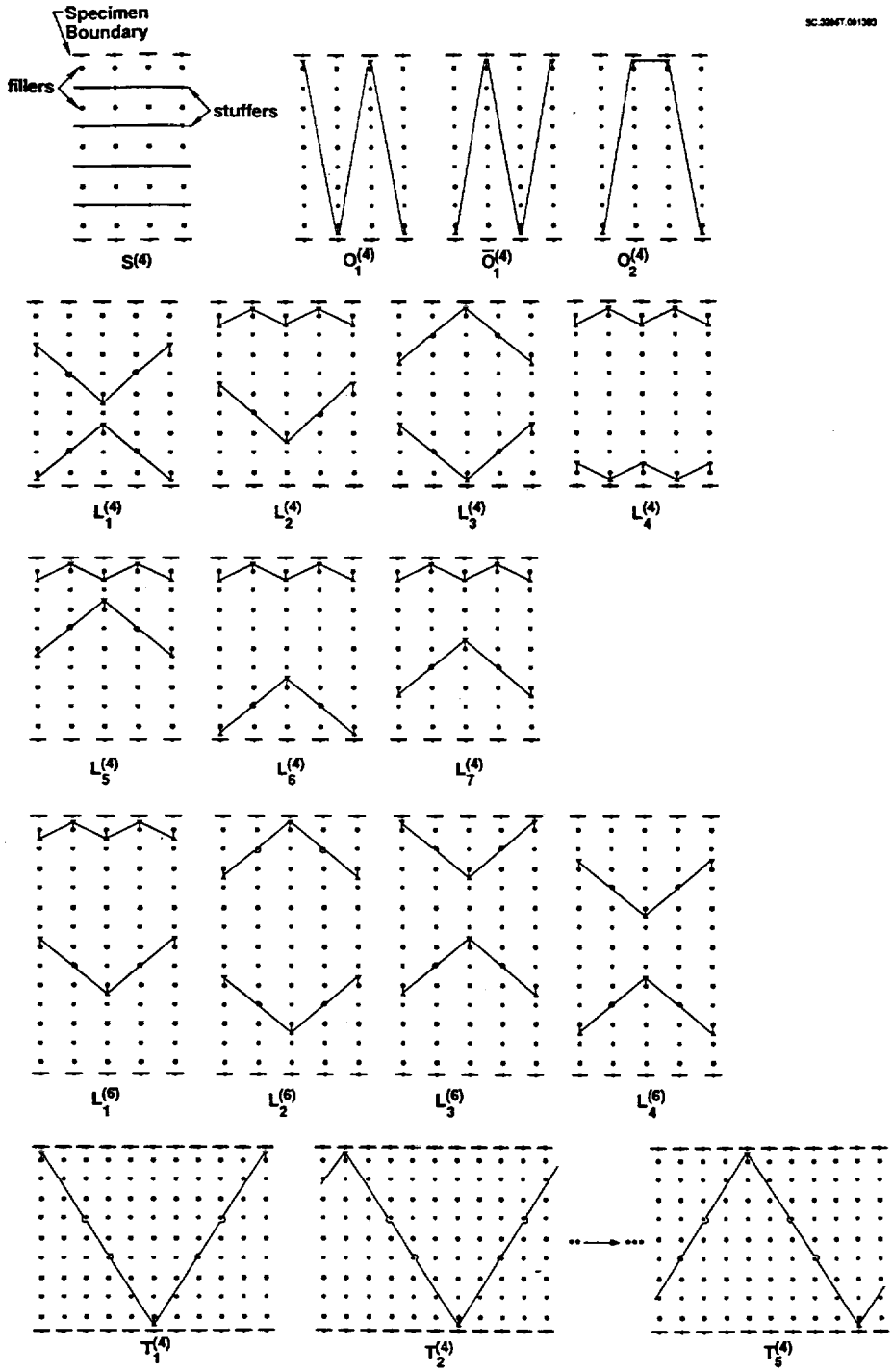

Figure A.2 Node patterns for models of composites with four or six layers of stuffers. Each diagram shows all nodes on a single plane lying normal to the filler direction (x_2 axis). An open circle indicates a node shared by filler and effective medium elements. A solid dot indicates a node shared by effective medium elements; and also by stuffer elements if it lies on an unbroken horizontal line. Solid triangular elements indicate nodes shared by warp weaver elements.

Where planes containing warp weavers appear consecutively in any sequence, they are assigned the same value of position coordinate x_2: the warp weavers are generally much lighter than stuffers and fillers and are packed into a thin volume between successive columns of stuffers.

Table A.1 Grid Plane Sequences

Composite Label	Sequence
l-L-1	$S^{(4)}, L_3^{(4)}, L_4^{(4)}, S^{(4)}, L_5^{(4)}, \overline{L}_5^{(4)}, S^{(4)}, L_6^{(4)}, \overline{L}_6^{(4)}, S^{(4)}, L_7^{(4)}, \overline{L}_7^{(4)}$
l-L-2	$S^{(4)}, L_3^{(4)}, L_4^{(4)}, S^{(4)}, L_5^{(4)}, \overline{L}_5^{(4)}, S^{(4)}, L_6^{(4)}, \overline{L}_6^{(4)}, S^{(4)}, L_7^{(4)}, \overline{L}_7^{(4)}$
l-T-1	$S^{(4)}, T_2^{(4)}, \overline{T}_2^{(4)}, S^{(4)}, T_5^{(4)}, \overline{T}_5^{(4)}, S^{(4)}, T_1^{(4)}, \overline{T}_1^{(4)}, S^{(4)}, \overline{T}_4^{(4)}3, T_4^{(4)}3, S^{(4)}3, T_3^{(4)}, \overline{T}_3^{(4)}$
l-T-2	$S^{(4)}, T_2^{(4)}, \overline{T}_2^{(4)}, S^{(4)}, T_5^{(4)}, \overline{T}_5^{(4)}, S^{(4)}, T_1^{(4)}, \overline{T}_1^{(4)}, S^{(4)}, \overline{T}_4^{(4)}, T_4^{(4)}, S^{(4)}, T_3^{(4)}, \overline{T}_3^{(4)}$
l-O	$3S^{(4)}, O_2^{(4)}, \overline{O}_2^{(4)}$
h-L-1	$S^{(4)}, L_2^{(4)}, S^{(4)}, L_3^{(4)}, S^{(4)}, \overline{L}_2^{(4)}, S^{(4)}, \overline{L}_1^{(4)}, S^{(4)}, L_1^{(4)}$
h-L-2	$S^{(6)}, L_1^{(6)}, S^{(6)}, L_2^{(6)}, S^{(6)}, \overline{L}_2^{(6)}, S^{(6)}, \overline{L}_2^{(6)}, S^{(6)}, \overline{L}_1^{(6)}, S^{(6)}, L_3^{(6)}, S^{(6)}, \overline{L}_3^{(6)}$
h-T-1	$S^{(4)}, T_1^{(4)}, \overline{T}_1^{(4)}, S^{(4)}, T_3^{(4)}, \overline{T}_3^{(4)}, S^{(4)}, T_5^{(4)}, \overline{T}_5^{(4)}, S^{(4)}, \overline{T}_2^{(4)}, T_2^{(4)}, S^{(4)}, T_4^{(4)}, \overline{T}_4^{(4)}$
h-T-2	$S^{(6)}, T_1^{(6)}, \overline{T}_1^{(6)}, S^{(6)}, T_3^{(6)}, \overline{T}_3^{(6)}, S^{(6)}, T_5^{(6)}, \overline{T}_5^{(6)}, S^{(6)}, \overline{T}_7^{(6)}, T_7^{(6)}, S^{(6)}, T_2^{(6)}, \overline{T}_2^{(6)}$ $S^{(6)}, T_4^{(6)}, \overline{T}_4^{(6)}, S^{(6)}, T_6^{(6)}, \overline{T}_6^{(6)}$
h-O-1	$2S^{(4)}, O_1^{(4)}, S^{(4)}, \overline{O}_1^{(4)}$
h-O-2	$2S^{(6)}, O_1^{(6)}, S^{(6)}, \overline{O}_1^{(6)}$

Notes: 1. A bar specifies a grid plane obtained by inverting the diagram whose label has no bar about a horizontal midline (e.g., $\overline{O}_1^{(4)}$ in Fig. A.1).

2. A number before a symbol indicates repetition (e.g., $2S^{(4)} \equiv S^{(4)}, S^{(4)}$).

Appendix B. The Elastic Properties of Unidirectional Fiber Composites

This appendix provides further details of the use of existing models in the literature for estimating the elastic properties of unidirectional fibrous composites. In the following, V is the fiber volume fraction; E_r and ν_r are Young's modulus and Poisson's ratio for the resin; E_f and ν_f are Young's modulus and Poisson's ratio for the fibers under axial load; μ_f is the axial shear modulus of the fibers: E_{ft} is the transverse Young's modulus for the fibers; and ν_{ft} is Poisson's ratio for the fibers in their plane of isotropy.

The following five models of unidirectional composites were compared.

(i) Rules of Mixtures (e.g.[24]).

(ii) Hill's Self-Consistent Method [27].

(iii) Christensen's Modified Self-Consistent Model [28].

(iv) Van Fo Fy's infinite series results for an hexagonal array [51], as simplified in [22].

(v) The average of Hashin's bounds for anisotropic fibers in an isotropic matrix [26].

Each model provides explicit expressions for the unidirectional composite elastic constants. In rules of mixtures, any composite property q_c is related to the corresponding constituent properties q_f and q_r by either

$$q_c = Vq_f + (1-V)\, q_r \qquad \text{(B.1a)}$$

or $$q_c = V/q_f + (1-V)/q_r; \qquad \text{(B.1b)}$$

with Eq (B.1a) used for the axial Young's modulus and Poisson's ratios and Eq. (B.1b) for the transverse Young's modulus and shear moduli. For models (ii)-(v), the reader is referred to the cited references for the relevant formulae, which are straightforward but lengthy to write out. A computer program for their evaluation can be obtained from the authors.

Properties estimated using the constituent properties of Table 5 for a unidirectional composite of AS4 fibers in Shell 1895 resin are compared as functions of

fiber volume fraction for each of the approximations (i)-(iii) and (v) in Fig. B.1. For models (i)-(iii), where the fibers are assumed isotropic, only the axial modulus E_f and axial Poisson's ratio ν_f were used in producing this figure. For Hashin's model, estimates were made for both isotropic and anisotropic fibers. Results for model (iv) are not plotted because they are very close to those from Christensen's method, except near V=0 and V=1, where some accuracy was lost in the simplified expressions given in [22].

Among all the cases, no discrepancy is found in the axial modulus, E_X, which was therefore not plotted. It is given very accurately by the rule of mixtures. In contrast, some significant discrepancies are found in transverse and shear moduli and Poisson's ratio in the plane of isotropy. In rules of mixtures, transverse properties and Poisson's ratios are estimated by partitioning stresses between the fibers and resin as though they were arranged in layers (e.g., [24]). The estimates given by rules of mixtures for transverse modulus and shear moduli are consequently less than those in the other models, in which the fiber geometry is treated more accurately. All of the approximations give very similar results for composites of isotropic fibers at low volume fraction, V. Hill's method gives transverse and shear properties that are much too high when $V \gtrsim 0.3$ and the fibers are much stiffer than the matrix, which is almost universally the case for polymer composites. Christensen's self-consistent model and Hashin's composite cylinder model give similar results for composites with isotropic fibers. However, as the data of Table 5 show, graphite fibers are highly anisotropic. Thus, the shear and transverse moduli shown in Fig. B.1 for Hashin's model for anisotropic fibers are much lower than those for models (ii) and (iii). Indeed, for $0.4 \leq V \leq 0.6$ all constants except the axial shear modulus are fortuitously rather close to the rule of mixtures predictions.

Engineering elastic constants were then estimated for each 3D woven composite using the constituent properties of Table 5 and all five methods of estimating domain properties. Some representative constants computed for composite *h*-L-1 are compared in Table B.1. Barring the results from Hill's model, which is clearly wrong for such high volume fractions, there are only quite small variations among the different entries for any property. The estimates following from rules of mixtures and Hashin's model with anisotropic fiber properties are especially close for every engineering constant, including those not shown in Table B.1, with the single exception of the in-plane shear modulus G_{12}, where a 30% difference is found.

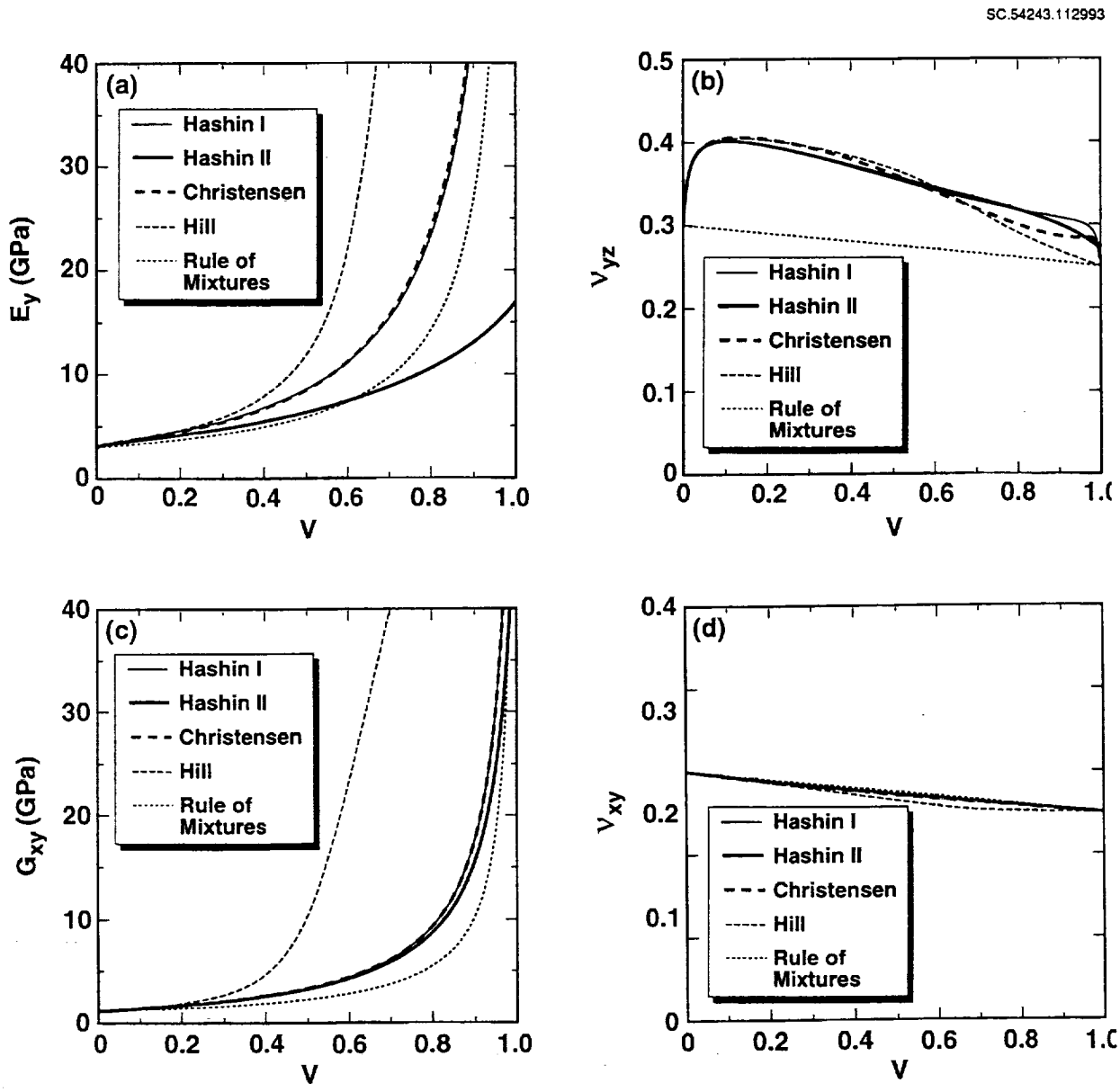

Figure B.1. Comparison of the elastic constants predicted for a unidirectional AS4/1895 composite using various models from the literature.

In the process of computing elastic constants for the composite, fiber volume fractions and elastic properties are also found for individual tow domains. These are given in Table B.2 for Hashin's model and the composite volume fractions, etc., of Tables 1,2, and 5. Table B.2 does not include the effects of tow waviness.

Table B.1
Comparison of Estimates of 3D Composite Elastic Constants for Composite *h*-L-1 Using Different Models for Domain Properties

Model for Domain Properties	E_1 (GPa)	E_2 (GPa)	G_{12} (GPa)	ν_{12}	E_3 (GPa)
Rule of Mixtures[a]	91.6	56.7	3.7	0.037	12.4
Hill [30][a]	102.1	70.3	26.6	0.11	34.5
Christensen [31][a]	93.8	60.2	5.7	0.056	17.9
Van Fo Fy [35][c]	93.3	59.5	5.7	0.053	17.3
Hashin [29] I[a]	93.7	60.1	5.7	0.056	17.9
II[b]	91.5	56.2	5.4	0.034	12.1

[a]for isotropic fibers with E_f and ν_f as in Table 4.
[b]for anisotropic fibers.
[c]with simplifications of Gowayed and Pastore [22].

Table B.2
Computed Tow Domain Properties

Composite Label	Stuffers/Fillers					Warp Weavers				
(a) Lightly Compacted	E_x (GPa)	E_y (GPa)	ν_{xy}	G_{xz} (GPa)	ν_{yz}	E_x (GPa)	E_y (GPa)	ν_{xy}	G_{xz} (GPa)	ν_{yz}
ℓ-L-1	84.2	5.11	0.280	2.32	0.378	5.11	5.11	0.280	2.32	0.378
ℓ-L-2	88.8	5.25	0.279	2.42	0.375	6.13	6.13	0.264	2.37	0.365
ℓ-T-1	111.1	6.04	0.274	3.02	0.362	6.04	6.04	0.274	3.02	0.362
ℓ-T-2	97.6	5.54	0.277	2.64	0.370	6.62	6.62	0.261	2.57	0.360
ℓ-O	115.1	6.19	0.273	3.14	0.360	6.19	6.19	0.273	3.14	0.360
(b) Heavily Compacted										
h-L-1	147.1	8.72	0.267	5.50	0.340	8.72	8.72	0.267	5.50	0.340
h-L-2	132.5	7.98	0.270	4.62	0.349	7.98	7.98	0.270	4.62	0.349
h-T-1	145.5	8.63	0.267	5.39	0.341	8.63	8.63	0.267	5.39	0.341
h-T-2	140.6	8.38	0.268	5.08	0.344	8.38	8.38	0.268	5.08	0.344
h-O-1	146.9	8.71	0.267	5.48	0.340	8.71	8.71	0.267	5.48	0.340
h-O-2	140.9	8.39	0.268	5.09	0.344	8.39	8.39	0.268	5.09	0.344

Note: The axis x lies in fiber direction, with the axes y and z forming planes of isotropy.

Appendix C. Numerical Methods for Fatigue Analysis

Procedure for Maximizing Eq. (56)

To avoid difficulty with numerical precision, Eq. (55) was written in the normalized form

$$N_f - 1 = \frac{1-\Delta\sigma/\sigma_o}{\left[\tilde{A}\Delta\sigma/\sigma_o\right]^m} \tag{C.1}$$

with

$$\sigma_o \equiv \frac{\tau_o E_s}{\zeta E_1} \tag{C.2}$$

$$\tilde{A} \equiv A^{1/m}\tau_o^{\frac{m-1}{m}} \tag{C.3}$$

Initial estimates of $\zeta_{fit}^{(i)}$ were made from the monotonic loading data:

$$\zeta_{fit}^{(i)} \approx \frac{\tau_0}{\Delta\sigma_{i0}} \tag{C.4}$$

where $\Delta\sigma_{i0}$ is the load amplitude for failure on the first cycle. Given estimates of $\{\zeta_{fit}^{(i)}\}$, A and m were updated by minimizing S of Eq. (56). Given new estimates of A and m, each $\zeta_{fit}^{(i)}$ could then be updated by minimizing

$$S_i = \sum_j \left[f^{-1}\left(\Delta\sigma_{ij}, \zeta_{fit}^{(i)}, A, m\right) - N_{ij}\right]^2 \tag{C.5}$$

i.e. the data for the i^{th} composite only. Iteration of the last two steps leads quickly to a global minimum for S.

Estimates of Uncertainty in Fitted Parameters

If the fatigue model Eq. (55) is valid, then departures of the experimental data from the fitted curves in Fig. 21 are a measure of experimental noise. The deviance σ_x in a fitted parameter x ($x \equiv \zeta_{fit}^{(i)}$ or m) is

$$\sigma_x^2 = \sum_{ij} \left(\frac{2x}{2(\Delta\sigma_{ij})} \right)^2 \sigma_{\Delta\sigma_{ij}}^2 \qquad \text{(C.6)}$$

where N_{ij} has been considered the independent variable and $\Delta\sigma_{ij}$ the dependent variable; and $\Delta\sigma_{ij}$ has been assumed normally distributed with deviance $\sigma_{\Delta\sigma_{ij}}$. From the minimum value found for S in Eq. (56), $\sigma_{\Delta\sigma_{ij}} \approx 20$ MPa for the data of Fig. 21. The partial derivatives in Eq. (C.6) were estimated by altering one datum $\Delta\sigma_{ij}$ at a time and resolving the minimization problem. As expected, $\partial(\zeta_{fit}^{(i)}) / \partial(\Delta\sigma_{ij})$ is small unless i=j. The calculated deviance in any misalignment angle $\zeta_{fit}^{(i)}$ is only ~ 0.2°; while the deviance in m is $\sigma_m \approx 4$.

Appendix D. "Weave.f": A Computer Program for Solving an Orientation Averaging Model of 3D Woven Composites

This fortran program finds the macroscopic elastic constants of a 3D woven composite similar to the subject materials of this report. It follows the model of Section 3. The program has one input file and one output file. The input contains the following variables:

v = total volume fract. of all kinds of fibers in composite
fs = fraction by vol. of all fibers that lie in stuffers
ff = " " " " " " fillers
fw = " " " " " " weavers
as = fraction by volume of composite assigned to stuffers
af = " " " fillers
aw = " " " weavers
ef = Young's modulus of fibers in stuffers or fillers
efw = " " " warp weavers
eres = " " resin
pf = Poisson's ratio of fibers in stuffers or fillers
pfw = " " " in warp weavers
pr = " " resin
bf = plane strain bulk modulus of fibers
eaf = axial Young' modulus for fibers in stuff. or fillers
etf = transverse " " " " " "
paf = axial Poisson's ratio " " " "
ptf = transverse " " " " "
gaf = axial shear modulus " " " "
gtf = transverse shear modulus " " "

other input constants ending in 'w' are for weaver fibers

weave = orth' if orthogonal interlock
'ltol' if layer-to-layer angle interlock
'thru' if through-the-thickness angle interlock
p2s,f,w = 2nd moment of normal distn of misalignment angles
for stuffers,fillers,warp weavers.
sf = scale factor for p2s,f,w to test sensitivity.

ys,f = yields of stuffers and fillers
ends, picks = number of (stuffers, fillers) per unit length
nstuf = number of layers of stuffers through thickness
nw = number of fillers between turns of weavers (orth only)
t = specimen thickness

data should appear in the following order in input file 'ortho.dat', arranged on four lines as shown:

```
weave                dummy label
v,fs,ff,as,af,p2s,p2f,p2w,eres,pr
eaf,etf,gaf,gtf,paf,ptf,eaw,etw,gaw,gtw,paw,ptw
ys,ends,yf,picks,nstuf,nw,t
```

representative input file 'ortho.dat' with data for the 11 composites of Table 1 (11 sets of data in one file):

```
ltol                lL1
.35  .385 .418 .385 .418 0.00 0.00 0.00   3   .3
235.  17.  55.  6.7  .25  .27  235.  17.  55.  6.7  .25  .27
 .652  5.1   .652  4.4  4   0  1.26
ltol                lL2
.37  .347 .501 .347 .501 4.01 9.86 0.00   3   .3
235.  17.  55.  6.7  .25  .27   85.  85.  32.7   32.7  .22 .22
 .652  5.1   .652  5.9  4   0  1.24
thru                lT1
.466 .381 .504 .381 .504 3.39 6.05 0.00   3   .3
235.  17.  55.  6.7  .25  .27  235.  17.  55.  6.7  .25  .27
 .652  4.7   .652  5.0  4   0  1.02
thru                lT2
.408 .406 .496 .406 .496 3.54 6.42 0.00   3   .3
235.  17.  55.  6.7  .25  .27   85.  85.  32.7   32.7  .22 .22
 .652  5.1   .652  5.0  4   0  0.97
orth                lO
.483 .387 .524 .387 .524 3.40 1.20 0.00   3   .3
235.  17.  55.  6.7  .25  .27  235.  17.  55.  6.7  .25  .27
```

```
 .652  4.7   .652  5.1  4   2  0.88
ltol                hL1
.62  .587 .340 .587 .340 1.74 6.38 0.00  3.7 .3
235.  17.  55.  6.7  .25  .27  235.  17.  55.  6.7  .25  .27
 .570  5.5   1.14  5.1  4   0  0.561
ltol                hL2
.557 .580 .375 .580 .375 2.04 14.8 0.00  3.7 .3
235.  17.  55.  6.7  .25  .27  235.  17.  55.  6.7  .25  .27
 1.14  7.1   2.28  7.9  6   0  0.625
thru                hT1
.613 .571 .331 .571 .331 1.33 2.94 0.00  3.7 .3
235.  17.  55.  6.7  .25  .27  235.  17.  55.  6.7  .25  .27
 .570  5.5   1.14  5.1  4   0  0.573
thru                hT2
.592 .571 .369 .571 .369 1.65 4.23 0.00  3.7 .3
235.  17.  55.  6.7  .25  .27  235.  17.  55.  6.7  .25  .27
 1.14  7.2   2.28  7.9  6   0  0.577
orth                hO1
.619 .586 .340 .586 .340 0.25 3.35 0.00  3.7 .3
235.  17.  55.  6.7  .25  .27  235.  17.  55.  6.7  .25  .27
 .570  5.5   1.14  5.1  4   1  0.579
orth                hO2
.593 .545 .353 .545 .353 0.85 1.96 0.00  3.7 .3
235.  17.  55.  6.7  .25  .27  235.  17.  55.  6.7  .25  .27
 1.14  7.1   2.28  7.9  6   1  0.587
```

resulting output file 'ortho.out' (results shown only for first case in input file):

```
 r. of m. following  Hashin
  oriav method

 sf= 1.00
 vs,vf,vw= 0.350 0.350 0.350 as,af,aw= 0.385 0.418 0.197
 p2= 0.000 e,pf=235.00  0.25 e,pr=  3.00  0.30 v=0.350
 p2= 0.000 e,pf=235.00  0.25 e,pr=  3.00  0.30 v=0.350
 p2= 0.000 e,pf=235.00  0.25 e,pr=  3.00  0.30 v=0.350
```

etas,f,w= 1.0000 1.0000 1.0000

vs,ef,pf,bf,gaf,gtf,eres,pr,rom=

0.35235.00 0.25 11.79 55.00 6.70 3.00 0.30 Hashin

v,fs,ff=0.350 0.385 0.418 as,af= 0.385 0.418 eres,pr= 3.000.300 weave=ltol

ef,pf,bf,gaf,gtf= 235.0000 0.2500 11.7899 55.0000 6.7000

" for weavers= 235.0000 0.2500 11.7899 55.0000 6.7000

e1,2,3= 36.84 38.68 9.00 g12,23,31= 2.27 2.09 5.95

p12,21,23,32,31,13= 0.023 0.025 0.216 0.050 0.148 0.607

rflex1,2= 0.79449 1.19107

Appendix E. The Binary Model of Textile Composites

The formulation of the Binary Model has been fully described in [23] and [37]. A summary may also be found in Section 4. A FORTRAN computer code BINMOD has been delivered to NASA Langley Research Center along with this report. Here operating instructions are provided.

Input

Input is entered in an input file called MOD.INP. It consists of 1) instructions for setting up the tow architecture; 2) material properties; and 3) the loading configuration. Instructions are included for the elastic case only. Simulations of progressive damage to ultimate failure in both monotonic and cyclic loading are now being performed under other funding.

The code solves for all stresses and strains in a cuboidal slab of composite containing stuffers in the x_1 direction, fillers in the x_2 direction, and body and surface warp weavers. Representative possible architectures may be found in Appendix A.

Command Summary for Binary Model Input

In the following commands, I,J, & K refer to planes on Cartesian axes on which all tow elements and effective medium faces lie. The discrete space (I,J,K) refers to points at the intersection of three planes; the origin has coordinates (1,1,1) and I,J, & K increase in the positive axis directions.

Each (I,J,K) identifies the location of a node shared by two, four, or eight effective medium element (depending on whether (I,J,K) is inside the simulated cuboid or on a boundary surface or edge. Every stuffer or filler node lies on some (I,J,K), but not all (I,J,K) are occupied by a stuffer or filler node. Warp weaver nodes lie just above or below some (I,J,K).

The coordinates (I,J,K) are used to assign a unique number to each node, which determines the global degrees of freedom associated with that node in the finite element formulation.

Since stuffer and filler nodes are a subset of effective medium nodes, the geometry of the effective medium ('EMGEN') is specified first.

'*' A COMMENT FOLLOWS AN ASTERISK ENCLOSED BY SINGLE QUOTES

All keywords are enclosed in single quotes.

KEYWORD FIELDS COMMANDS

'*' GEOMETRY:

'*' generate effective medium elements
'EMGEN' NI NJ NK XE YE ZE ZLT ZLW1 ZLW2
NI - Number of nodes in the I direction
NJ - Number of nodes in the J direction
NK - Number of nodes in the K direction
XE - Element size in the X direction (a1)
YE - Element size in the Y direction (a2/2)
ZE - Element size in the Z direction (a3)
ZLT - Element thickness on the top/bottom of specimen (a3')
ZLW1 - Body weaver offset from EM node
ZLW2 - surface weaver offset from EM node

'STFGEN' J0 K0 JM KM JD KD Generate stuffer elements
J0 - J location of first stuffer
K0 - K location of first stuffer
JM - Maximum J location of stuffers
KM - Maximum K location of stuffers
JD - Delta J increment to next stuffer in J direction
KD - Delta K increment to next stuffer in K direction

'FILGEN' I0 K0 IM KM ID KD Generate filler elements
I0 - I location of first filler
K0 - K location of first filler
IM - Maximum I location of fillers
KM - Maximum K location of fillers

ID - Delta I increment to next filler in I direction

KD - Delta K increment to next filler in K direction

'BWVGEN' I0 J0 K0 IM ID KD IAB Generate body weavers

I0 - I location of first segment of body weaver

J0 - J location of first segment of body weaver

K0 - K location of first segment of body weaver

IM - Maximum I location of fillers

KM - Maximum K location of fillers

ID - Delta I increment to next filler in I direction

KD - Delta K increment to next filler in K direction

IAB - +1 Start above node I0,J0,K0

-1 Start below node I0,J0,K0

0 Determine start from previous pattern or initial slope (KD/ID)

'SWVGEN' I0 J0 K0 IM KM ID KD IAB Generate surface weavers

I0 - I location of first segment of body weaver

J0 - J location of first segment of body weaver

K0 - K location of first segment of body weaver

IM - Maximum I location of fillers

KM - Maximum K location of fillers

ID - Delta I increment to next filler in I direction

KD - Delta K increment to next filler in K direction

IAB - +1 Start above node I0,J0,K0

-1 Start below node I0,J0,K0

0 Determine start from previous pattern or initial slope (KD/ID)

'RNDGEOS' GS ISEDG Randomize geom. of stuffers

GS - determines std. dev. of deviation in z axis direction

ISEDG - random integer seed

'RNDGEOF' GF ISEDF Randomize geom. of fillers

GF - determnes std. dev. of deviation in z axis direction

'*' MATERIAL PROPERTIES:

'EMMAT' EM VXY VXZ GXY EMYLD Set material prop's of EM

EM - Young's Modulus of EM

VXY - Poisson's ratio XY

VXZ - Poisson's ratio XZ

GXY - Shear Modulus XY

'STFMAT' ESTF Set stiffness of Stuffers

ESTF - Young's modulus of stuffers (Adjusted)

'FILMAT' EFIL Set stiffness of Fillers

EFIL - Young's modulus of fillers

'BWVMAT' EWEA1 Set stiffness of body weaver

EWEA1 - Young's modulus of body weaver (Adjusted)

'BWVSPR' ESPR1 Set stiffness of bwv spring

ESPR1 - Youngs modulus of spring (Adjusted)

'SWVMAT' EWEA2 Set stiffness of Surface Weaver

EWEA2 - Young's modulus of Surface weaver

'SWVSPR' ESPR2 Set stiffness of swv spring

ESPR2 - Young's modulus of spring (Adjusted)

'*' SET LOADING CONDITIONS

'STRAIN' STRAIN IFACE IDIR Set total eng. strain and direction

STRAIN - magnitude of total engineering strain desired (> 0)

IFACE - Axis normal to loading plane (i=1,j=2,k=3)

IDIR - Direction and axis of loading (+/- 1,2, or 3)

'STRINC' STRINC Set starting strain increment

STRINC - magnitude of strain increment (> 0)

'STRMIN' STRMIN Set minimum strain increment

STRMIN - magnitude of minimum strain increment (> 0)

'STRMAX' STRMAX Set maximum strain increment

STRMAX - magnitude of the maximum strain increment (> 0)

'FORCE' FORCE IFACE IDIR Set desired force loading

FORCE - magnitude of force on free end (> 0)

IFACE - Axis normal to loading plane (i=1,j=2,k=3)

IDIR - Direction and axis of loading (+/- 1,2, or 3)

'*' SET CONTROL FLAGS

'CHECK' Perform check run

'CRIT' CRIT Set resid/force coverg. ratio

'EMFAIL' Set EM Fail flag

'ITERATE' Set iterative sol. flag

Example - Input File for Linear Loading of Composite *l*-L-1 along Stuffer Direction to Prescribed Engineering Strain

```
'*' ARCHITECTURE "l-L-2"  DISPLACEMENT CONTROL IN X DIRECTION
'*'
'*' GEOMETRY

'*'  SET UP EFFECTIVE MEDIUM FIRST
'*'
'*'          NL   NW   NT    XE      YE      ZE      ZLT     ZLW1    ZLW2
'EMGEN'   9    9    11   1.5694  0.9081  1.3667  0.7331  1.3667  1.3667
'*'
'*' SET UP STUFFERS
'*'
'*'          J0   K0   JM   KM   JD   KD
'STFGEN'  2    3    8    9    2    2
'*'
```

```
'*' SET UP FILLERS
'*'
'*'          I0    K0    IM    KM    ID    KD
'FILGEN'     1     2     8     10    1     2
'*'
'*' SET UP BODY WEAVERS
'*'
'*'          I0    J0    K0    IM    ID    KD    IAB
'BWVGEN'     1     3     4     9     2     -2    0
'BWVGEN'     1     3     8     9     2     2     0
'BWVGEN'     1     5     6     9     2     -2    0
'BWVGEN'     1     5     6     9     2     2     0
'BWVGEN'     1     7     10    9     2     -2    0
'BWVGEN'     1     7     2     9     2     2     0
'BWVGEN'     1     9     8     9     2     -2    0
'BWVGEN'     1     9     4     9     2     2     0
'*'
'*' SET UP SURFACE WEAVERS
'*'
'*'          I0    J0    K0    IM    ID    KD    IAB
'SWVGEN'     1     3     2     9     1     -1    0
'SWVGEN'     1     3     10    9     1     1     0
'SWVGEN'     1     5     2     9     1     -1    0
'SWVGEN'     1     5     10    9     1     1     0
'SWVGEN'     1     7     2     9     1     -1    0
'SWVGEN'     1     7     10    9     1     1     0
'SWVGEN'     1     9     2     9     1     -1    0
'SWVGEN'     1     9     10    9     1     1     0
'*'
'*'
'*' SET UP MATERIAL PROPERTIES

'*'            E        VXY      VXZ      GXY      YLD     STRAIN
'EMMAT'     5052.8      0.280    0.3789   2275.9   0.02
'*'
'*'            E
```

```
'STFMAT' 174295.5
'FILMAT' 174295.9
'BWVMAT' 35893.5
'SWVMAT' 35893.5
'BWVSPR' 4883.8
'SWVSPR' 4883.8
'*'
'*' SET UP PARAMETERS FOR CONTROLLING EXECUTION
'*'
'*'          ENGSTRN      IFACE       IDIR
'STRAIN'      0.001          1           1
'STRINC'      0.001
'*'
'*' maximum absolute error in net force at any node.
'CRIT'          0.05
'ITERATE'
```

Example - Output files for above input.

File MOD.BRK contains:

A summary of macroscopic behaviour in the simulation.

```
ITER  0  STRI 0.0010000000  STRN 0.00000000
RSDL   0.0000  TFRC     0.0000  TSTRS     0.0000
ITER  1  STRI 0.0010000000  STRN 0.00100000
RSDL   0.0023  TFRC  4159.8601  TSTRS    44.8065
```

In this file:
- ITER is the iteration count (zero prior to loading)
- STRI is the applied strain increment
- STRN is the accumulated applied strain
- RSDL is the maximum computed error in all node forces
- TFRC is the total force acting on the loaded plane
- TSTRS is the average applied stress on the loaded plane

The units in MOD.BRK are always those of the data in the input file. Thus, for example, if moduli are supplied in GPA and dimensions in mm, then the force TFRC will be in GPa.mm^2.

File MOD.GEOM contains:

The coordinates (I,J,K) of all nodes of all elements, in the order effective medium elements, stuffer elements, filler elements, body warp weaver elements, surface warp weaver elements, body warp weaver springs, and surface warp weaver springs.

File MOD.STRESS contains:

1) stress components in order s11, s22, s33, s12, s23, s31 at each of the eight quadrature points in each effective medium element
2) line forces qs, qf, and qw in the stuffer, filler, and warp weaver tow elements

File MOD.STRAIN contains:

1) strain components in order e11, e22, e33, e12, e23, e31 at each of the eight quadrature points in each effective medium element
2) the macroscopic strains e11, e12, and e31

File MOD>TFORCE:

LBDCD(I) records the (L)ist of displaced (B)oun (D)ary (C)on (D)ition degrees of freedom (DOF), i=1 to #disp. For each DOF i, FC(DOF i) records the net force acting in the direction of DOF i using the internal units of stress * area. The sum of FC(DOF i) in each axis direction is the net force acting on the composite at the end of the simulation. This sum is also reported in the file MOD.STA as the total force.

Appendix F. Cumulative List of Publications

The following papers report work funded wholly or primarily under our contracts within the Advanced Composites Technology Program, NASA Langley Research Center.

1. B.N. Cox, M.S. Dadkhah, W.L. Morris and J.G. Flintoff, "Failure Mechanisms of 3D Woven Composites in Tension, Compression, and Bending," *Acta Metall. Mater.*, 42 3967-84 (1994).

2. B.N. Cox, M.S. Dadkhah, R.V. Inman, W.L. Morris and J. Zupon, "Mechanisms of Compressive Failure in 3D Composites," *Acta Metall. Mater.*, **40** 3285–98 (1992).

3. B.N. Cox and M.S. Dadkhah, "The Macroscopic Elasticity of 3D Woven Composites," *J. Mater. Sci.*, in press.

4. B.N. Cox, W.C. Carter, and N.A. Fleck, "A Binary Model of Textile Composites. I Formulation," *Acta Metall. Mater.*, in press.

5. M.S. Dadkhah, B.N. Cox, and W.L. Morris, "Compression-Compression Fatigue of 3D Woven Composites," *Acta Metall. Mater.*, in press.

6. J. Xu, B.N. Cox, M.A. McGlockton, and W.C. Carter, "A Binary Model of Textile Composites: II The Elastic Regime," *Acta Metall. Mater.*, in press.

7. B.N. Cox, M.S. Dadkhah, and W.L. Morris, "On the Tensile Failure of Some 3D Woven Composites," submitted to *Composites*.

8. B. N. Cox, M. S. Dadkhah, R. V. Inman, M. R. Mitchell, W. L. Morris, and S. Schroeder, "Micromechanics of Fatigue in Woven and Stitched Composites," in *Proc. Advanced Composites Technology Conf.*, Seattle, Washington, Oct.-Nov. 1990, ed. J. A. Davis, Jr. and H. L. Bohon (NASA Conf. Publ. 3104, 1990).

9. B. N. Cox, M. S. Dadkhah, R. V. Inman, W. L. Morris, and S. Schroeder, "Mechanisms of Compressive Failure in Woven Composites and Stitched Laminates," in *Proc. 9th DoD/NASA/FAA Conf. on Fibrous Composites in Structural Design*, Lake Tahoe, Nevada, November 1991, ed. J. R. Soderquist, L. M. Neri, and H. L. Bohon (U.S. Dept. Transportation, 1992) pp. 125-138.

10. W. C. Carter, B. N. Cox, M. S. Dadkhah, and W. L. Morris, "An Engineering Model of Woven Composites Based on Micromechanics," in *Proc. 3rd. NASA Advanced Composites Technology Conf.*, Long Beach, California, June 1992, ed. J. Davis (NASA, 1992).

11. B. N. Cox, "A View of 3D Composites," in *Processing, Properties, and Applications of Metallic and Ceramic Materials*, Proc. IRC 92, Birmingham, England, September 1992, ed. M. H. Loretto and C. J. Beevers (Engng Mater. Advisory Servives Ltd., Birmingham, 1993) pp. 1087-98.

12. B. N. Cox, W. C. Carter, M. S. Dadkhah, N. A. Fleck, J. Flintoff, W. L. Morris, and J. Xu, "A Failure Model for Textile Composites," in *Proc. Fourth NASA/DoD Advanced Composites Technology (ACT) Conference*, Salt Lake City, Utah, June 1993, ed. J. Davis and H. Bohon (NASA, 1993).

13. B. N. Cox, "Modeling Three Dimensional Composites," in *Proc. Int. Conf. on Advanced Technology in Design and Fabrication of Composite Materials and Structures*, May 1993, Torino, Italy, ed. A. Carpinteri, G. C. Sih, and G. Surace (Kluwer, Amsterdam) in press.

14. B. N. Cox," Modeling the Properties of 3D Woven Composites," in proc. Textiles Workshop, NASA Langley Research Center, December, 1994, ed. C. C. Poe, NASA, 1995.

Appendix G. Monotonic Loading Test Data

Tension	Spec. #	Peak Stress (MPa)	Strain to Failure	Modulus (GPa)	Thickness (mm)	Width (mm)
h-L-1						
	1_2	573	0.013	81	5.6	10.34
	1_4	690	0.0104	72	5.6	10.1
	1_6	655	0.03	80.7	5.6	9.3
	1_8	679	0.014	94.5	5.6	9.45
	1_26	827	0.03	66	5.6	10.3
	1_29	992	0.018			
	7_5	1000	0.02	91	5.4	9.4
p-u test						
	1_24					
	1_25	903	0.025			
	1_30	917	0.028	56		
h-L-2						
	6_10	935	0.04	83		
h-T-1						
	2_1	840	0.038	78		
	2_13	878	.043-->.1	58		
	2_15	904	.025-->.12	58		
h-T-2						
	3_7	886	0.013	72		
	3_8	807	0.011	77		
h-O-1						
	4_2	1075	0.013	89		
	4_3	1103	0.023	87		
	4_4	1027	0.015	78		
h-O-2						
	5_10	856	0.014	66		
	9_10	846	0.013	70	5.9	9.4

	Spec. #	Peak Stress (MPa)	Strain to Failure	Modulus (GPa)	Thickness (mm)	Width (mm)
Compression						
h-L-1						
	1_1	416	0.006	72		
	1_3	524	0.0074			
	1_7	469	0.005		5.6	9.6
	1_11	455	0.0055	77		
	1_20	545	0.007	80		
	1_21	634	0.009	81		
	7_6	674	0.009	87	5.4	9.4
h-L-2						
	6_11	700	0.01	80	5.7	9.5
h-T-1						
	2_2	565	0.008	80	5.7	9.8
	2_9	503	0.005	87	5.8	9.6
h-T-2						
	3_3	538	0.01	69	5.7	10.2
	3_12	517	0.0053	81.4	5.7	10.2
h-O-1						
	4_5	634	0.011	70	5.8	10.2
h-O-2						
	5_11	629	0.008	74	5.9	8.9
	9_11	603	0.0084	66	5.9	9.5
Compression: transverse loading						
h-L-1						
	1_35	221	0.01	44	5.7	10.5
h-T-1						
	2_35	318	0.01	43	5.7	10.4
h-T-2						
	3_35	372	0.008	48	5.7	10.4
h-O-1						
	4_35	317	0.016	43	5.7	10.4

			Peak Stress (MPa)	Strain to Failure	Modulus (GPa)	Thickness (mm)	Width (mm)
Compression After Impact							
	h-L-1						
		CO1-1	403	0.008	74		
buckled		CO1-3	359	0.006	76		
	h-T-1						
		CO2-1	507	0.0082	75		
	h-T-2						
		CO3-1	442	0.0083	66		
	h-O-1						
		CO4-1	472	0.01	71		

Open Hole Tension

		Ultimate Load (kip)	Ultimate Stress (MPa)	Failure Location
h-L-1				
	1_5	23.2 kip	923	grip
	1_7	26.6 kip	1060	hole
h-T-2				
	3_5	18.7 kip	749	hole

REPORT DOCUMENTATION PAGE

Form Approved
OMB No. 0704-0188

1. AGENCY USE ONLY (*Leave blank*)	2. REPORT DATE	3. REPORT TYPE AND DATES COVERED
	August 1995	Contractor Report

4. TITLE AND SUBTITLE
Failure Models for Textile Composites

5. FUNDING NUMBERS
C NAS1-19243
WU 510-02-1107

6. AUTHOR(S)
Brian Cox

7. PERFORMING ORGANIZATION NAME(S) AND ADDRESS(ES)
Rockwell International Science Center
P.O. Box 1085
Thousand Oaks, CA 91358

8. PERFORMING ORGANIZATION REPORT NUMBER

9. SPONSORING / MONITORING AGENCY NAME(S) AND ADDRESS(ES)
National Aeronautics and Space Administration
Langley Research Center
Hampton, VA 23681-0001

10. SPONSORING / MONITORING AGENCY REPORT NUMBER
NASA CR-4686

11. SUPPLEMENTARY NOTES
Langley Technical Monitor: Clarence C. Poe, Jr.
Final Report - Task 9

12a. DISTRIBUTION / AVAILABILITY STATEMENT
Unclassified - Unlimited

Subject Category 24

12b. DISTRIBUTION CODE

13. ABSTRACT (*Maximum 200 words*)

The goals of this investigation were to:

- identify mechanisms of failure and determine how the architecture of reinforcing fibers in 3D woven composites controlled stiffness, strength, strain to failure, work of fracture, notch sensitivity, and fatigue life
- and to model composite stiffness, strength, and fatigue life

A total of 11 different angle and orthogonal interlock woven composites were examined. Composite properties depended on the weave architecture, the tow size, and the spatial distributions and strength of geometrical flaws. Simple models were developed for elastic properties, strength, and fatigue life. A more complicated stochastic model, called the "Binary Model," was developed for damage tolerance and ultimate failure. These 3D woven composites possessed an extraordinary combination of strength, damage tolerance, and notch insensitivity.

14. SUBJECT TERMS
Composite; Carbon/epoxy; 3D weave; Resin transfer molding; Fiber architecture; Stiffness; Strength; Failing strain; Fatigue; Failure mechanism; Prediction models; Stochastic modeling; Shear kinking

15. NUMBER OF PAGES
142

16. PRICE CODE
A07

17. SECURITY CLASSIFICATION OF REPORT	18. SECURITY CLASSIFICATION OF THIS PAGE	19. SECURITY CLASSIFICATION OF ABSTRACT	20. LIMITATION OF ABSTRACT
Unclassified	Unclassified		